Damping Identification of an Offshore Wind Turbine

A Predictor-Based Subspace Identification Approach

D. C. van der Hoek

TUDelft
Delft
University of
Technology

Delft Center for Systems and Control

Damping Identification of an Offshore Wind Turbine
A Predictor-Based Subspace Identification Approach

MASTER OF SCIENCE THESIS

For the degree of Master of Science in Mechanical Engineering
Track Control Engineering at Delft University of Technology

D. C. van der Hoek

May 12, 2017

SIEMENS

TUDelft
Delft
University of
Technology

DCSC

DELFT UNIVERSITY OF TECHNOLOGY
DEPARTMENT OF
DELFT CENTER FOR SYSTEMS AND CONTROL (DCSC)

The undersigned hereby certify that they have read and recommend to the Faculty of Mechanical, Maritime and Materials Engineering (3mE) for acceptance a thesis entitled

DAMPING IDENTIFICATION OF AN
OFFSHORE WIND TURBINE

by

D. C. VAN DER HOEK

in partial fulfillment of the requirements for the degree of

MASTER OF SCIENCE MECHANICAL ENGINEERING
TRACK CONTROL ENGINEERING

Dated: <u>May 12, 2017</u>

Supervisor(s):

<div align="right">dr.ir. J.W. van Wingerden</div>

<div align="right">dr.ir. M. Seidel</div>

<div align="right">ir. H.C. Kramers</div>

Reader(s):

<div align="right">dr.ir. E. Lourens</div>

Abstract

Increasing the capacity of offshore wind energy is a necessary step in the transition from fossil fuels to renewable energy sources. In order to accelerate this process, the costs of wind energy should be reduced to make it more competitive with traditional energy sources. Cost reduction could be achieved by increasing the lifetime of an Offshore Wind Turbine (OWT). The lifetime is directly affected by the amount of damping present in an OWT. Hence, it is vital to have accurate estimates of the damping in order to predict the lifetime.

All Offshore Wind Turbines are equipped with a bidirectional accelerometer, resulting in large amounts of data that can be used for identification purposes. Using Operational Modal Analysis (OMA) it is possible to estimate the structural parameters of an OWT from output measurement data. Due to technical limitations, however, the available measurement data does not have a constant sampling frequency. Consequently, conventional OMA methods based on discrete-time models cannot be applied directly.

The goal of this thesis is to investigate whether the damping of an OWT can be accurately estimated using non-uniformly sampled measurement data. Two different identification approaches are taken to answer this problem. The first approach consists of resampling the measurement data with a constant sampling frequency and subsequently applying OMA methods. The second approach uses a continuous-time identification method, which can be applied directly to non-uniformly sampled measurement data.

In this thesis, the Predictor-Based Subspace IDentification (PBSID) method is used for the identification of measurement data. This method is based on a discrete-time state-space representation of a system. Using Laguerre projections the PBSID algorithm can also be extended to the continuous-time domain. The performance of both the discrete and continuous-time PBSID algorithms is examined by applying them to a simulation example. It is observed that both methods are able to provide damping estimates of similar accuracy.

Following the simulation example, both identification approaches are applied to wind turbine simulation and measurement data, respectively. Furthermore, the results from these two approaches are compared with the results obtained from uniformly sampled measurement data taken from an experimental OWT. It is concluded that accurate damping estimates of an OWT can be obtained from non-uniformly sampled measurement data.

Table of Contents

List of Figures

List of Tables

Acknowledgements

I would like to thank my supervisor Jan-Willem van Wingerden for all his help during the past year and for putting me in touch with Siemens Wind Power. It has been a real pleasure to work on my thesis for this company and learn more about the fascinating world of wind energy. Furthermore, I would like to thank my supervisors from Siemens Wind Power. Dick, thank you for volunteering to be my supervisor halfway down the line. I really appreciate that you were always willing to have a small discussion with me whenever I got stuck. Marc, you always provided some helpful comments and helped me keep the goal of this thesis in mind during our weekly meetings. Thank you for that. Rad, thanks for all the help and feedback you gave me during the first half of my graduation period. Many thanks as well to everyone else from Siemens Wind Power for providing the necessary distractions in the office.

I would also like to thank my friends and family, especially my parents, for all their support over the past year. Finally, I want to thank Claire for putting up with me during these last few months and for giving me the best support I could have hoped for.

Delft, University of Technology
May 12, 2017

Daan van der Hoek

Chapter 1

Introduction

In this chapter the background and motivation for this thesis will be discussed. A brief introduction on wind energy is first given in Section 1-1. Following this introduction, the research problem is formulated in Section 1-2. Finally, the framework of this thesis will be presented in Section 1-3.

1-1 Wind Energy

In 2015 the Dutch government signed the Paris agreement, of which the goal is to limit global warming to less than two degrees Celsius compared to pre-industrial levels [5]. In order to contribute to this goal, the Dutch government strives to generate 14% of its required energy through renewable sources by 2020 [6]. However, as can be observed in Figure 1-1, by the end of 2015 only 5.8% of the gross energy consumption in the Netherlands was produced by renewable sources. This ranks the country among the lowest contributors of renewable energy in Europe, showing the need for quick improvements over the coming years.
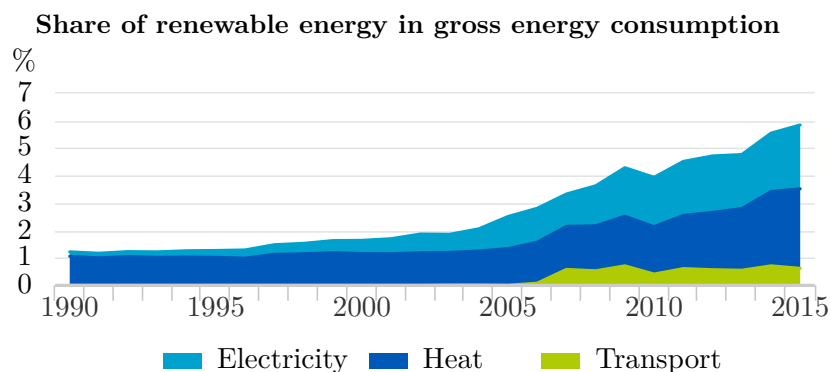
Figure 1-1: Share of renewable energy in gross energy consumption in the Netherlands until 2015 [1].

Estimates show that at the current rate of the energy transition, the 2020 target will not be achieved. In order to speed up this process a number of companies, including Siemens Wind Power (SWP), have allied in a Transition Coalition. The goal of this coalition is to motivate the Dutch government to pass a climate law for the energy goals of 2020 [7]. It is expected that such a law will help both government and industry to become more focused on reaching the climate goals.

The role of the industry in the energy transition is to reduce the overall costs of offshore wind energy. In recent years the costs of offshore wind energy have dropped significantly, resulting in the development of two offshore wind farms near the Dutch coast at the low costs of 5,45 cents per kWh [8]. However, a part of these costs is being subsidized by the Dutch government. In order to make offshore wind energy independent of government support and therefore truly competitive with fossil fuels, the costs should be reduced even further.

Currently, offshore wind turbines often have conservative designs in order to make sure they are able to withstand the harsh conditions at sea. By optimizing the design of the support structure, it might be possible to either reduce the mass or increase a turbine's lifetime, and hence reduce the overall costs. The lifetime of a turbine is influenced by the amount of fatigue damage that occurs, which in turn is directly related to the amount of damping of an Offshore Wind Turbine (OWT) [9]. When a turbine is in operation, it is well damped and the damping is dominated by aerodynamic effects. When a turbine is idling, i.e., not generating any power, it is assumed that aerodynamic damping effects cease to exist and the overall damping drops to the structural damping level [10]. It is at times like these when there is limited damping, that the most fatigue damage occurs. Thus, in order to accurately predict the lifetime, it is vital to know the damping values of a turbine.

In order to get more insight in the dynamics of an OWT, the current generation of turbines are all equipped with a bidirectional acceleration sensor. The huge amount of data that is obtained through these sensors provides a significant opportunity to compare the design basis values with the actual field values. A number of studies has been performed in recent years using this measurement data [10, 11, 12, 13, 14]. In two of these studies a Subspace Model Identification (SMI) method was used to obtain estimates of the structural parameters of an idling OWT from measurement data. These identification results suggested that there might be more damping than initially assumed. In order to find out more about this phenomenon, additional research using measurement data is required.

1-2   Problem Formulation

The measurement data that was used for the identification of the structural parameters in previous research by Kramers [14] consisted of uniformly sampled data sequences. However, due to technical limitations, the majority of turbines are not equipped with sensors that are able to deliver this consistent quality. These turbines are solely equipped with a bidirectional accelerometer located in the nacelle, which only registers measurements when a significant change is detected by the sensor. Therefore, the resulting measurements do not have a constant sampling frequency. Unfortunately, conventional identification methods are not directly compatible with this kind of data, making it difficult to identify the damping for the majority of installed turbines. This leads to the problem formulation that will be addressed in this thesis:

"Identify the structural parameters of an idling Offshore Wind Turbine using non-uniformly sampled measurement data."

There are two different approaches to solving above problem, therefore the problem formulation is split into two subproblems. The first approach would be to resample the data, and subsequently apply identification methods. However, the original uniformly sampled data can never be exactly reconstructed from the non-uniformly sampled data. As a result, the estimated structural parameters obtained using resampled data might not be as accurate. The first subproblem can therefore be formulated as follows:

"Examine the effects of resampling non-uniformly sampled measurement data on the estimated structural parameters of an Offshore Wind Turbine."

In some fields of research such as medicine or transport, but also engineering applications like aircraft identification, it is often preferred to obtain a continuous-time model of a system. Because of this, many studies have been performed in recent years to extend identification methods from a discrete-time to a continuous-time framework. The nature of these methods also allows for the use of non-uniformly sampled data and could therefore prove to be a useful method for identifying the structural parameters of an OWT. The second subproblem that will be investigated in this thesis will therefore be the following:

"Investigate continuous-time identification methods and subsequently evaluate the performance when applied to non-uniformly sampled turbine measurement data."

In the next section it will be discussed how these problems are to be solved and where they fit in the framework of this thesis.

1-3   Thesis Framework

The framework of this thesis consists of two parts. The first part investigates and discusses the methodology of the identification methods that will be applied to the OWT measurement data. The second part shows the application of the identification methods to turbine measurement data and presents the overall conclusions and recommendations for future work.

- **Part I: Identification Methodology**
  The first parts is divided into three chapters. Chapter 2 starts by presenting the OWT that will be the subject of identification in this thesis. Furthermore, some basic concepts for Offshore Wind Turbines are discussed. The chapter finishes with a brief literature overview of damping identification methods that have been applied to wind turbines. Following this literature research, two identification procedures are selected that will be investigated further. The first of these methods is the discrete-time variant of the Predictor-Based Subspace IDentification (PBSID) method and will be the topic of chapter 3. The chapter starts with the introduction of the general framework that is required for this algorithm. The algorithm itself is subsequently presented and applied to a simulation example to examine its performance. More specifically, the identification results

that have been obtained using uniformly sampled data are compared to those obtained with data that has been resampled from non-uniformly sampled data. In Chapter 4, the transition is made to a continuous-representation of the PBSID algorithm. It is shown that through a transformation of the measurement data, a continuous-time representation of the system can be estimated. The continuous-time algorithm is implemented in an existing identification toolbox and is subsequently applied to non-uniformly sampled data from the same simulation example as in Chapter 3. This allows a direct comparison between the discrete-time and continuous-time variants of the PBSID algorithm.

- **Part II: Application to Offshore Wind Turbines**
  In the second part of this thesis the identification methods from Part I will be applied to turbine data. In order to assess whether the identification algorithms are able to estimate the damping of in installed OWT, they are first applied to turbine simulation data in Chapter 5. This simulation data is generated by a software package developed at SWP, which is able to simulate the interaction of the turbine with wind, waves and soil. If the identification methods are able to acquire satisfactory estimates of the turbine's damping, they can subsequently be applied to actual measurement data of an installed OWT in Chapter 6. The damping estimates that are obtained using these methods can then be compared to each other, but also to estimates that are obtained using measurement data that was acquired using a fixed sampling frequency. All the findings of this thesis are summarized once more in Chapter 7. Furthermore, recommendations based on these conclusions will be provided for future work.

Part I

Identification Methodology

Chapter 2

Offshore Wind Turbine

The significance of accurately identifying the structural parameters, especially the damping, of an Offshore Wind Turbine (OWT) was briefly explained in Chapter 1. Using first principles modeling or numerical tools such as the Finite Element Method (FEM), it is possible to get estimates of the damping present in a system. However, this has proven to be a troublesome process for complex structures such as wind turbines, as it relies on a lot of assumptions. In order to verify the damping of existing turbine models or get more accurate estimates, the response of a physical OWT has to be studied.

The aim of this chapter is to provide an introduction on Offshore Wind Turbines and give an overview of the current state-of-the-art identification methods that are being used for wind turbine identification. The 6-MW Siemens Offshore Wind Turbine is presented in Section 2-1 along with general information on wind turbines. This section also focuses on the damping of an OWT and highlights the importance of accurately identifying the damping. Section 2-2 gives a brief overview of identification methods available in literature for damping estimation from measurement data. Furthermore, the choice for the Predictor-Based Subspace IDentification (PBSID) method will be discussed.

2-1   Presenting the Offshore Wind Turbine

This section will present the OWT that is studied in this thesis and will also provide general information on wind turbines. The Offshore Wind Turbine under consideration is located in ███

2-1-1   Design of an Offshore Wind Turbine

The Offshore Wind Turbine consists of several major components, which have been visualized in Figure 2-2. A monopile foundation is used to embed the wind turbine in the seabed. A so called transition piece is placed on top of the monopile in order to connect it to the tower. The Rotor Nacelle Assembly (RNA) is subsequently mounted on the tower. The RNA is able to rotate (yaw) in order to make sure that the rotor plane is directed towards the wind when it is operational. However, when the turbine is not operational (idling) the turbine will not follow the direction of the wind. Each blade of the turbine is able to rotate (pitch) as well. By pitching, the turbine can control the amount of power that is generated at higher wind speeds. During long periods of idling, e.g. when the wind speed is too low, the blades are pitched out of the wind entirely in order to reduce the loads acting on the wind turbine.

Offshore Wind Turbines are continually subjected to combined wind and wave loads. By using the knowledge of the wind and wave conditions at a particular site, it is possible to design a turbine that is able to withstand these loads. More specifically, an OWT is designed to cope with ultimate loads acting on the structure at a given time, as well as resisting different kinds of loads over its entire lifetime. The latter type of loads are referred to as fatigue loads and are an important factor to take into account when designing an OWT.

Fatigue damage is the result of cyclic loading of a structure, resulting in the development of microscopic fractures in the material which propagate over time. The lifetime of a structure is directly influenced by the amplitudes of these loads. In order to minimize fatigue loads, wind turbines are classically designed to avoid coincidence of resonance between the first natural frequencies and the dynamic forces acting on the turbine. Current practice is to make sure that the eigenfrequencies of the first two tower bending modes are located between the 1P and 3P frequency bands [2], as can be seen in Figure 2-1. These frequency bands are the result of excitations caused by the wind, and correspond to the rotational frequency of the rotor (1P) and the three times a blade passes the tower each rotation (3P). As Offshore Wind Turbines keep growing in size, it is observed that the first natural frequency drops as well. Dropping in frequency in itself is not a problem, were it not that the energy content of the waves is also located close to this frequency. Decreasing the natural frequency of the turbine too much will then result in wave induced structural resonances, leading to higher loads and subsequent fatigue damage.
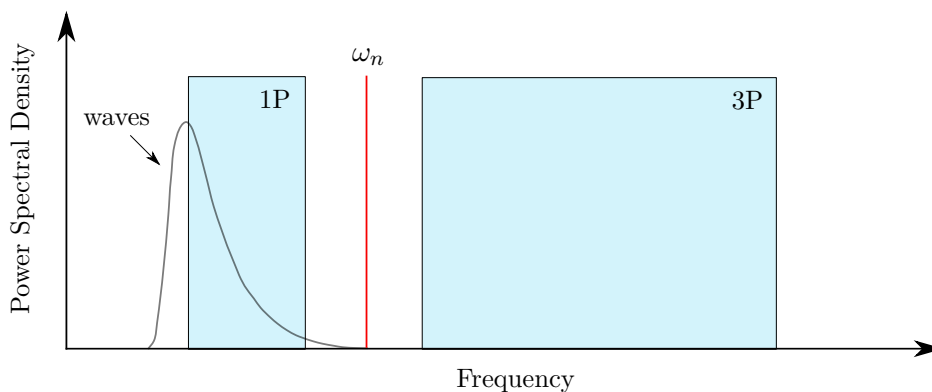
Figure 2-1: Frequency design diagram for an Offshore Wind Turbine incorporating 1P, 3P and wave spectra [2].
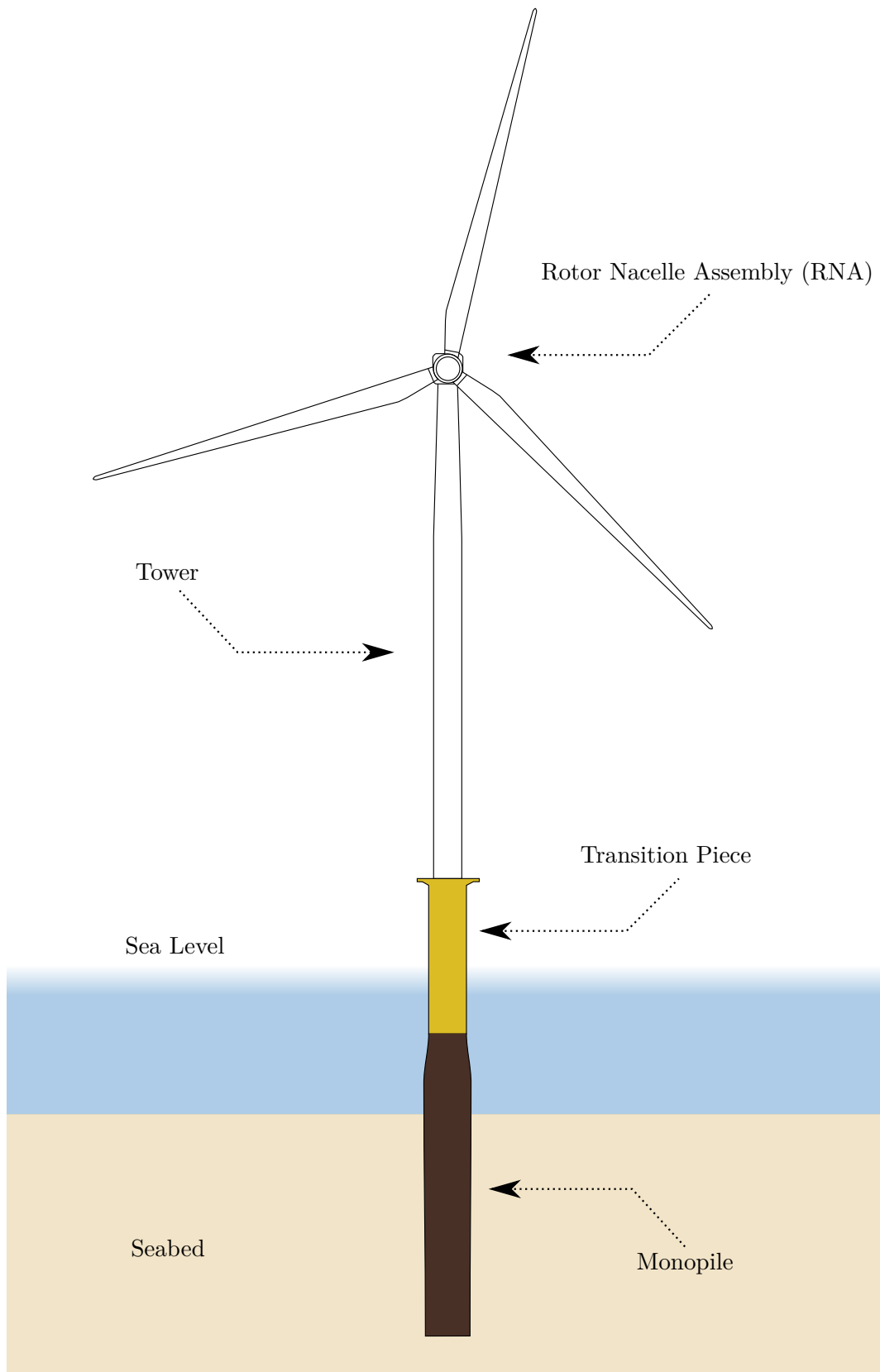
Figure 2-2: Schematic overview of an Offshore Wind Turbine on monopile foundation.

The described design practice does not solve the problem of fatigue damage altogether. Even though there is no coincidence of resonance, the turbine is still excited by the combined wind and wave loading. Through the concept of modal superposition, the total movement of the turbine can be seen as a summation of the movements of all its different modes. From all the natural modes of a turbine, the largest contribution in the movement of an OWT comes from the principal bending modes. These modes are called the first Fore-Aft (FA) and Side-Side (SS) modes and a graphical interpretation of them is provided in Figure 2-3. Consequently, it is crucial that the damping of these modes can be accurately estimated, as the amplitude of vibrations and therefore the amount of fatigue damage is inversely proportional to the damping [9].
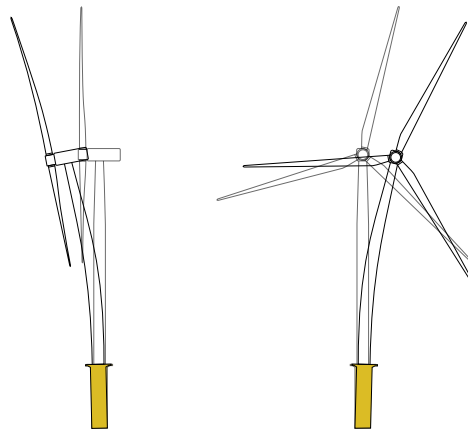
Figure 2-3: Graphical representation of the first Fore-Aft (left) and Side-Side (right) bending modes of an Offshore Wind Turbine.

2-1-2   Damping in Offshore Wind Turbines

In the field of structural dynamics, damping is defined as the dissipation of energy from the structure to the environment. In the case of an OWT, the overall damping can be seen as a summation of several damping sources. The damping of an OWT consists of the following elements [12]:

1. **Structural damping:** This type of damping is defined as the transformation of vibrational energy from the structure into heat as a result of internal friction. The structural damping ratio is typically assumed to be in the order of 0.5% critical damping for steel structures.

2. **Soil damping:** Soil damping is defined as the effect of soil on the vibration decrement of an oscillating pile. The monopile on which the wind turbine is mounted causes a cyclic motion of the surrounding soil and this results in some damping. It is often assumed that this kind of damping is of low importance compared to other kinds of damping [12]. However, other studies claim that the order of magnitude of soil damping could in fact be higher than it is often assumed [15].

3. **Hydrodynamic damping:** Hydrodynamic damping consists of two elements: wave radiation and viscous damping. Wave radiation is a damping effect resulting from the creation of waves by vibrations of the structure. Viscous damping is the result of hydrodynamic drag of the wind turbine support structure. The amount of damping coming from hydrodynamic effects is small compared to other damping sources.

4. **Aerodynamic damping:** Vibrations that are present in the wind turbine also have a direct interaction with the air that flows around it, resulting in the damping of the vibrations. This damping effect is part of a physical phenomenon called aero-elasticity. When the wind turbine is operational, the aerodynamic damping dominates the other damping sources and therefore the OWT is relatively well damped. However, the aero-dynamic damping drops if the rotor or wind speed drops, the blades are pitched out or the wind turbine is yawed away from the dominating wind direction. It is often assumed that aerodynamic damping can be neglected entirely when a turbine is idling [12]. The estimation of fatigue damage that occurs when idling is then only based on the other three damping sources, which comes down to a damping ratio of approximately $0.8 - 1.0\%$ critical damping. Consequently, the amount of fatigue damage is many times greater when a turbine is idling. ██ ██ ████████████

5. **Mass damping:** Apart from the previous damping sources, it is also possible to add additional damping to the wind turbine in the form of a mass damper. This can be done by installing an extra mass, with free movement up to a certain point, inside the tower of the turbine. Some of the vibrations can then be dissipated from the wind turbine by transferring them to the added mass. This technique has been introduced fairly recently in wind turbines and therefore has not been applied on a large scale yet. ████████ ████████████████████████████████████ have not been installed with any form of mass damping, and therefore this type of damping will not be taken into account in this thesis.

It was stated that the amount of aerodynamic damping of an idling turbine is negligible. However, recent studies have shown that the aerodynamic damping might be more complex than expected [13, 14]. More research is required in order to give more accurate estimations of the damping. For this purpose there is the possibility to use the vast database of turbine measurements from Siemens Wind Power.

2-1-3 Turbine Measurement Data

The number of installed turbines has increased greatly over the past years. In order to monitor the performance and condition of an OWT, each turbine is equipped with a number of sensors. The increased capacity of offshore wind energy has thus resulted in a large amount of measurement data. This data provides a significant opportunity to compare the design model of a turbine with the actual field values.

Each OWT is equipped with a data acquisition system which is able to provide so called fastlog data. This fastlog data is recorded on an event driven basis, meaning that it only records when the current sample crosses a certain threshold. As a result, the turbine measurement data

does not have a constant sampling rate. As was already mentioned in Chapter 1, conventional identification methods cannot be directly applied to this kind of data.

The turbine under consideration is also equipped with an additional data acquisition system. This system is used to monitor the internal forces of the turbine at several locations. For this purpose, a great number of accelerometers and strain gauges has been installed on the turbine. Furthermore, this system is able to record all these measurements with a fixed sampling frequency of $f_s = 25$ Hz. Since the turbine is equipped with two data acquisition systems, it is possible to use both types of measurement data for identification purposes and study the effect of non-uniform sampling on the damping estimates. The next section presents several identification methods that can be used for this purpose.

2-2   Identification Methods

In this section an overview is given of of possible identification methods which can be applied to offshore wind turbine measurement data. Most classical identification methods are based on working with a Linear Time-Invariant (LTI) system. When a turbine is in operation, this condition is obviously violated and these identification methods cannot be applied. In the case of an idling wind turbine, the system is assumed to be linear and time invariant.

The majority of classical identification methods fall in the category of modal analysis [16]. In modal analysis the vibrations of a structure can be modeled as a linear system. In the case of an undamped system this leads to the following equation of motion:

$$\mathbf{M\ddot{q}}(t) + \mathbf{Kq}(t) = \mathbf{f}(t), \tag{2-1}$$

where $\mathbf{q}$ is the displacement of the system, $\mathbf{f}$ is an external force acting on the system and $\mathbf{M}$ and $\mathbf{K}$ are the symmetric mass and stiffness matrices respectively. By solving this equation in the case that no external force is applied, the eigenfrequencies ω_r and the eigenmodes ϕ_r of the system can be obtained. Subsequently, it can be shown that the eigenmodes of the system are orthogonal to each other. This fact can be used to decouple the equations of motion of the system. This means that the dynamics of a multiple degrees of freedom system can be described as multiple single degree of freedom systems, which is called modal superposition [16]. In this way, each degree of freedom is represented as a function of the time-dependent amplitude of the modal component η_r and the eigenmode of that particular degree of freedom. The response of the entire system is then given by

$$\mathbf{q}(t) \simeq \sum_{r=1}^{k} \eta_r(t)\phi_r, \tag{2-2}$$

where k represents the number of dominant modes. The rest of the modes that are not considered in this solution are assumed to have very small effects on the solution.

When damping is present in a system, modal superposition becomes more complicated. This is due to the non-negative damping matrix, which does not allow a decoupling of the system [16]. In order to still be able to apply modal analysis, it is assumed that the system is lightly damped, i.e., the undamped and damped modal frequencies are approximately equal. In this way, some of the damping coefficients in the damping matrix can be neglected and modal

superposition can still be used. This will form the basis of the identification method that will be discussed in this section.

A classical identification method is that of Experimental Modal Analysis (EMA) [17]. This method consists of exciting the structure with a known input force and measuring its response at different locations using, for instance, accelerometers. However, in the case of an OWT this method is very impractical since wind and wave forces cannot be accurately measured. This leaves only Operational Modal Analysis (OMA) to be used for the identification of an OWT.

2-2-1 Operational Modal Analysis

When input forces cannot be measured but only output measurements are available, it is possible to use OMA methods. These methods only require output measurements from systems under normal conditions to identify the structural parameters. An advantage of this method is that the system is identified using realistic excitations. OMA methods also assume that the system to be identified is an LTI system. Additionally, the excitations are assumed to be given by an uncorrelated white noise sequence in the frequency band of interest and should be distributed over the entire structure [18]. As stated before, these assumptions are violated when a wind turbine is rotating and consequently regular OMA methods cannot be directly applied.

In order not to violate the OMA assumptions, measurements are commonly taken from idling wind turbines or from an overspeed stop test [10]. The latter means that the wind turbine is sped up until it reaches its maximum operating speed, after which it is shut down. At the moment of shut down, the blades are pitched out of the wind and the thrust force acting on the rotor drops. This causes an excitation of the wind turbine in the fore-aft direction which is damped out over time.

OMA methods can be divided into two different categories, time domain and frequency domain methods. Several of these methods will be discussed in the remainder of this section.

1. Time domain methods

- Commonly used time domain methods are those of the Natural Excitation Technique (NExT) type [19]. These methods use the correlation function of a structure's response to estimate the modal parameters. This method can only provide accurate estimates for the damping coefficients when there is a decay in the correlation function that consists of one mode. In the case of an overspeed stop test, the use of correlation functions is not necessary, since the exponential functions can be directly fitted to the decaying measurement response. Both methods have been successfully applied on an OWT to identify the damping [10]. However, these methods become inaccurate when several modes are grouped close to each other.

- Another type of time domain techniques consists of Prediction Error Methods (PEM) [20]. The PEM framework contains multiple algorithms that are able to estimate the parameters of a system by minimizing the prediction errors. The prediction error methods all have different model parameterizations with each their own advantages and disadvantages, which makes them applicable to a wide variety of systems. In general,

PEM are able to provide models with good asymptotic properties. However, PEM also have some drawbacks. First of all, unlike other OMA methods, PEM always require an explicit parametrization. Secondly, the numerical solution to the minimization problem often proves to be very computationally intensive and leads to a search over multiple local minima. Finally, the computation of the parameters requires accurate initial values of the parameters, which can be hard to find when dealing with complex structures.

- The last category of time domain OMA methods that will be briefly discussed in this section, is that of Stochastic Subspace Identification (SSI) methods. SSI methods are based on a LTI state-space representation of a system. The advantage of SSI methods is that they are numerically robust and are less computationally intensive than PEM. Furthermore, they can be directly applied to Multiple-Input Multiple-Output (MIMO) systems and they can be extended to a continuous-time framework in order to deal with non-uniformly sampled data. Another advantage of SSI methods is that some of them can also be employed in case of colored noise [21]. Within the class of SSI there are different algorithms to be found. So called Multivariable Output-Error State-sPace (MOESP) type algorithms [22] have been successfully applied to wind turbines in the recent past [13, 14]. The state of the art in subspace identification is represented by the PBSID$_{opt}$ algorithm [23]. The difference between the two methods is that the former directly estimates the state matrices from an extended observability matrix, while the latter first computes a state sequence before determining the system matrices.

2. Frequency domain methods

- A frequently used OMA technique is the Frequency Domain Decomposition (FDD) method [21]. The FDD method uses the spectral densities of the output signal to estimate the modal parameters. The first step in doing this, is to apply a Fast Fourier Transform (FFT) to the output data in order to transform it to the frequency domain. Using the frequency domain output data, the covariance matrix, also called the Power Spectral Density (PSD) matrix, can be computed. All the modal parameters of interest are stored within the PSD matrix. In order to identify these parameters, a Singular Value Decomposition (SVD) is used. The singular values can subsequently be plotted over the frequency spectrum. By repeating this progress for a number of discrete frequencies and averaging the results, the eigenfrequencies of the system can be determined. The eigenfrequencies are located at the peaks of the frequency response. The modes corresponding to the eigenfrequencies can be found in the singular vectors from the SVD. By using this peak picking method over multiple frequency spectra, it is possible to identify coupled modes that would otherwise have been dominated by other modes.

- The FDD method can be extended in order to estimate damping values of a structure. This results in the Enhanced Frequency Domain Decomposition (EFDD) method [24]. After the peaks in the frequency spectrum have been determined using the FDD, the single degree of freedom PSD function is transformed back to the time domain using the inverse FFT. The natural frequency is subsequently determined by counting the number of zero-crossings of the decaying correlation function of the single degree of freedom system over time. The damping can subsequently be estimated through a

simple curve fit of the correlation function. Literature shows us that the EFDD method is a fast and reliable method to determine the eigenfrequencies and modes, when the modes are well separated and when light damping is assumed.

- Other types of frequency domain techniques use modal parameter estimators. Examples of these methods are the least squares complex frequency domain estimators (polyMAX) or polyreference maximum likelihood estimators (pLME) [25]. These methods estimate the modal parameters by optimizing a cost function that consists of the frequency data and a model parametrization. These methods consist of multiple iterations, where a model is estimated in each iteration. This means that it is possible to determine the poles of the system at each iteration. These poles can be plotted as a function of the frequency to obtain the stabilization chart, which can be used to determine the physical poles of the system. Both estimators have been applied to wind turbines measurements and were shown to be able to estimate the damping of an OWT [12, 26].

The identification methods that have been presented in this section are summarized in Table 2-1, where their performance is rated for some important criteria. It can be observed that there are several methods which are capable of estimating the damping of an OWT. However, only SSI methods can be extended to a continuous-time framework in order to be applied to non-uniformly sampled data. Frequency domain techniques are generally computationally faster. However, they rely on the FFT of time domain data, which is not available for non-uniformly sampled data. This is the most important reason for using a subspace identification algorithm for the identification of an OWT in this thesis. More specifically, the discrete-time and continuous-time variants of the PBSID_{opt} algorithm will be applied to the turbine measurement data, as it is the state of the art in subspace identification.

Table 2-1: Comparison of identification methods

	Time domain			Frequency domain		
	NExT	PEM	SSI	FDD	EFDD	polyMAX/pLME
Damping estimation	✓	✓	✓	✗	✓	✓
Closely spaced modes	✗	✓	✓	✗	✗	✓
Computationally fast	∼	✗	∼	✓	✓	✓
Non-uniformly sampled data	✗	✗	✓	✗	✗	✗

2-3   Conclusion

The goal of this chapter was to highlight the importance of damping for an OWT and to select a suitable method for damping identification. The lifetime of a turbine is dependent on the amount of fatigue damage, which in turn is inversely proportional to the damping. The damping of a turbine is assumed to be at its lowest when it is idling, resulting in a large amount of fatigue damage during this state. Therefore, it is important to have accurate damping estimates for an idling OWT.

In order to find the right method for estimating the damping of an OWT, a brief overview of identification methods found in literature was presented. The so called PBSID_{opt} algorithm

was judged to be the most promising method for this purpose. This algorithm belongs to the class of SSI methods that are based on discrete-time state-space models. However, these methods can also be transformed to a continuous-time framework. This will allow the use of non-uniformly sampled measurement data, such as fastlog data, for identification purposes. The two following chapters will discuss the discrete and continuous-time PBSID algorithms, respectively, in further detail.

Chapter 3

Discrete-Time Predictor-Based Subspace Identification

In this chapter Predictor-Based Subspace IDentification (PBSID) is presented as a damping identification method for an Offshore Wind Turbine (OWT). More specifically, the PBSID$_{opt}$ algorithm as presented by Chiuso is discussed [27, 23]. This algorithm is able to provide identification results with a lower variance compared to the standard PBSID algorithm . This method combines the least-squares estimation of a Vector-Auto-Regressive with eXogenuous input (VARX) model with typical subspace identification steps. These steps include the use of Hankel-like matrix structures and numerical tools such as the Singular Value Decomposition (SVD) and RQ-factorization in order to find estimates of the state sequence and system matrices, respectively. The PBSID$_{opt}$ method is suited for closed-loop system identification, but can also be applied to an open-loop system such as an OWT.

The entire identification procedure incorporating the PBSID$_{opt}$ algorithm has been visualized in Figure 3-1, with each step of the procedure referring to a specific section in this chapter. Section 3-1 will present a representation of the system that is uses for the PBSID$_{opt}$ algorithm, rewritten for the purpose of Operational Modal Analysis (OMA). In Section 3-2, the theory behind PBSID is discussed and the algorithm is presented. The PBSID$_{opt}$ algorithm will subsequently be evaluated by applying it to a simulation example in Section 3-3. First, uniformly sampled data sets will be taken from the simulation example to be used for identification. Second, non-uniformly sampled data sets will be resampled and used for identification. Comparing both cases allows for analysis of the effects of resampling on the estimation of the modal parameters of an OWT. Conclusions on the algorithm and the simulation results are provided in Section 3-4.
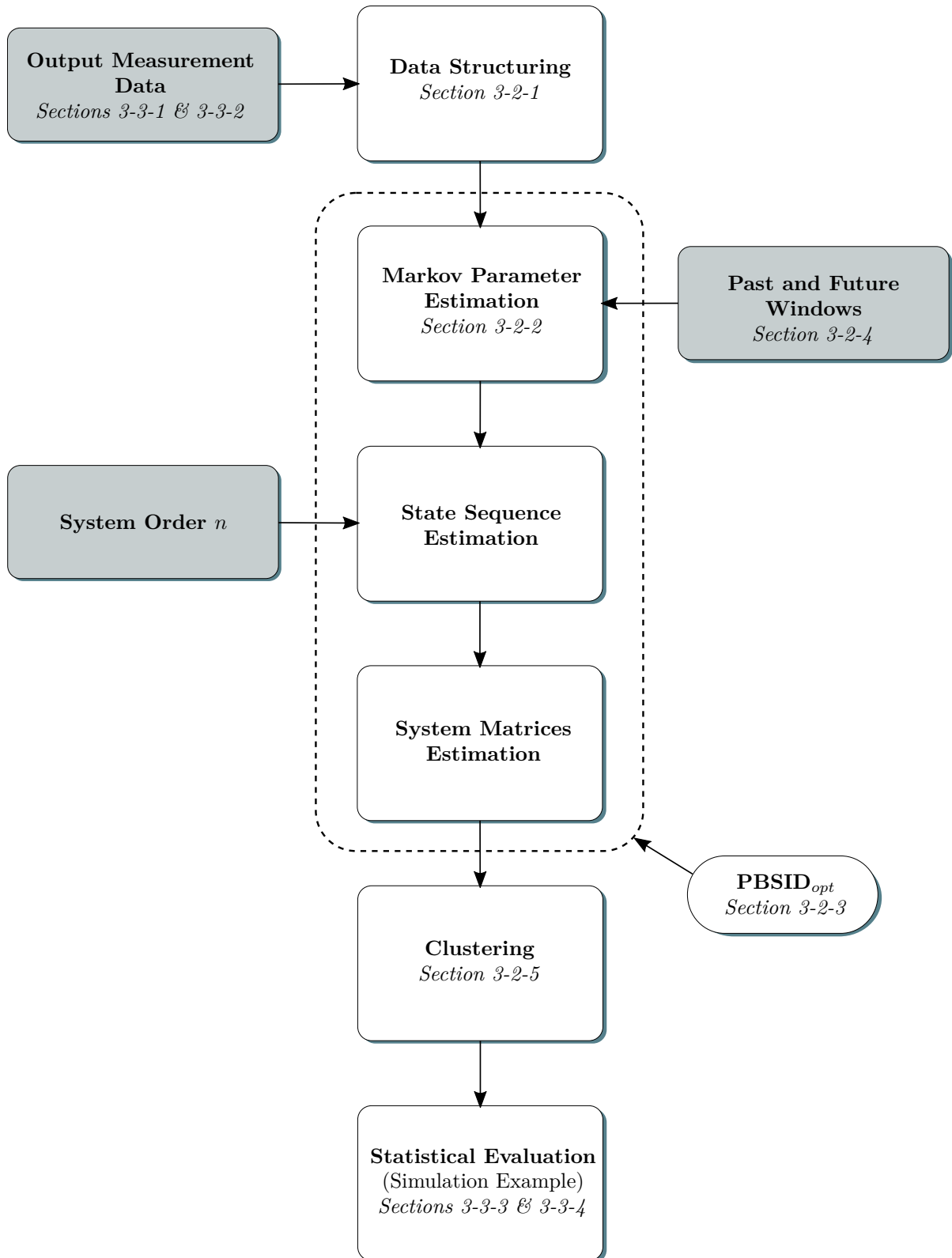
Figure 3-1: Flowchart of the discrete-time PBSID$_{opt}$ procedure.

3-1   System Representation for Operational Modal Analysis

This section provides the state-space representation for the PBSID$_{opt}$ algorithm in the case of OMA. The application of Stochastic Subspace Identification (SSI) algorithms requires assumptions regarding the system that is to be identified. It is assumed that the system is a finite dimensional, Linear Time-Invariant (LTI) system subjected to both process and measurement noise. Hence, it can be written in the discrete-time innovation state-space form as

$$x(k + 1) = Ax(k) + Bu(k) + Ke(k), \tag{3-1a}$$
$$y(k) = Cx(k) + Du(k) + e(k). \tag{3-1b}$$

This state-space representation contains the system matrix $A \in \mathbb{R}^{n \times n}$, the input matrix $B \in \mathbb{R}^{n \times m}$, the output matrix $C \in \mathbb{R}^{\ell \times n}$, the direct feed-through term $D \in \mathbb{R}^{\ell \times m}$ and the Kalman gain $K \in \mathbb{R}^{n \times \ell}$. Here the parameters n, m and ℓ denote the system order, number of inputs and number of outputs respectively. The state sequence, input signal, output signal and innovation signal are respectively represented by the vectors $x(k) \in \mathbb{R}^n$, $u(k) \in \mathbb{R}^m$, $y(k) \in \mathbb{R}^\ell$ and $e(k) \in \mathbb{R}^\ell$. It is assumed that the innovation signal $e(k)$ is an ergodic zero-mean white noise sequence with covariance matrix $\mathbb{E}\{e(j)e(k)^T\} = W\delta_{jk}$, with $W \succ 0$ and δ_{jk} representing the Kronecker delta. Furthermore, it is assumed that the system is a minimal realization of order n, by definition the pair (A, C) should therefore be observable and $(A, \begin{bmatrix} B & KW^{\frac{1}{2}} \end{bmatrix})$ reachable. The matrices A and $(A - KC)$ are assumed to be stable, meaning that their eigenvalues are located within the unit circle. This last assumption allows for the consistent estimation of the observer Markov parameters, as will be shown Section 3-2.

The state-space form given in Equation (3-1) is useful when the input vector $u(k)$ is available for identification purposes. However, as was explained in Chapter 2, the input which represents the wind and wave loads acting on the OWT is not known. As a result, we are left to use SSI methods, which are based on the state-space representation given by

$$x(k + 1) = Ax(k) + Ke(k), \tag{3-2a}$$
$$y(k) = Cx(k) + e(k). \tag{3-2b}$$

Here it is assumed that no deterministic input is acting on the system, but that it is solely excited by a stochastic input signal $e(k)$ [28]. Since the forces resulting from wind and waves can be described as (coloured) noise signals, it is possible to use the expression from Equation (3-2) to model the dynamics of an OWT.

By rewriting Equation (3-2b) to obtain an expression for the innovation signal $e(k)$ and subsequently inserting this into Equation (3-2a), the one-step-ahead predictor state-space representation is obtained as

$$x(k + 1) = \tilde{A}x(k) + Ky(k), \tag{3-3a}$$
$$y(k) = Cx(k) + e(k), \tag{3-3b}$$

where $\tilde{A} = A - KC$. This expression forms the basis for the PBSID$_{opt}$ algorithm which will be introduced in the next section.

3-2   PBSID$_{opt}$ Algorithm

Now that a suitable state-space representation for OMA has been provided, the PBSID$_{opt}$ algorithm will be presented in this section as it was formulated by Van der Veen et al. [29]. First, Section 3-2-1 introduces new notations which are required for deriving the algorithm. Next, the data equation which is related to the Auto-Regressive with eXogenuous input (ARX) model is constructed in Section 3-2-2. In Section 3-2-3, it is shown how the state-space matrices can be estimated by solving a series of least-squares problems. Section 3-2-4 gives additional information on the selection of the past and future window parameters. Finally, Section 3-2-5 presents a hierarchical clustering method that is used to automatically classify all the estimated poles.

3-2-1   Preliminaries

Before it is possible to derive the PBSID$_{opt}$ algorithm, additional notations are required. First, the stacked sample $z(k) = y(k)$ is introduced. When input measurement data is available, the stacked sample contains the input and output vectors at time instance k. However, in the case of SSI it only contains the output vector. The stacked sample can be extended with multiple time instances to obtain the stacked vector

$$z^{(p)}(k) = \begin{bmatrix} z(k-p)^T & z(k-p+1)^T & \cdots & z(k-1)^T \end{bmatrix}^T,$$

where p represents the so called past window. Second, a block Hankel matrix is constructed from a data sequence in the following way

$$Z_{i,s,N} = \begin{bmatrix} z(i) & z(i+1) & \cdots & z(i+N-1) \\ z(i+1) & z(i+2) & \cdots & z(i+N) \\ \vdots & \vdots & \ddots & \vdots \\ z(i+s-1) & z(i+s) & \cdots & z(i+N+s-2) \end{bmatrix}.$$

Third, the use of block-row matrices is required. These matrices are denoted by $Z_{i,N}$, and are essentially Hankel matrices with a block size of $s = 1$. Finally, the reversed extended controllability matrix $\tilde{\mathcal{K}}^{(p)}$ is given by

$$\tilde{\mathcal{K}}^{(p)} = \begin{bmatrix} \tilde{A}^{p-1}K & \tilde{A}^{p-2}K & \cdots & K \end{bmatrix}.$$

3-2-2   Data Equation

Using the new notation given in Section 3-2-1, a data equation for the one-step-ahead predictor state-space representation can be derived. If an initial state $x(k)$ is assumed, this state can be propagated forward in time by the past window p as

$$x(k+p) = \tilde{A}^p x(k) + \tilde{\mathcal{K}}^{(p)} z^{(p)}(k+p). \tag{3-4}$$

The output at time instant $k+p$ can consequently be formulated as

$$y(k+p) = C\tilde{A}^p x(k) + C\tilde{\mathcal{K}}^{(p)} z^{(p)}(k+p) + e(k+p). \tag{3-5}$$

Recall from Section 3-1 that the matrix $\tilde{A} = A - KC$ is assumed to be stable and therefore has all the eigenvalues located within the unit circle. In this way, by choosing a sufficiently large value for p, it is possible to neglect the term $\tilde{A}^p$, i.e. $\|\tilde{A}^p\|_2 \simeq 0$. Hence, the output equation can be simplified to

$$y(k + p) \simeq C\tilde{\mathcal{K}}^{(p)}z^{(p)}(k + p) + e(k + p). \tag{3-6}$$

The next step is to extend this output relation from time instant p up to $N - 1$ and use the shifted data sequences to obtain a data equation consisting of block-row and Hankel matrices. This data equation can be written as

$$X_{p,N_p} \simeq \tilde{\mathcal{K}}^{(p)}Z_{0,p,N_p} \tag{3-7a}$$

$$Y_{p,N_p} \simeq C\tilde{\mathcal{K}}^{(p)}Z_{0,p,N_p} + E_{p,N_p}. \tag{3-7b}$$

where $N_p = N - p$ and the matrices Y_{p,N_p}, Z_{0,p,N_p} and E_{p,N_p} are matrices containing the output signals, stacked samples and innovation signals respectively. The matrix $C\tilde{\mathcal{K}}^{(p)}$ contains the predictor Markov parameters, which are related to an ARX model. Such a system model is given by the following equation

$$A(q)y(k) = B(q)u(k) + e(k), \tag{3-8}$$

where q^{-1} represents the unit backward shift operator and

$$A(q) = I - a_1 q^{-1} - \cdots - a_p q^{-p},$$
$$B(q) = b_0 + b_1 q^{-1} + \cdots + b_p q^{-p}.$$

Assuming that p is chosen sufficiently large and the predictor form is used, it can be observed that the ARX model is fully equivalent to the predictor model. Then the parameters a_i and b_i can be given as the predictor Markov parameters

$$a_i = C\tilde{A}^{i-1}K, \quad \text{for } i = 1 \ldots p, \tag{3-9a}$$

$$b_i = C\tilde{A}^{i-1}\tilde{B}, \quad \text{for } i = 1 \ldots p, \tag{3-9b}$$

$$b_0 = D. \tag{3-9c}$$

In the case of OMA, this comes down to finding the parameters a_i for $i = 1 \ldots p$, which will be demonstrated next.

3-2-3 Parameter Estimation in a Least-Squares Sense

Starting from the data equation given by Equation (3-7), the predictor Markov parameters, state sequence and system matrices can be estimated by solving several least-squares problems. By assuming that the innovation signal $e(k)$ is a noise sequence, it is possible to estimate the predictor Markov parameters by solving

$$\min_{C\tilde{\mathcal{K}}^{(p)}} = \left\| Y_{p,N_p} - C\tilde{\mathcal{K}}^{(p)}Z_{0,p,N_p} \right\|_F^2. \tag{3-10}$$

This problem can be efficiently solved by performing an RQ-factorization of the data matrices, such that

$$\begin{bmatrix} Z_{0,p,N_p} \\ Y_{p,N_p} \end{bmatrix} = \begin{bmatrix} R_{11} & 0 \\ R_{21} & R_{22} \end{bmatrix} \begin{bmatrix} Q_1 \\ Q_2 \end{bmatrix}. \tag{3-11}$$

The estimate of the matrix $C\tilde{\mathcal{K}}^{(p)}$ can subsequently be found by solving

$$R_{21} = C\tilde{\mathcal{K}}^{(p)} R_{11}. \tag{3-12}$$

In order to ensure uniqueness of the parameter estimates it is required that the matrix Z_{0,p,N_p} is of full rank. Using the estimated Markov parameters it is possible to come up with an estimate of the state sequence. Looking back at Equation (3-4) and exploiting $\|\tilde{A}^p\| \simeq 0$, the extended state sequence can be formulated as

$$X_{p,N_p} = \tilde{\mathcal{K}}^{(p)} Z_{0,p,N_p}. \tag{3-13}$$

The next step is to construct the extended observability-times-controllability matrix $\tilde{\Gamma}^{(f)}\tilde{\mathcal{K}}^{(p)}$. With the help of the future window f the predictor model extended observability matrix is given by

$$\tilde{\Gamma}^{(f)} = \begin{bmatrix} C \\ C\tilde{A} \\ \vdots \\ C\tilde{A}^{f-1} \end{bmatrix}. \tag{3-14}$$

The extended observability-times-controllability matrix then has the structure

$$\tilde{\Gamma}^{(f)}\tilde{\mathcal{K}}^{(p)} = \begin{bmatrix} C\tilde{A}^{p-1}K & C\tilde{A}^{p-2}K & \cdots & CK \\ C\tilde{A}^p K & C\tilde{A}^{p-1}K & \cdots & C\tilde{A}K \\ \vdots & \vdots & \ddots & \vdots \\ C\tilde{A}^{p+f-2}K & C\tilde{A}^{p+f-3}K & \cdots & C\tilde{A}^{f-1}K \end{bmatrix}. \tag{3-15}$$

Using once more the assumption that $\|\tilde{A}^p\| \simeq 0$, this matrix can be simplified to

$$\Gamma^{(f)}\tilde{\mathcal{K}}^{(p)} \simeq \begin{bmatrix} C\tilde{A}^{p-1}K & C\tilde{A}^{p-2}K & \cdots & CK \\ 0 & C\tilde{A}^{p-1}K & \cdots & C\tilde{A}K \\ \vdots & \vdots & \ddots & \vdots \\ 0 & 0 & \cdots & C\tilde{A}^{f-1}K \end{bmatrix}. \tag{3-16}$$

Looking at the first block row of this matrix, it can be seen that it is possible to compute it using the estimate of $C\tilde{\mathcal{K}}^{(p)}$ which was obtained by solving the least squares problem of Equation (3-10). Furthermore, the remaining block rows can be found by shifting the estimate of $C\tilde{\mathcal{K}}^{(p)}$ to the right.

The next step is to pre-multiply Equation (3-13) with the matrix Γ, in order to find an estimate of the state sequence. Subsequently, by computing the SVD of

$$\tilde{\Gamma}^{(f)} X_{p,N_p} = \tilde{\Gamma}^{(f)}\tilde{\mathcal{K}}^{(p)} Z_{0,p,N_p} = U_n \Sigma_n V_n^T, \tag{3-17}$$

the state sequence can be extracted up to a similarity transformation by

$$\hat{X}_{p,N_p} = \Sigma_n^{\frac{1}{2}} V_n^T. \tag{3-18}$$

In this last step one should also define the order of the state sequence and therefore the order of the state-space system. One way to get an estimate of the right system order, is to look

at the singular values of Σ_n. This is often indicated by a large gap between two consecutive singular values in the singular value plot.

Now that an estimate of the state sequence is available, it is possible to compute the estimates of the remaining state space matrices. First the matrix C can be estimated by solving the least-squares problem

$$\min_C = \left\| Y_{p,N_p} - CX_{p,N_p} \right\|_F^2 . \tag{3-19}$$

Next, the residual of the previous least-squares problem is used to estimate the innovation data matrix

$$E_{p,N_p} = Y_{p,N_p} - CX_{p,N_p}. \tag{3-20}$$

Finally, the matrices A and K are estimated by solving another least squares problem

$$\min_{A,K} = \left\| X_{p+1,N_p-1} - \begin{bmatrix} A & K \end{bmatrix} \begin{bmatrix} X_{p,N_p-1} \\ E_{p,N_p-1} \end{bmatrix} \right\|_F^2 . \tag{3-21}$$

It has to be noted that the matrices A, C and K can only be estimated up to similarity transformation T, meaning that the estimated matrices are given by $T^{-1}AT$, CT and $T^{-1}K$.

The performance of the PBSID$_{opt}$ algorithm as presented in this section is heavily dependent on the amount of output measurement data that is available. Both the accuracy and variance of the identification results improve when longer datasets are used. When identifying a system from measurement data, the length of a single measurement dataset is often limited. However, by combining multiple shorter datasets for a single identification, it is possible to improve the identification results. There are two ways to combine multiple datasets for a single identification, which will both be briefly explained next.

The first method uses the properties of the RQ-factorization of Equation (3-11) to update the R-matrix with multiple datasets. The concept of RQ-factorization is also extended to Equations (3-19) and (3-21), in order to update the estimates of the A, C and K matrices.

The second method extends the matrices of all the least-squares problems seen in this section to incorporate multiple datasets. For the least-squares problem of Equation (3-10) this results in the following matrices when j different datasets are available:

$$Y_{p,N_p} = \begin{bmatrix} Y_{p,N_p,1} & Y_{p,N_p,2} & \cdots & Y_{p,N_p,j} \end{bmatrix}, \tag{3-22a}$$

$$Z_{0,p,N_p} = \begin{bmatrix} Z_{0,p,N_p,1} & Z_{0,p,N_p,2} & \cdots & Z_{0,p,N_p,j} \end{bmatrix}. \tag{3-22b}$$

The matrices X_{p,N_p} and E_{p,N_p} are extended in the same manner and subsequently improved estimates of the state-space matrices are obtained.

The identification procedures that are done in the remainder of this thesis will be performed with the help of the PBSID-toolbox [30], which has been developed at the Delft Center for Systems and Control (DCSC). Within this toolbox the discrete-time PBSID$_{opt}$ algorithm as presented in this section has been implemented for use in MATLAB. However, the toolbox did not support the use of multiple data batches for a single identification as explained above. Both these methods were therefore added to the existing toolbox, and it was found that they provide similar results, though the former method is computationally less intensive since it uses smaller data matrices.

The PBSID$_{opt}$ algorithm presented in this section can subsequently be applied to any uniformly sampled output measurement dataset. Apart from the length of the measurement data, the performance of the identification is also dependent on the choice of the past and future window sizes. The selection of these parameters will be highlighted in the next section.

3-2-4   Past and Future Windows

This section contains additional information on the choice of the parameters p and f. The most important reason for the size of the past window p, is to make sure that the term $\tilde{A}^p$ is small enough to be removed from the data equation. However, the term $\tilde{A}^p$ can only be computed afterwards, meaning that the identification might require multiple iterations. Furthermore, by increasing the size of p, one also increases the number of parameters that are estimated in the least-squares problem of Equation (3-10). The amount of parameters that are estimated in this step is given by $p\ell^2$ in the case of SSI, indicating that it grows linearly with p. Therefore, increasing the size of p too much can result in over-fitting and an unnecessary increase in computation time.

In order to find a suitable p, order selection tools like the Akaike Information Criterion (AIC) are frequently used [31]. The standard form of the AIC is given by

$$\text{AIC} = \text{-2}\,\log(\mathcal{L}(\hat{\theta}|y)) + 2K, \tag{3-23}$$

where $\mathcal{L}(\hat{\theta}|y)$ is the maximum log-likelihood of an estimated parameter θ, given the data y. The maximum likelihood indicates the probability that a parameter θ results in a data sequence y. The term K represents the number of estimated parameters in the model. It can be observed that the criterion is aiming for the right balance between the accuracy of the prediction error and the complexity of the model. By minimizing this criterion it is possible to obtain a range of suitable values for the function parameters.

The AIC as given in Equation (3-23) cannot be directly applied to the PBSID$_{opt}$ algorithm. An alternate expression of the AIC exists for the least-squares case [32]. It is suggested to apply this expression of the AIC to the residual obtained in the VARX step of Equation (3-10) [29]. The AIC for the PBSID$_{opt}$ algorithm is given by

$$\text{AIC} = N_p \cdot \log\left(\frac{\sum_{k=p}^{N_p}(Y_{p,N_p} - C\tilde{\mathcal{K}}^{(p)}Z_{0,p,N_p})^2}{N_p}\right) + 2K \tag{3-24}$$

In this case, K represents the size of the matrix $C\tilde{\mathcal{K}}^{(p)}$. It should be noted however, that the optimal past window found using the AIC does not necessarily result in the most accurate identification of the system, and should therefore serve more as an initial indication. The optimal value of p can subsequently be found with additional tuning of the results.

The size of the future window f is only constrained by the relation $f \geq n$. For simplicity reasons, a common choice for f is given by $p = f$. However, it is important to note that the size of f also affects the variance of the estimated system matrices [33].

3-2-5   Clustering of Identification Results

In order to analyse the accuracy and precision of the identification procedure, it is necessary to apply the PBSID$_{opt}$ algorithm to multiple data sequences. Doing this results in a large

amount of estimated poles that are unsorted. If a statistical evaluation of the results has to be performed, it is required to group all the poles belonging to a particular mode. It would be very time consuming if this were to be done by hand, therefore a hierarchical clustering algorithm is presented to sort all the poles automatically [34].

Hierarchical clustering methods can be visualized by a hierarchical tree-like structure. Initially, all the poles belong to a main branch, i.e. a single cluster. Subsequently, by analysing the similarity between all the poles, the main branch can be split into multiple branches where each branch represents a cluster. These new branches can be split even further depending on the amount of clusters that is desired. A common procedure to evaluate the similarity between estimated poles is to compute the Euclidean distance. However, this might not be enough to discern between closely grouped poles. A possible solution for this is to also evaluate the mode shape belonging to each pole. For the PBSID$_{opt}$ procedure, the following distance measure is used

$$d_{i,j} = \alpha \frac{|f_i - f_j|}{f_j} + \beta \left(1 - \text{MAC}_{i,j}\right). \tag{3-25}$$

Here, the first term represents the distance between different frequency components and the second term uses the Modal Assurance Criterion (MAC) to compare the mode shapes of different estimates [35]. The MAC value is in turn given by

$$\text{MAC}_{i,j} = \frac{|\psi_i^H \psi_j|^2}{\psi_i^H \psi_j \psi_j^H \psi_i}, \tag{3-26}$$

where ψ is an eigenvector of the estimated system and ψ^H refers to the transposed conjugate (Hermitian). It has to be noted however, that the MAC value becomes less accurate if the number of sensors used for the identification is limited. Since only two acceleration measurement channels will be used for the identification of the OWT, the MAC value should be treated with care.

The idea behind this distance measure is that if the distance between two poles is small, their natural frequency and mode shape are similar. This indicates that they are likely representing the same physical mode and should belong to the same cluster. If required, it is also possible to tune the weights α and β to give more importance to either frequency or mode shape.

The entire identification procedure for the PBSID$_{opt}$ algorithm has now been presented. In the following section the working principles of the algorithm will be demonstrated by applying it to a simulation example.

3-3   Simulation Example for the PBSID$_{opt}$ Algorithm

Looking at Figure 3-1, all that remains is to supply the PBSID$_{opt}$ algorithm with output measurement data and subsequently perform a statistical evaluation. In order to demonstrate the PBSID$_{opt}$ algorithm in the output only case, it is applied to simulation data from a Multi-Degree-of-Freedom (MDoF) system. The system that is used for the identification is presented in Section 3-3-1 and in Section 3-3-2 the simulation conditions are discussed. The identification results with the original simulation data are presented in Section 3-3-3. Finally, samples from the simulation data are removed after which the data is resampled. Section 3-3-4 presents the identification results obtained using this resampled data.

3-3-1   9-DoF Simulation Model

The MDoF system that is used for the identification is given in Figure 3-2. This system consists of two subsystems which are coupled through two rigid bars, resulting in a 9-DoF system. The equation of motion belonging to this system is given by

$$M\ddot{q}(t) + D\dot{q}(t) + Kq(t) = f(t), \tag{3-27}$$

where the parameters M, D and K represent the mass, damping and stiffness matrices respectively and f is the external force acting on the masses. The vectors $q(t)$ and its first and second derivatives give the positions, velocities and accelerations of the masses respectively.
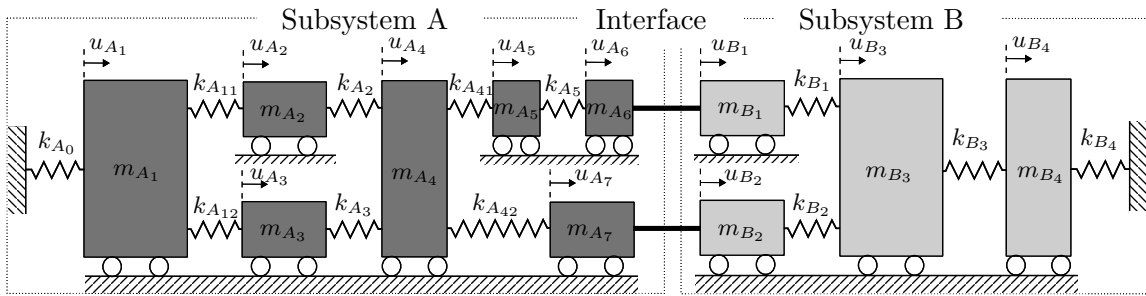
Figure 3-2: 9-DoF system used for testing the PBSID$_{opt}$ algorithm [3].

Since an OWT is considered a lightly damped structure, the 9-DoF system will also be modeled with low damping characteristics. This can be done by describing the damping using a Rayleigh damping matrix D, which is defined as

$$D = \alpha M + \beta K. \tag{3-28}$$

In this way, a damping matrix is obtained from a linear combination of the mass and stiffness matrices. The eigenfrequencies (f) and damping ratios (ζ) of the 9-DoF system that was used for the identification procedure are given in Table 3-1.

Table 3-1: Modal parameters of the lightly damped 9-DoF simulation model.

Mode	1	2	3	4	5	6	7	8	9
f [Hz]	0.665	1.478	2.471	2.628	3.143	3.996	4.600	4.935	6.311
ζ [%]	0.269	0.491	0.792	0.841	1.000	1.265	1.454	1.558	1.989

The equation of motion given by Equation (3-27) can be rewritten into a state-space representation to allow for easy simulation of the system. For this purpose the state vector of the system is first introduced as

$$x(t) = \begin{bmatrix} \dot{q}(t) \\ q(t) \end{bmatrix}.$$

Furthermore, a matrix $F = I_{[9\times9]}$ is designed that determines which of the masses of the system are excited by an external force. The following state-space representation is subsequently

obtained by deriving the derivative of the state vector $x(t)$

$$\dot{x}(t) = \underbrace{\begin{bmatrix} -M^{-1}D & -M^{-1}K \\ I & 0 \end{bmatrix}}_{A} x(t) + \underbrace{\begin{bmatrix} M^{-1}F \\ 0 \end{bmatrix}}_{B} u(t), \tag{3-29a}$$

$$y(t) = \underbrace{\begin{bmatrix} -M^{-1}D & -M^{-1}K \end{bmatrix}}_{C} x(t) + \underbrace{\begin{bmatrix} M^{-1}F \end{bmatrix}}_{D} u(t). \tag{3-29b}$$

It should be noted that the C and D matrices in Equation (3-29b) are chosen in such a way that the accelerations of the masses are obtained as output. This is done to resemble the identification of the OWT later on, which uses acceleration data as input for the PBSID$_{opt}$ algorithm. For this reason, only two output channels from the simulation results are used for the identification of the 9-DoF system. As a consequence, the identification results presented in this section are likely to be less accurate than when all output channels would have been used. Furthermore, this increases the difficulty of detecting all the modes of the system.

3-3-2 Simulation of the 9-DoF Model

First, the 9-Degree of Freedom (DoF) system is discretized using the Zero-Order Hold (ZOH) method so that it can be simulated by applying white Gaussian noise as input on every Degree-of-Freedom. The input can be applied on every DoF by choosing the matrix $F = I_{[9 \times 9]}$. The sampling frequency is initially chosen at $f_s = 100$ Hz, and the simulation ran for 100 seconds. This results in $N = 10^4$ data points for each output channel. The output data is then collected and white Gaussian noise is added in order to simulate measurement noise. The noise is chosen in such a way that a signal-to-noise ratio of $\sigma_e^2/\sigma_y^2 = 0.1$ is obtained. A small sequence of input and output data taken from the first channels is shown in Figure 3-3.
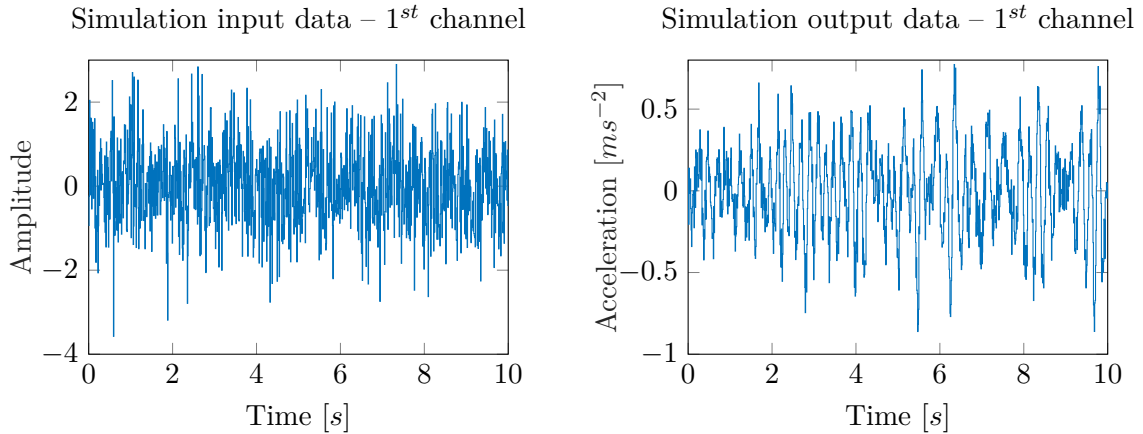
Figure 3-3: Input signal consisting of white Gaussian noise sampled at $f_s = 100$ Hz (left) and acceleration data contaminated with white Gaussian noise sampled at $f_s = 100$ Hz and signal-to-noise ratio $\sigma_e^2/\sigma_y^2 = 0.1$ (right).

The next step is to pick two channels of the output data to use for the identification. These two channels are selected by looking at the frequency content of each output channel. It was found

that the two optimal channels were located at the first and ninth degrees-of-freedom. The combined power spectrum in the frequency domain of these two channels is given in Figure 3-4. It can be seen that from these two channels every mode of the system can be observed to a certain degree, as is indicated by the peaks at the locations of the eigenfrequencies.
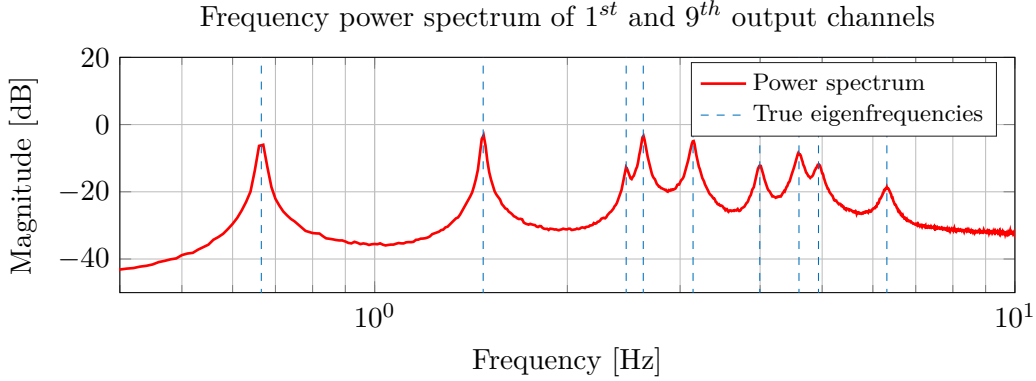
Figure 3-4: Frequency power spectrum of the first and ninth output channels of the 9-DoF system, $f_s = 100$ Hz, $N = 10^4$, $\sigma_e^2/\sigma_y^2 = 0.1$

Now that two output data channels have been selected, the simulation data can be generated for the identification. The PBSID$_{opt}$ algorithm will subsequently be analysed by performing a Monte-Carlo simulation. In a Monte-Carlo simulation the 9-DoF system will be simulated multiple times with a different input sequence each time. As a result, each output measurement dataset is different and consequently leads to different results. Using the Monte-Carlo simulation it is then possible to perform a statistical evaluation of the identification procedure. The following two sections present the results from the PBSID$_{opt}$ algorithm for multiple operating conditions.

3-3-3 Identification with Original Simulation Data

In this section the results of the PBSID$_{opt}$ algorithm applied to the original simulation data are presented. The results are obtained by applying the identification procedure given in Figure 3-1. First, a Monte-Carlo simulation consisting of 400 runs is performed to generate the simulation data. Next, the PBSID$_{opt}$ algorithm is applied to each of these data sequences using the PBSID-toolbox [30]. All of the estimated poles are then grouped using the clustering algorithm. Finally, the average and standard deviation of each cluster can be computed.

When the PBSID$_{opt}$ algorithm is applied it is required to pick a past and future window. The AIC from Equation (3-24) is used by simulating the system ten times for a range of past windows, and computing the average AIC. The results of this procedure are shown in Figure 3-5, where the AIC is given as a function of p. It is observed that the balance between the residual from the VARX step and the amount of estimated parameters is optimal for a past window around $p = 100$. However, it was found that the results using this past window size were not optimal. For this reason $p = 300$ was taken, which gave improved results while still maintaining an allowable computation time.
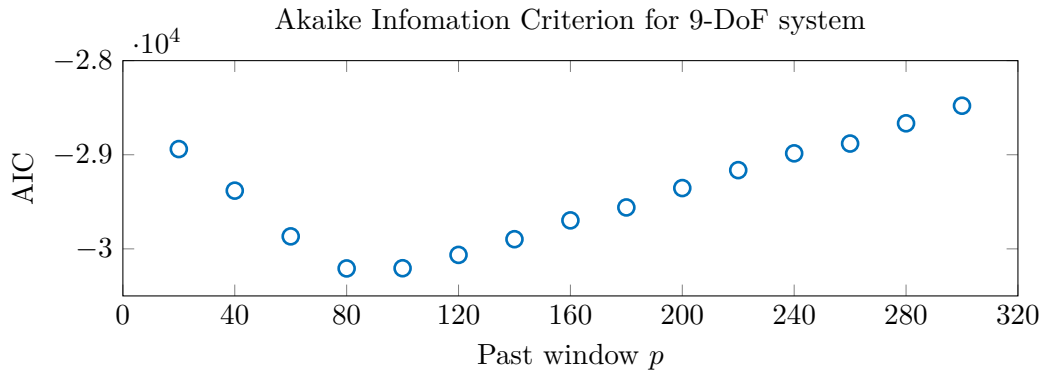
Figure 3-5: Akaike Information Criterion as a function of the past window size p for the 9-DoF system, $f_s = 100$ Hz, $N = 10^4$

For this simulation example the future window f is selected to be the same as p. As a result, the variance of the estimated modal parameters might not be optimal. However, for the sake of demonstrating the identification algorithm, tuning of the future window is not required.

The frequency and damping values obtained from the Monte-Carlo simulations are presented in Figure 3-6a. A statistical evaluation of the results is performed by computing the mean (μ), standard deviation (σ) and relative error to the analytical solution (ϵ) of each cluster. The results of this evaluation are presented in Table 3-2. Looking at the relative errors ϵ, it can be observed that the eigenfrequency of each mode could be accurately estimated for every identification procedure. The results for damping are less accurate, as can be observed by the values of ϵ and the variance of the damping ratios for some modes.

Figure 3-6c presents the singular value plots of the original system and the average of all the estimated systems. The singular value plot can be seen as a bode magnitude plot for Multiple-Input Multiple-Output (MIMO) systems, combining all the input-output relations into a single figure. By comparing the singular value plots, the overall behavior of the true and estimated systems is seen to be similar. A boxplot of the identified damping values is presented in Figure 3-6e. The horizontal line in each box represents the median of the identified damping. The box itself indicates the location of 50% of the data and the outliers are given by the red circles.

In order to improve the identification results it is possible to provide the PBSID$_{opt}$ algorithm with longer datasets. This is demonstrated by simulating the 9-DoF system for 500 seconds, which results in $N = 5 \cdot 10^4$ data points for each output channel. Another Monte-Carlo simulation was performed for this data length, of which the results are presented in Figure 3-6b. From this figure and Table 3-2 it is observed that the increase of data significantly improves the results of the estimation in terms of accuracy as well as precision.

The 9-DoF system has previously been simulated using a sampling frequency of $f_s = 100$ Hz. This sampling frequency was chosen because the smallest sampling period in the turbine fastlog data is $T_s = 0.01s$. However, this sampling frequency is not necessarily the best for the 9-DoF model. A rule of thumb is to select the sampling frequency to be ten times the bandwidth of the system [22]. In order to examine the effect of sampling frequency on the results, the system is also sampled at $f_s = 50$ Hz. It is observed in Figure 3-7 that taking a lower sampling frequency improves the identification results for the 9-DoF system.
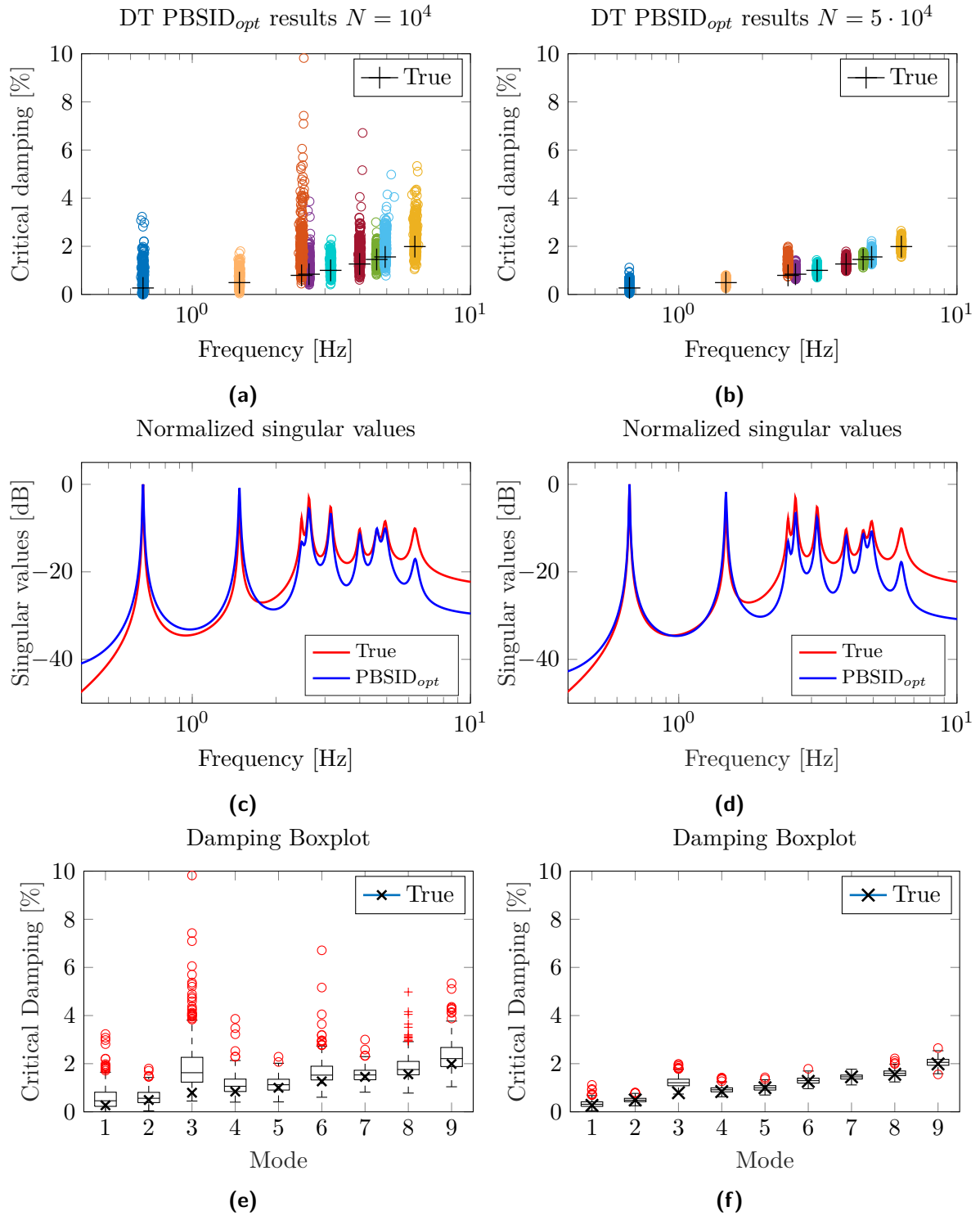
Figure 3-6: Identification results using the discrete-time PBSID$_{opt}$ algorithm from 400 Monte-Carlo simulations, sampled at $f_s = 100$ Hz, $\sigma_e^2/\sigma_y^2 = 0.1$ and $p, f = 300$.
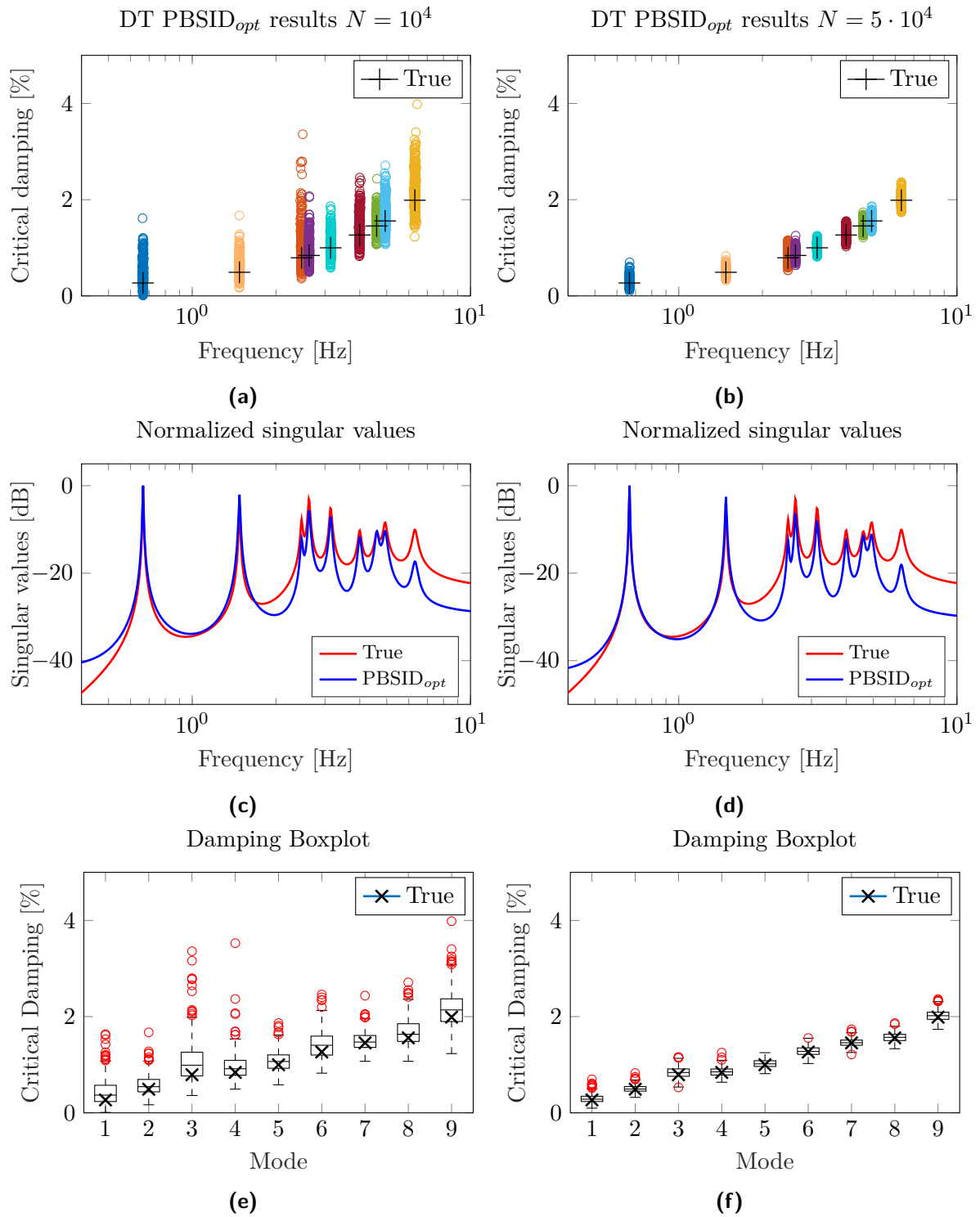
Figure 3-7: Identification results using the discrete-time PBSID$_{opt}$ algorithm from 400 Monte-Carlo simulations, sampled at $f_s = 50$ Hz, $\sigma_e^2/\sigma_y^2 = 0.1$ and $p, f = 300$.

Table 3-2: Means and standard deviations of the identification results from 400 Monte-Carlo simulations using the discrete-time PBSID$_{opt}$ algorithm, $f_s = 100$ Hz, $\sigma_e^2/\sigma_y^2 = 0.1$, $p, f = 300$, $N = 10^4$ (left) and $N = 5 \cdot 10^4$ (right).

	$N = 10^4$					$N = 5 \cdot 10^4$				
Mode	$\mu_f \pm \sigma_f$ [Hz]	ϵ_f [%]	$\mu_\zeta \pm \sigma_\zeta$ [%]	ϵ_ζ [%]	poles	$\mu_f \pm \sigma_f$ [Hz]	ϵ_f [%]	$\mu_\zeta \pm \sigma_\zeta$ [%]	ϵ_ζ [%]	poles
1	0.666 ± 0.003	0.03	0.591 ± 0.524	119.91	370	0.665 ± 0.001	0.00	0.337 ± 0.149	24.41	395
2	1.478 ± 0.004	0.02	0.610 ± 0.304	24.24	400	1.477 ± 0.002	0.01	0.494 ± 0.106	0.59	400
3	2.472 ± 0.017	0.03	1.911 ± 1.106	141.19	357	2.469 ± 0.005	-0.10	1.237 ± 0.218	56.05	400
4	2.629 ± 0.011	0.03	1.128 ± 0.426	34.17	399	2.630 ± 0.003	0.09	0.926 ± 0.137	10.12	400
5	3.146 ± 0.009	0.08	1.153 ± 0.321	15.31	400	3.143 ± 0.004	-0.02	1.003 ± 0.126	0.33	400
6	4.001 ± 0.016	0.12	1.653 ± 0.564	30.61	396	3.995 ± 0.006	-0.01	1.298 ± 0.148	2.60	400
7	4.605 ± 0.013	0.09	1.548 ± 0.302	6.50	400	4.601 ± 0.005	0.02	1.452 ± 0.117	-0.10	400
8	4.945 ± 0.032	0.26	1.864 ± 0.501	19.64	396	4.937 ± 0.007	0.05	1.607 ± 0.149	3.12	400
9	6.335 ± 0.039	0.39	2.311 ± 0.629	16.18	393	6.312 ± 0.012	0.02	2.059 ± 0.176	3.52	400

Table 3-3: Means and standard deviations of the identification results from 400 Monte-Carlo simulations using the discrete-time PBSID$_{opt}$ algorithm, $f_s = 50$ Hz, $\sigma_e^2/\sigma_y^2 = 0.1$, $p, f = 300$, $N = 10^4$ (left) and $N = 5 \cdot 10^4$ (right).

	$N = 10^4$					$N = 5 \cdot 10^4$				
Mode	$\mu_f \pm \sigma_f$ [Hz]	ϵ_f [%]	$\mu_\zeta \pm \sigma_\zeta$ [%]	ϵ_ζ [%]	poles	$\mu_f \pm \sigma_f$ [Hz]	ϵ_f [%]	$\mu_\zeta \pm \sigma_\zeta$ [%]	ϵ_ζ [%]	poles
1	0.665 ± 0.002	0.00	0.439 ± 0.285	63.44	397	0.665 ± 0.000	0.00	0.295 ± 0.089	9.76	400
2	1.478 ± 0.003	0.02	0.577 ± 0.205	17.56	400	1.477 ± 0.001	0.01	0.502 ± 0.074	2.28	400
3	2.471 ± 0.008	-0.02	1.063 ± 0.424	34.13	398	2.471 ± 0.003	0.00	0.843 ± 0.119	6.33	400
4	2.630 ± 0.007	0.06	0.961 ± 0.285	14.30	400	2.628 ± 0.002	0.01	0.858 ± 0.094	2.10	400
5	3.146 ± 0.007	0.08	1.078 ± 0.215	7.75	400	3.144 ± 0.003	0.02	1.020 ± 0.082	1.99	400
6	3.996 ± 0.012	0.00	1.421 ± 0.283	12.31	400	3.996 ± 0.004	0.01	1.284 ± 0.099	1.47	400
7	4.604 ± 0.009	0.07	1.495 ± 0.197	2.80	400	4.601 ± 0.004	0.02	1.461 ± 0.081	0.46	400
8	4.938 ± 0.013	0.07	1.672 ± 0.282	7.29	400	4.935 ± 0.005	0.00	1.570 ± 0.097	0.76	400
9	6.318 ± 0.025	0.12	2.168 ± 0.372	9.02	400	6.311 ± 0.008	0.01	2.022 ± 0.120	1.64	400

3-3-4   Identification with Resampled Simulation Data

In the previous section it was shown using the original uniformly sampled output data, that the modal parameters of the 9-DoF system could be accurately identified. When only non-uniformly sampled measurement data is available, one option is to resample the data with a constant sampling frequency. In order to see what kind of effect resampling has on the identification results, the previous identification experiment is repeated using resampled data sequences.

Resampled simulation data is obtained by first simulating the 9-DoF system using a sampling frequency of $f_s = 200$ Hz for a duration of 100 seconds, resulting in a data set of length $N = 2 \cdot 10^4$. Subsequently, half of the samples are randomly removed from this dataset so that a non-uniformly sampled signal with an average sampling frequency of $f_{s,avg} = 100$ Hz is obtained. This signal is then resampled at a constant sampling frequency of $f_{s,res} = 100$ Hz through linear interpolation in combination with an anti-aliasing low pass filter. In this way, the resampled simulation data has the same sampling frequency and length as in the previous section. It has to be noted that by increasing the sampling frequency of the initial simulation, a different input signal is used than in the previous section. The response resulting from this input signal is therefore also different. The results obtained using this simulation data are also influenced by this fact.

The resampling procedure as described above is repeated in order to also obtain data resampled at $f_{s,res} = 50$ Hz. The results of the Monte-Carlo simulations, using only datasets of length $N = 5 \cdot 10^4$, are presented in Figure 3-8 and Table 3-4. By comparing these results to those in Figures 3-6 and 3-7, it can be concluded that using resampled data for the identification procedure can decrease the accuracy and precision of the estimated eigenfrequencies and damping ratios. The data resampled at $f_{s,res} = 100$ Hz results in a higher variance and furthermore it can be seen that a large bias is introduced in the identified damping ratios for all modes. The results obtained with data resampled at $f_{s,res} = 50$ show smaller variance. However, a bias in the damping estimates can still be observed for several modes.

(a)

(b)

(c)

(d)
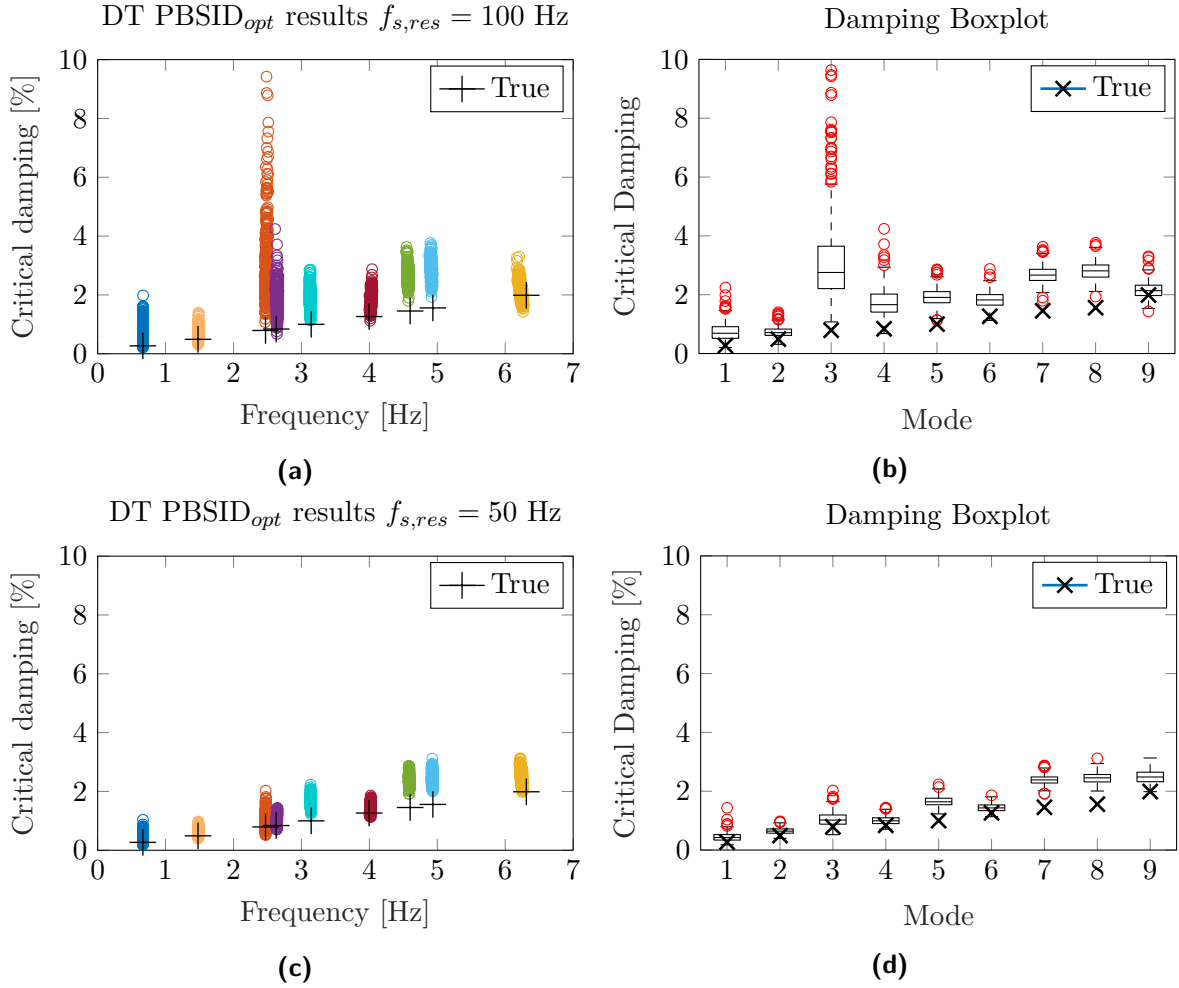
Figure 3-8: Identification results using the discrete-time PBSID$_{opt}$ algorithm from 400 Monte-Carlo simulations, $\sigma_e^2/\sigma_y^2 = 0.1$, $p, f = 300$ and $N = 5 \cdot 10^4$.

Table 3-4: Means and standard deviations of the identification results from 400 Monte-Carlo simulations using the discrete-time PBSID$_{opt}$ algorithm, $\sigma_e^2/\sigma_y^2 = 0.1$, $p, f = 300$, $N = 5 \cdot 10^4$, resampled at $f_{s,res} = 100$ Hz (left) and $f_{s,res} = 50$ Hz (right).

	$f_{s,res} = 100$ Hz					$f_{s,res} = 50$ Hz				
Mode	$\mu_f \pm \sigma_f$ [Hz]	ϵ_f [%]	$\mu_\zeta \pm \sigma_\zeta$ [%]	ϵ_ζ [%]	poles	$\mu_f \pm \sigma_f$ [Hz]	ϵ_f [%]	$\mu_\zeta \pm \sigma_\zeta$ [%]	ϵ_ζ [%]	poles
1	0.667 ± 0.001	0.19	0.738 ± 0.298	174.55	400	0.666 ± 0.001	0.10	0.446 ± 0.148	66.03	400
2	1.482 ± 0.002	0.31	0.735 ± 0.175	49.56	400	1.481 ± 0.001	0.21	0.648 ± 0.104	31.93	400
3	2.481 ± 0.012	0.40	3.167 ± 1.441	299.68	398	2.473 ± 0.003	0.09	1.053 ± 0.235	32.82	400
4	2.643 ± 0.008	0.59	1.743 ± 0.472	107.38	400	2.639 ± 0.003	0.41	1.004 ± 0.143	19.46	400
5	3.128 ± 0.006	-0.51	1.916 ± 0.306	91.61	400	3.138 ± 0.003	-0.17	1.652 ± 0.161	65.15	400
6	4.023 ± 0.007	0.69	1.841 ± 0.261	45.49	400	4.016 ± 0.005	0.50	1.436 ± 0.137	13.52	400
7	4.568 ± 0.007	-0.69	2.684 ± 0.270	84.59	400	4.586 ± 0.004	-0.32	2.387 ± 0.161	64.15	400
8	4.910 ± 0.008	-0.50	2.817 ± 0.306	80.76	400	4.926 ± 0.005	-0.18	2.453 ± 0.182	57.44	400
9	6.227 ± 0.017	-1.32	2.157 ± 0.277	8.45	400	6.240 ± 0.011	-1.12	2.500 ± 0.215	25.18	400

3-4   Conclusion

The goal of this chapter was to present the identification procedure incorporating the discrete-time PBSID_{opt} algorithm as visualized in Figure 3-1. Starting from a discrete-time state-space representation, the PBSID_{opt} algorithm was derived step by step. Additionally, it was shown how the PBSID_{opt} algorithm can be extended to allow the use of multiple batches of data. This procedure has the same effect as using longer datasets, thus improving the results of the identification procedure. Special attention was given to the choice of the past window parameter p, of which an initial estimate can be obtained using the AIC. By combining the PBSID_{opt} algorithm with a hierarchical clustering method, the identification procedure can be automated in obtaining a statistical analysis of the results.

In order to examine the performance of the PBSID_{opt} algorithm, the identification procedure was applied to a simulation example based on a 9-DoF system. First, the original simulation data with fixed sampling frequency was used. It was observed that accurate estimates of the frequency and damping could be obtained when long datasets were used. The choice of sampling frequency was also shown to have an effect on the identification results. In the case of the 9-DoF model, improved damping estimates were obtained using data sampled at a frequency of $f_s = 50$ Hz.

The performance of the PBSID_{opt} algorithm was also tested for non-uniformly sampled data which had been resampled. It was observed that the damping estimates were less accurate compared to the results obtained with the original simulation data. More specifically, a bias was introduced in the estimated damping of multiple modes. Therefore, it can be concluded that using non-uniformly sampled data which has been resampled can have a negative influence on the accuracy and precision of the estimated damping.

Chapter 4

Continuous-Time Predictor-Based Subspace Identification

In this chapter the continuous-time version of the Predictor-Based Subspace IDentification (PBSID) algorithm will be presented. Furthermore, it will be examined whether this identification method can be used to estimate the structural parameters of a system. The results obtained using non-uniformly sampled data are particularly of interest, since this is the same type of data as is taken from an Offshore Wind Turbine (OWT).

Obtaining a continuous-time model of a system can have several advantages over a discrete-time model. For instance, in engineering fields such as aircraft and rotorcraft identification the direct estimation of continuous-time parameters is important [4]. However, the physical meaning of these parameters is lost in a discrete-time representation. Another advantage of continuous-time methods is related to the sampling of the input-output data. In areas such as medicine and transport, the measuring instant can not be controlled, resulting in non-uniformly sampled data. A discrete-time model can not be used in this case, since it is based on a constant sampling frequency. This argument also applies to the model of the OWT in this thesis, for which only non-uniformly sampled measurement data is available.

There are multiple continuous-time identification methods to be found in literature, of which the Laguerre filtering and Laguerre projections approaches have been the topic of most studies. The former approach consists of a filtering operation on the measurement data using Laguerre filters. This approach was first presented in combination with Multivariable Output-Error State-sPace (MOESP) class algorithms by Haverkamp et al. [36, 37, 38, 39]. The Laguerre projection approach on the other hand is used to obtain a discrete-time equivalent system. Both approaches were first combined with the PBSID method by Bergamasco [4]. The performance of both methods was compared and it was found that the Laguerre projection approach in combination with the PBSID$_{opt}$ algorithm provided the best results in terms of accuracy and precision. This method will therefore be the focus of this chapter.

The entire continuous-time identification procedure that will be discussed in this chapter has been visualized in Figure 4-1, with each step referring to the corresponding section. In Section 4-1 the continuous-time state-space system on which the identification method is based

is presented. Next, it is shown in Section 4-2 how the original measurement data can be transformed using the Laguerre projections to obtain a Laguerre domain state-space description. Starting from this state-space description, the continuous-time variant of the PBSID$_{opt}$ algorithm is subsequently presented in Section 4-3. After this, some general implementation issues concerning this method are discussed in Section 4-4, as well as some additional issues that were experienced during the writing of this thesis. In order to test the performance of the new algorithm, it is applied to the 9-Degree of Freedom (DoF) system from Section 3-3-1. The results from these simulation experiments are presented in Section 4-5. Finally, in Section 4-6 conclusions are drawn concerning the performance the continuous-time PBSID algorithm compared to the performance of its discrete-time counterpart, thus examining which of the two PBSID algorithms is better equipped for the identification of an OWT.
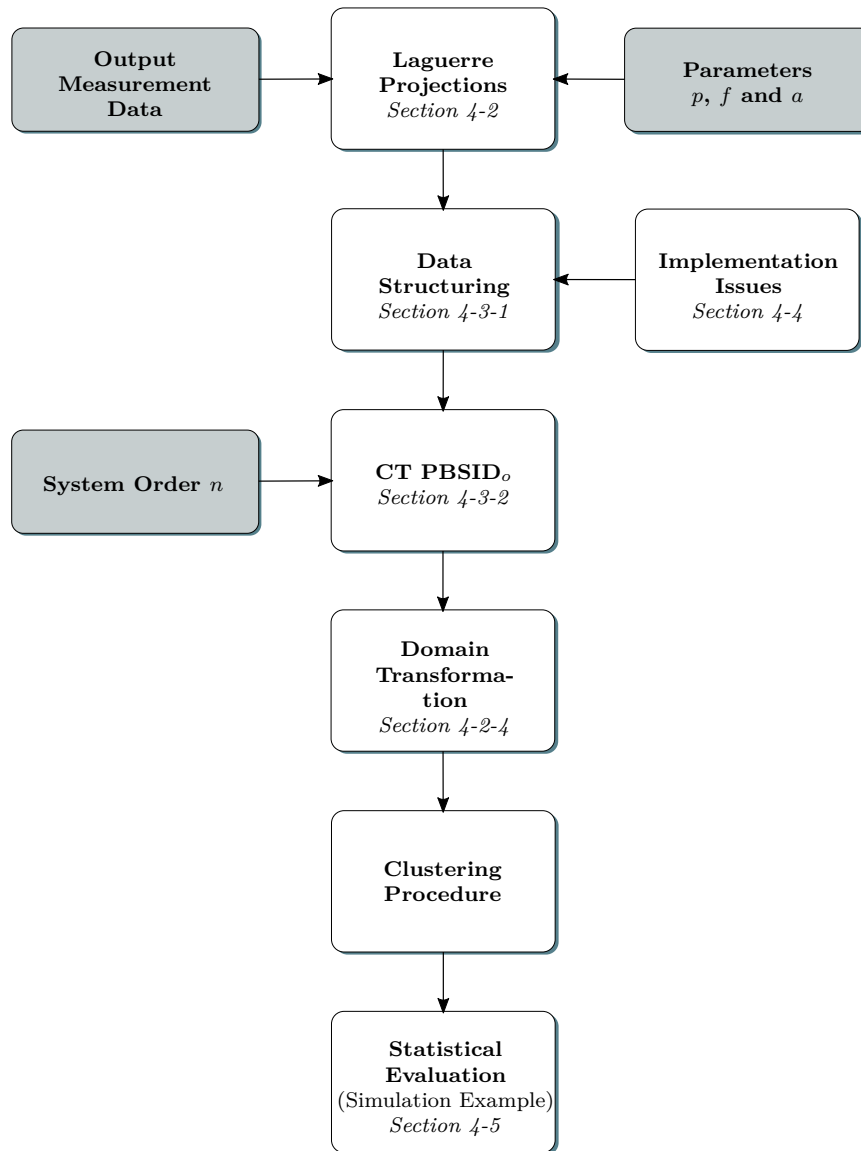
Figure 4-1: Flowchart of the continuous-time PBSID$_o$ procedure.

4-1   System Representation for Continuous-Time PBSID

This section will provide the basis for all continuous-time identification methods based on state-space systems. The continuous-time state-space representation is written as

$$dx(t) = Ax(t)dt + Bu(t)dt + dw(t), \qquad (4\text{-}1\text{a})$$

$$y(t)dt = Cx(t)dt + Du(t)dt + dv(t). \qquad (4\text{-}1\text{b})$$

Here the state sequence, input signal, output signal, the process noise and the measurement noise are respectively represented by the vectors $x(t) \in \mathbb{R}^n$, $u(t) \in \mathbb{R}^m$, $y(t) \in \mathbb{R}^\ell$, $w(t) \in \mathbb{R}^n$ and $v(t) \in \mathbb{R}^\ell$. In the continuous-time domain the process and measurement noise are modeled as Wiener processes [40], which is due to the fact that it is not possible to model a continuous-time white noise signal with finite variance [39]. The covariance matrix is given by

$$\mathbb{E}\left\{ \begin{bmatrix} dw(t) \\ dv(t) \end{bmatrix} \begin{bmatrix} dw(t) & dv(t) \end{bmatrix} \right\} = \begin{bmatrix} Q & S \\ S^T & R \end{bmatrix} dt. \qquad (4\text{-}2)$$

The system matrices A, B, C and D are assumed to be of appropriate dimensions, such that (A, C) is observable and $(A, \begin{bmatrix} B & Q^{\frac{1}{2}} \end{bmatrix})$ is controllable. Under these assumptions, the state-space representation for the continuous-time system in innovation form can be written as

$$dx(t) = Ax(t)dt + Bu(t)dt + Kde(t), \qquad (4\text{-}3\text{a})$$

$$y(t)dt = Cx(t)dt + Du(t)dt + de(t), \qquad (4\text{-}3\text{b})$$

where the innovation signal $e(t) \in \mathbb{R}^\ell$ is a Wiener process and the matrix K is the Kalman gain. Again, since Operational Modal Analysis (OMA) methods will be used, the innovation state-space system is reduced to

$$dx(t) = Ax(t)dt + Kde(t), \qquad (4\text{-}4\text{a})$$

$$y(t)dt = Cx(t)dt + de(t). \qquad (4\text{-}4\text{b})$$

In the case that a dataset $\{y(t_i)\}$, for $i = [1, \ldots, N]$, of possibly non-uniformly sampled measurement data is available, the goal is to find accurate estimates of the state space matrices A, C, and K up to a similarity transformation. However, if Subspace Model Identification (SMI) methods are applied directly, false results will be obtained. This is due to the fact that measurement data which is stored into Hankel matrix structures will return a discrete-time system when subspace identification algorithms are applied. In order to obtain Hankel matrices which will preserve the continuous-time properties of the data, some transformations will have to be applied to the measurement data beforehand. A possible solution would be to compute higher-order derivatives of the input-output data. However, this is not feasible for large data sets since it is very computationally intensive.

Literature offers some alternative methods for the transformation of the measurement data for subspace identification purposes. In the last two decades there has been an increased interest in this topic and a range of methods has been proposed. Two of these methods are the topic of most of the research concerning continuous-time identification. Both these methods use Laguerre filters to transform the original measurement data. Comparative analysis on a

simulation model showed that the method using Laguerre projections provided results with better accuracy [4]. Therefore, only the Laguerre projection approach will be discussed in this thesis.

Using Laguerre projections, the measurement data can be transformed and subsequently the PBSID$_{opt}$ algorithm discussed in Chapter 3 can be extended to the continuous-time domain. The next section will present the working principles of the Laguerre projections, and shows how an alternative discrete-time equivalent state-space system can be obtained.

4-2 Data Transformation Using Laguerre Projections

In this section it is shown how a discrete-time equivalent model is obtained starting from a continuous-time model. This transition is the result of a transformation of the input-output data based on the lifting technique [41]. With the help of Laguerre filters the lifting technique could be extended to obtain the so called Laguerre projections. This method was first presented by Ohta [42, 43, 44], where it was used in combination with MOESP class algorithms to test its performance. Next, the PBSID$_{opt}$ algorithm was extended to the continuous-time domain in combination with Laguerre projections by Bergamasco [45].

The lifting technique which forms the basis for the Laguerre projections is first discussed in Section 4-2-1. Next, the Laguerre filters that are used to compute the projections are introduced in Section 4-2-2. Finally, the Laguerre projections and the resulting discrete-time equivalent system are presented in Section 4-2-3.

4-2-1 Lifting Technique

The lifting technique can be seen as a method that represents a continuous-time system by an equivalent discrete-time system. This equivalent discrete-time system is obtained by decomposing the input and output space using the inner function $\phi(s) = e^{-sh}$, commonly known as the delay function. A function $\phi(s)$ is called an inner function if $\phi^T(j\omega)\phi(j\omega) = 1$ on the imaginary axis. The lifting technique is explained by Bergamasco [4] using the following state-space system

$$\dot{x}(t) = Ax(t) + Bu(t), \tag{4-5a}$$

$$y(t) = Cx(t) + Du(t). \tag{4-5b}$$

It is assumed that this system is stable and provides the input-output mapping $u \mapsto y$.

Instead of considering the state $x(t)$ only at sampling instants, a function piece θ is introduced during the sampling period as the state. The idea behind the lifting technique is then to see a signal $x(t)$ defined in a certain space, as a sequence of projections onto the basis of that space, such as is shown in Figure 4-2. The sequence of projections $\{x_k(\theta)\}_{k=1}^{\infty}$ can be defined as a discrete-time state transition rule given by

$$x_k(\theta) = x((k-1)h + \theta), \quad \theta \in (0, h]. \tag{4-6}$$
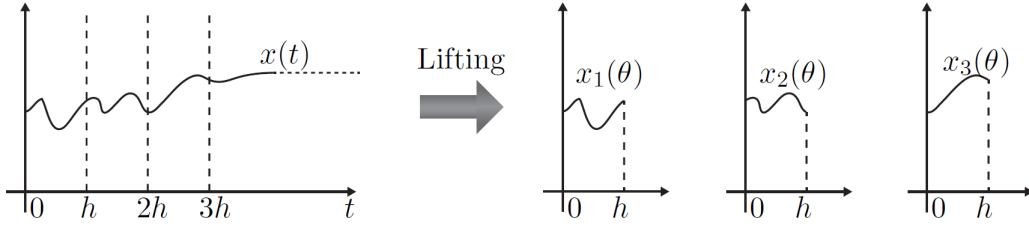
Figure 4-2: Projections of a signal $x(t)$ using the inner function $\phi(s) = e^{-sh}$ [4].

It can subsequently be shown that a new state-space system is obtained that has the same input-output correspondence as the system from Equation (4-5). According to Bergamasco [4], this system can be written as

$$x_{k+1} = Fx_k + Gu_{k+1}, \tag{4-7a}$$
$$y_k = Hx_k + Mu_k. \tag{4-7b}$$

The matrices of this state-space model represent the following operations

$$F : x(\theta) \mapsto e^{A\theta} x(h),$$
$$G : u(\theta) \mapsto \int_0^\theta e^{A(\theta-\tau)} Bu(\tau)d\tau,$$
$$H : x(\theta) \mapsto Cx(\theta),$$
$$M : u(\theta) \mapsto Du(\theta).$$

Note that on the right side of Equation (4-7a) the input term is given by u_{k+1} and not u_k. By introducing a new state variable

$$\xi_k = x_k - Gu_k,$$

the state trajectory and output can be rewritten as

$$\xi_{k+1} = F\xi_k + FGu_k, \tag{4-8a}$$
$$y_k = H\xi_k + (HG + M)u_k. \tag{4-8b}$$

The lifted system of Equation (4-5) is hence given as

$$\xi_{k+1} = A_d\xi_k + B_du_k, \tag{4-9a}$$
$$y_k = C_d\xi_k + D_du_k, \tag{4-9b}$$

where

$$A_d : \xi \mapsto e^{Ah}\xi,$$
$$B_d : u_k \mapsto \int_{-h}^0 e^{-A\tau} Bu_k(h+\tau)d\tau,$$
$$C_d : \xi \mapsto Ce^{A\theta}\xi, \quad \theta \in [0, h),$$
$$D_d : u_k \mapsto Du_k(\theta) + C \int_0^t e^{A(\theta-\tau)} Bu_k(\tau)d\tau.$$

In other words, the lifted system from Equation (4-9) describes the transition between one projection of the original signal to another projection. By repeating this step for every projection, the original signal can be obtained once again. Instead of looking at the data on fixed time intervals, the lifted system uses a part of the trajectory. Therefore, the available signals do not have to be equidistantly sampled in order to obtain a lifted system. This principle formed the inspiration for continuous-time identification using Laguerre projections. In later research it was shown that the idea of a lifted system is valid using any inner function [43]. Consequently, this allows the use of Laguerre filters to transform the input-output data and hence obtain a transformed system. These Laguerre filters are introduced in the next section.

4-2-2   Laguerre Filter

Laguerre filters are widely used in the field of system identification due to their orthonormal properties. The Laguerre filter is closely related to the first order all-pass filter, which is given by

$$w(s) = \frac{s - a}{s + a}. \tag{4-10}$$

Laguerre filters can be viewed as a single low-pass filter combined with a bank of all-pass filters. The transfer function of the i-th order Laguerre filter is given by

$$\mathcal{L}_i(s) = \sqrt{2a} \frac{(s - a)^i}{(s + a)^{i+1}}. \tag{4-11}$$

Choosing $a > 0$ results in a stable filter, while for $a < 0$ an unstable filter is obtained. In this thesis, $\ell_i(t)$ represents the impulse response function of the i-th order Laguerre filter. The impulse responses of the Laguerre filter are visualized in Figure 4-3 for multiple orders using a constant filter pole a.
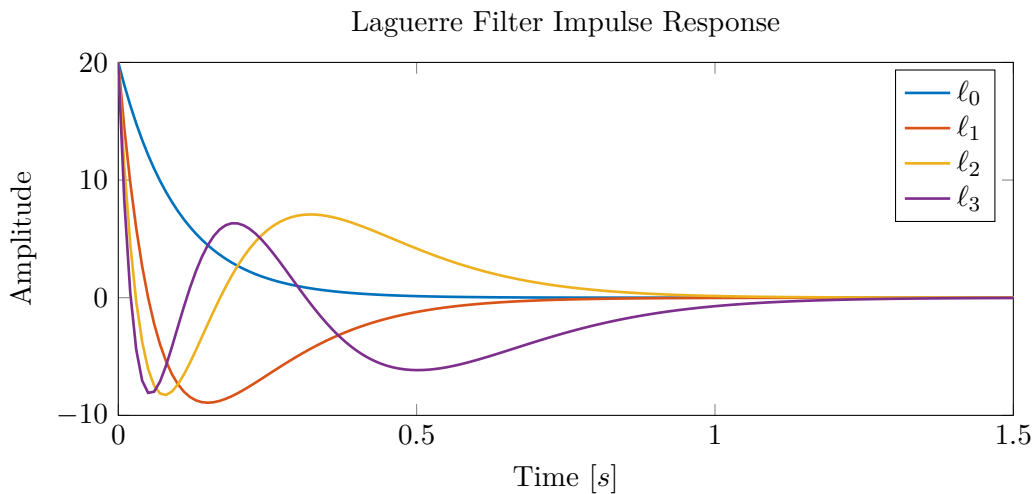
Figure 4-3: Impulse response of the Laguerre filter for multiple orders with Laguerre filter pole $a = 10$

It can be shown that the zero-th order Laguerre filter can be written as a function of the all-pass filter, such that

$$\mathcal{L}_0(s) = \frac{\sqrt{2a}}{s + a} = \frac{(1 - w(s))}{\sqrt{2a}}. \tag{4-12}$$

For notational simplicity, the modified Laguerre filter $L_i(s)$ is introduced with the following equation

$$L_i = 2a\frac{(s - a)^i}{(s + a)^{i+1}} = (1 - w(s))w(s)^i. \tag{4-13}$$

This filter is the same as the original Laguerre filter up to a constant factor $\sqrt{2a}$. Since the orthogonality property of the filter is not lost using the modified Laguerre filter, $L_i(s)$ will from here one be referred to as the Laguerre filter. The impulse response function $\ell_i(t)$ will consequently correspond to $L_i(s)$. In the next section it is shown how the Laguerre filters can be used to transform the system signals and obtain the corresponding transformed system.

4-2-3   Laguerre Projections

As stated before, it is possible to use any inner function in order to obtain a lifted system. Ohta showed that using the first order all-pass operator as inner function, a signal can be projected onto the k-th element of the orthonormal Laguerre basis [43]. As a result, a system is obtained with a state-space description in the Laguerre domain. In the case of output-only identification, the original system is described by Equation (4-4). The projections of the output and innovation signals are then given by

$$\tilde{y}(k) = \int_0^\infty \Lambda_w^k \ell_0(t)y(t)dt, \tag{4-14a}$$

$$\tilde{e}(k) = \int_0^\infty \Lambda_w^k \ell_0(t)de(t), \tag{4-14b}$$

where $\Lambda_w^k \ell_0(t)$ is the impulse response of the k-th Laguerre filter, meaning $\Lambda_w^k \ell_0(t) = \ell_k(t)$. Using the projections from Equation (4-14), the continuous-time system can be transformed to obtain the following state-space representation

$$\xi(k + 1) = A_o\xi(k) + K_o\tilde{e}(k), \quad \text{with } \xi(0) = 0, \tag{4-15a}$$

$$\tilde{y}(k) = C_o\xi(k) + \tilde{e}(k). \tag{4-15b}$$

These state-space matrices are related to the original continuous-time matrices from Equation (4-4) by

$$A_o = (A - aI)^{-1}(A + aI), \tag{4-16a}$$

$$C_o = -\sqrt{2a}C(A - aI)^{-1}, \tag{4-16b}$$

$$K_o = \sqrt{2a}(A - aI)^{-1}K. \tag{4-16c}$$

With the help of the Laguerre projections an equivalent discrete-time system has now been derived. This new system description allows the use of conventional subspace identification methods, by using the transformed measurement signals as input for the identification algorithms. In the next section, the PBSID$_{opt}$ algorithm from Chapter 3 will be reformulated for the Laguerre domain state-space description of Equation (4-15).

4-3 PBSID$_o$ Algorithm

The continuous-time PBSID algorithm proposed by Bergamasco [45] is commonly referred to as the PBSID$_o$ algorithm and will be presented in this section. First, the projections of the signals and the resulting state-space system are presented in Section 4-3-1. Here, the data equation that is used for the identification algorithm will also be derived. Second, the PBSID$_o$ algorithm is formulated in Section 4-3-2. The continuous-time algorithm has the same procedure as its discrete-time counterpart, it only differs in the matrices that make up the data equation.

4-3-1 Data Equation

In the case that output measurement data is available for time instants t_i, with $i = [1, \ldots, N]$, the following transformations on the output $y(t_i)$ and innovation signal $e(t_i)$ can be applied

$$\tilde{y}_i(k) = \int_0^\infty \Lambda_w^k \ell_0(\tau) y(t_i + \tau) d\tau, \tag{4-17a}$$

$$\tilde{e}_i(k) = \int_0^\infty \Lambda_w^k \ell_0(\tau) de(t_i + \tau). \tag{4-17b}$$

With these transformed signals the state-space representation in innovation form is given by

$$\xi_i(k+1) = A_o \xi_i(k) + K_o \tilde{e}_i(k), \quad \xi_i(0) = x(t_i), \tag{4-18a}$$

$$\tilde{y}_i(k) = C_o \xi_i(k) + \tilde{e}_i(k). \tag{4-18b}$$

Equivalent to the discrete-time case, this state-space system can be written in the predictor form

$$\xi_i(k+1) = \tilde{A}_o \xi_i(k) + K_o \tilde{y}_i(k), \quad \xi_i(0) = x(t_i), \tag{4-19a}$$

$$\tilde{y}_i(k) = C_o \xi_i(k) + \tilde{e}_i(k), \tag{4-19b}$$

where $\tilde{A}_o = A_o - K_o C_o$.

In order to apply the PBSID$_{opt}$ algorithm, the data equation of the transformed system has to be constructed first. For this purpose the stacked sample $\tilde{z}_i(k) = \tilde{y}_i(k)$ is introduced once more. The next step is to iterate the state update operation from Equation (4-19a) $p - 1$ times. The state equation is then obtained as

$$\xi_i(k+p) = \tilde{A}_o^p \xi_i(k) + \mathcal{K}^{(p)} Z_i^{0,p-1}, \tag{4-20}$$

where the extended controllability matrix is given by

$$\mathcal{K}^{(p)} = \begin{bmatrix} \tilde{A}_o^{p-1} K_o & \tilde{A}_o^{p-2} K_o & \cdots & K_o \end{bmatrix}, \tag{4-21}$$

and the stacked data vector is written as

$$Z_i^{0,p-1} = \begin{bmatrix} \tilde{z}_i(k) \\ \vdots \\ \tilde{z}_i(k+p-1) \end{bmatrix}. \tag{4-22}$$

Equivalent to the discrete-time case, it is assumed that the matrix $\tilde{A}_o$ has all its eigenvalues inside the unit circle and as a result the term $\tilde{A}_o^p \xi_i(k)$ can be neglected if p is chosen sufficiently large. Subsequently, the state equation can be reduced to

$$\xi_i(k+p) \simeq \mathcal{K}^{(p)} Z_i^{0,p-1}, \tag{4-23}$$

and the following output equation is obtained

$$\tilde{y}_i(k+p) \simeq C_o \mathcal{K}^{(p)} Z_i^{0,p-1} + \tilde{e}_i(k+p). \tag{4-24}$$

By iterating this output equation another f times, where f denotes the future window, the system can be written in matrix notation. For this purpose, the following matrices are introduced

$$Y_i^{p,f} = \begin{bmatrix} \tilde{y}_i(k+p) & \cdots & \tilde{y}_i(k+p+f) \end{bmatrix}, \tag{4-25a}$$

$$E_i^{p,f} = \begin{bmatrix} \tilde{e}_i(k+p) & \cdots & \tilde{e}_i(k+p+f) \end{bmatrix}, \tag{4-25b}$$

$$\Xi_i^{p,f} = \begin{bmatrix} \xi_i(k+p) & \cdots & \xi_i(k+p+f) \end{bmatrix}, \tag{4-25c}$$

$$\bar{Z}_i^{p,f} = \begin{bmatrix} Z_i^{0,p-1} & \cdots & Z_i^{f,p+f-1} \end{bmatrix}. \tag{4-25d}$$

The state space system in matrix form is then given by

$$\Xi_i^{p,f} \simeq \mathcal{K}^{(p)} \bar{Z}_i^{p,f}, \tag{4-26a}$$

$$Y_i^{p,f} \simeq C_o \mathcal{K}^{(p)} \bar{Z}_i^{p,f} + E_i^{p,f}. \tag{4-26b}$$

The final step is to form the Hankel-like matrices of the state, output and innovation signals. This can be done by transforming the entire dataset for $i = [1, \ldots, N]$ and for $k = [p, \ldots, p+f]$. In the case of the output signal y this results in the matrix

$$Y^{p,f} = \begin{bmatrix} \tilde{y}_1(k+p) & \cdots & \tilde{y}_N(k+p) & \cdots & \tilde{y}_1(k+p+f) & \cdots & \tilde{y}_N(k+p+f) \end{bmatrix}. \tag{4-27}$$

The matrices $E^{p,f}$, $\Xi^{p,f}$ and $\bar{Z}^{p,f}$ will have the same structure as $Y^{p,f}$. Using these matrices, the data equation can be written as

$$\Xi^{p,f} \simeq \mathcal{K}^p \bar{Z}^{p,f}, \tag{4-28a}$$

$$Y^{p,f} \simeq C_o \mathcal{K}^p \bar{Z}^{p,f} + E^{p,f}. \tag{4-28b}$$

It is observed that this data equation is very similar to the one from Equation (3-9), and can therefore be used as the basis for the continuous-time PBSID$_o$ algorithm. However, there a difference in the parameters p and f for the discrete-time and continuous-time cases. In the continuous-time case, p and f indicate the number of Laguerre filters that are used for the projections of the original signals.

4-3-2 PBSID$_o$ Algorithm

Now that a data equation for the transformed system has been derived, the PBSID$_{opt}$ algorithm can be applied using the equations that were presented in Chapter 3. For simplicity

reasons the past and future windows are again taken as $p = f$. First, the matrix $C_o \mathcal{K}^{(p)}$ is estimated by solving the least-squares problem from Equation (3-10). Next, the extended observability-times-controllability matrix is formed using the estimates of $C_o \mathcal{K}^{(p)}$, resulting in

$$\Gamma^p \mathcal{K}^{(p)} \simeq \begin{bmatrix} C_o \tilde{A}_o^{p-1} \bar{B}_o & C_o \tilde{A}_o^{p-2} \bar{B}_o & \cdots & C_o \bar{B}_o \\ 0 & C_o \tilde{A}_o^{p-1} \bar{B}_o & \cdots & C_o \tilde{A}_o \bar{B}_o \\ \vdots & \vdots & \ddots & \vdots \\ 0 & 0 & \cdots & C_o \tilde{A}_o^{p-1} \bar{B}_o \end{bmatrix}. \tag{4-29}$$

Subsequently, the relation

$$\Gamma^p \Xi^{p,p} \simeq \Gamma^p \mathcal{K}^{(p)} \bar{Z}^{p,p} \tag{4-30}$$

is used to find an estimate of the state sequence $\Xi^{p,p}$ with the help of a singular value decomposition. Following this step, the matrix C_o can be estimated by solving a least-squares problem similar to Equation (3-19). With C_o available, an estimation of the innovation data matrix $E^{p,p}$ can be made. The final step of the identification algorithm involves the least-squares problem from Equation (3-21), in which the matrices A_o and K_o are obtained. The continuous-time system matrices A, C and K are subsequently computed using the relations given in Equation (4-16).

Starting from the continuous-time data equation, the steps of the PBSID$_o$ algorithm are basically the same as it discrete-time counterpart. Hence, for the most part it should be possible to apply this part of the algorithm without any issues. However, the computation of the Laguerre projections is not so straightforward and several issues can be experienced during this step. The next section will present some of the difficulties that are faced when computing the Laguerre projections of a measurement signal.

4-4   Implementation Issues of the PBSID$_o$ Algorithm

When computing the Laguerre projections of a signal there are several issues that can be experienced in the process. First, as will be explained in Section 4-4-1, it is not possible to directly compute the Laguerre projections using the equations presented Section 4-3. Second, in the case of non-uniformly sampled measurement data, the computation of the Laguerre projections is even more troublesome. A solution for this problem is presented in Section 4-4-2. Finally, Section 4-4-3 discusses numerical problems that might be experienced in some cases using the PBSID$_o$ algorithm.

4-4-1   General Implementation Issues

One of the problems that is experienced when computing the Laguerre projections, is that the convolution integral from Equation (4-17) has an infinite horizon. Obviously, it is not possible to perform this convolution integral, since only a finite amount of data is available from measurements. In order to solve this problem, an alternative transformation is presented that approximates the infinity integral [45]. This alternative implementation uses a sliding window with size equal to half of the dataset to approximate the infinity integral and can be

written as

$$\tilde{y}_i(k) = \int_0^\infty \Lambda_w^k \ell_0(\tau) y(t_i + \tau) d\tau = \int_{t_i}^\infty \Lambda_w^k \ell_0(\tau - t_i) y(\tau) d\tau =$$

$$\simeq \int_{t_i}^{t_N/2 + t_i} \Lambda_w^k \ell_0(\tau - t_i) y(\tau) d\tau. \tag{4-31}$$

Unfortunately, this approximation does introduce an error which is a function of the impulse response of the Laguerre basis and the length of the dataset. It was found that increasing the length of the dataset, decreasing the maximum Laguerre filter order, or increasing the Laguerre filter pole a resulted in reducing this error [4]. An efficient implementation of the convolution from Equation (4-31) is given by Bergamasco as

$$\tilde{y}_i(k) = \int_0^{t_N - t_i} \Lambda_w^k \ell_0((t_N - t_i) - \eta) m(\eta) d\eta, \tag{4-32}$$

where $m(t) = y(t_N - t)$, $\eta = t_N - \tau$ and $d\eta = -d\tau$. This can be viewed as the convolution between the k-th order Laguerre filter and a signal $y(t)$ that has been flipped in time. Equivalent to Equation (4-31), only the part of the convolution integral computed with at least half of the data length, meaning with $i = [1, \ldots, \frac{N}{2}]$, is retained.

Another issue that is encountered with the computation of Laguerre projections, is that the signals are assumed to be continuous-time. However, when dealing with real systems, only information on sampled instants is obtained and so it is necessary to discretize the Laguerre filters as well. A similar issue is seen in the case of continuous-time identification in combination with Laguerre filtering.

A detailed study on the effects of Laguerre filter discretization for the Laguerre filtering approach was performed by Haverkamp [39]. It was found that a Tustin transformation could be applied to provide a discrete-time equivalent of the Laguerre filters. However, it was also shown that discretization of the filters leads to a perturbation of the estimated column space of the extended observability matrix. This perturbation subsequently leads to a bias in the estimates of the system matrices. The resulting bias is related to the sampling interval as well as the system under study itself. Using a higher sampling frequency will lead to a smaller bias. Unfortunately, a detailed study on the effects of filter discretization using Laguerre projections is not available in literature. However, it is expected that the results will be similar to those obtained using the Laguerre filtering approach.

Finally, a comment is provided on the choice of the past and future window sizes. Apart from the necessary conditions that were given in Section 3-2-4, another constraint can be placed on the maximum size of the past window p. By looking at the impulse responses of the Laguerre filters in Figure 4-3, it can be observed that the settling time is a function of the filter order. By increasing the filter order k, the settling time of its impulse response is also increased. The computation of the Laguerre projections requires the convolution of these impulse responses with a dataset of finite length. This means that the settling time of the impulse responses is bounded by the length of the dataset. Considering the filter

$$\mathcal{L}_k(s) = \sqrt{2a} \frac{(s-a)^k}{(s+a)^{k+1}}, \tag{4-33}$$

the settling time can be approximated by $t_s = (5 + 2k)/a = (5 + 4p)/a$ for $k = 2p$. Hence, a rough guideline for the choice of p is given by

$$p \leq (aT/2 - 5)/4 \simeq (1/8)(T/\tau - 1), \tag{4-34}$$

where T denotes the duration of a dataset and $\tau = 1/a$ [45].

4-4-2   Laguerre Projections of Non-Uniformly Sampled Data

In the previous section it was stated that an efficient computation of the Laguerre projections could be performed using Equation (4-32). Indeed, this convolution integral can easily be computed in MATLAB, e.g. using the function **lsim**. This operation can be explained using an arbitrary system $H(s)$, as seen in Figure 4-4, which maps an input $u(s)$ to an output $y(s)$. In the time-domain, the output of this system is given by the convolution

$$y(t) = \int_0^t h(t - \tau)u(\tau)d\tau, \tag{4-35}$$

where $h(t)$ represents the impulse response function of transfer function matrix $H(s)$. Similarly the time response of the system can be computed using a state-space representation of $H(s)$. The transfer function matrix is related to the state-space form by

$$H(s) = C(sI - A)^{-1}B + D. \tag{4-36}$$

Consequently, the convolution from Equation (4-35), can be computed by simulating $H(s)$ as a state-space system. In order to compute the Laguerre projections using Equation (4-32), the Laguerre filters are rewritten to their state-space form and subsequently simulated using the original measurement signal as input. Prior to the simulation the state-space form of the Laguerre filters needs to be discretized, since the measurement data is not a continuous signal.
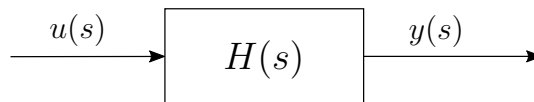
Figure 4-4: Input-output relation of an arbitrary plant $H(s)$.

The method for computing the Laguerre projections that was described just now is straightforward when a uniformly sampled data set is available. This is because the Laguerre filters can be discretized for the sampling interval of the dataset. However, when the dataset which is to be transformed has non-uniform sampling intervals, this approach is not directly possible. Although literature on continuous-time identification often refers to the possibilities of identification using non-uniformly sampled data, a straightforward method for computing the Laguerre projections of such data is not provided. Therefore, an approximation of the Laguerre projections using non-uniformly sampled data is presented in this thesis.

In order to compute the Laguerre projections for non-uniformly sampled data, a variable step size simulation algorithm is devised. This simulation algorithm uses state-space matrices discretized for every sampling interval present in the data. The discretization is done in MATLAB using the Tustin/Bilinear transformation, which has the following relations between

the continuous-time and discrete-time state-space matrices

$$A_d = (I + \frac{h}{2}A)(I - \frac{h}{2}A)^{-1}, \tag{4-37a}$$

$$B_d = h \cdot (I - \frac{h}{2}A)^{-1}B, \tag{4-37b}$$

$$C_d = C(I - \frac{h}{2}A)^{-1}, \tag{4-37c}$$

$$D_d = \frac{h}{2} \cdot C(I - \frac{h}{2}A)^{-1}B + D. \tag{4-37d}$$

In this case h represents the current sampling interval and the subscript d refers to the discrete-time domain. The variable step size simulation algorithm is given in Table 4-1.

Table 4-1: Simulation of a system using non-uniformly sampled data

Algorithm simulation with non-uniformly sampled signals

1. Read out all sampling intervals h_i of a non-uniformly sampled signal $\{u(t_i)\}_{i=1}^N$.

2. Discretize the continuous-time state-space matrices for every sampling interval using Equation (4-37).

3. For $i = 1 \ldots N$, compute the discrete states

$$x(t_i) = A_d^{h_i} x(t_{i-1}) + B_d^{h_i} u(t_i), \quad x(t_0) = 0.$$

4. Use the discrete states to compute the output at time t_i for $i = 1 \ldots N$.

$$y(t_i) = C_d^{h_i} x(t_i) + D_d^{h_i} u(t_i).$$

By supplying discretized Laguerre filters along with a non-uniformly sampled data sequence to the new simulation algorithm, an approximation of the real Laguerre projections can be obtained. In order to demonstrate the algorithm, a sinusoidal input signal sampled at $f_s = 1000$ Hz is supplied to the variable step simulation algorithm. First, the 0-th order Laguerre filter $L_0(s)$ is simulated using the uniformly-sampled input signal. Next, random samples are removed from the input signal such that a non-uniformly sampled signal containing 75% of the original data is obtained. The output is subsequently computed using the simulation algorithm. Finally, random samples are removed once more to obtain a non-uniformly sampled signal containing approximately 50% of the original data. The input signal and the resulting output signals are presented in Figure 4-5. It can be observed that even though a large part of the original signal is removed, a reasonable approximation of the uniformly sampled output can still be obtained. Still, this approximation introduces an error in the computation of the

Laguerre projections, which will undoubtedly have an effect on the identification results from the PBSID$_o$ algorithm.
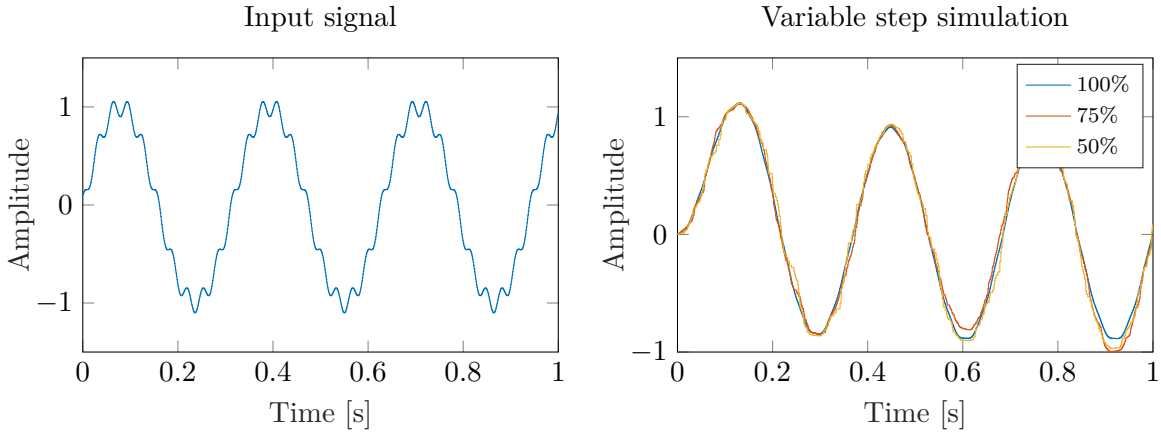
Figure 4-5: Sinusoidal input signal sampled at $f_s = 1000$ Hz (left) and output of the system L_0 using uniformly and non-uniformly sampled data as input (right).

In the previous example a relatively high sampling frequency was used. It is expected that the error of the variable step simulation output will decrease when even higher sampling frequencies are used. This is because for higher sampling frequencies the sampled input signal is approximating the real continuous-time signal. However, when a lower sampling frequency is used to obtain a signal, the output computed with a non-uniformly sampled input signal will probably contain larger errors as a result of discretization errors. In order to test if this is indeed the case, the same input signal as in the previous example is now sampled at $f_s = 200$ Hz. The variable step simulation algorithm is then applied in the same manner as before, resulting in the outputs given in Figure 4-6.
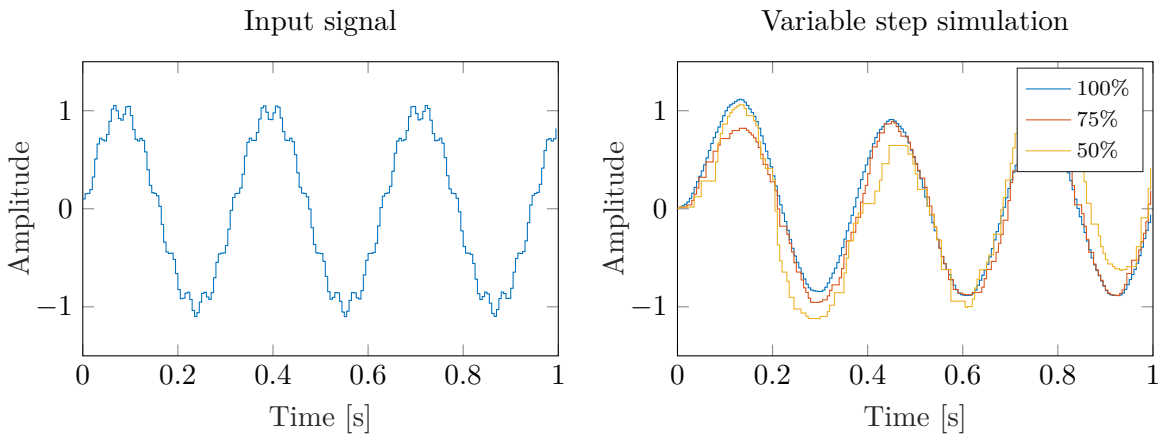
Figure 4-6: Sinusoidal input signal sampled at $f_s = 200$ Hz (left) and output of the system L_0 using uniformly and non-uniformly sampled data as input.

Indeed it can be seen that the outputs of the system simulated using non-uniformly sampled signals deviate more from the uniformly sampled output than in the case of with sampling

frequency of $f_s = 1000$ Hz. By increasing the amount of data that is removed these errors grow even larger. Therefore, it seems that the computation of the Laguerre projections becomes less accurate for lower sampling frequencies and when large gaps in a non-uniformly sampled signal are present. Consequently, it is expected that applying the continuous-time PBSID$_o$ algorithm to a non-uniformly sampled dataset with a relatively low average sampling frequency, will have a negative effect on the accuracy of the estimated state-space system.

The results obtained in this section together together with the comments given in Section 4-4-1, show us that the performance of the continuous-time PBSID$_o$ algorithm is very dependent on the sampling intervals of the measurement data. While discretization errors resulting from large sampling intervals lead to a bias in the estimated state-space matrices, this effect is amplified even more when non-uniformly sampled data is used. In order to have clear view on these effects, the PBSID$_o$ will be applied to a simulation example further on in this chapter.

4-4-3 Computational Issues

Apart from all the implementation issues that were discussed in the previous two sections, it is also possible to run into a different kind of problem using the PBSID$_o$ algorithm. In general, SMI methods require a large amount of data in order to provide an accurate estimate of a system model. As a result, this can sometimes lead to long computation times. In the case of continuous-time identification, computation time is increased even more.

The computation time of the PBSID$_o$ algorithm is related to the length of the original dataset and to the past and future windows. For continuous-time identification, the parameters p and f indicate the amount of Laguerre projections that are to be computed. This means that filters up to an order of $s = p + f + 1$ are used to perform the data transformations. Subsequently, all these projections are stored in a Hankel-like matrix such as in Equation (4-27). Comparing this to the discrete-time PBSID$_{opt}$ algorithm, it is seen that the Hankel matrices are many times larger in the continuous-time domain.

In this thesis, the identification using the PBSID$_o$ algorithm is done offline and therefore longer computation times are not directly an issue. However, there is a limit to the computing power and the maximum amount of data available in MATLAB. Thus, it can occur that the continuous-time identification algorithm breaks down when a complex system is estimated, which requires a long dataset and a large amount of projections.

4-5 Simulation Example for the PBSID$_o$ Algorithm

The previous sections discussed a number of implementation issues for the computation of the Laguerre projections. In order to overcome some of these problems it is necessary to make compromises. The result is that the continuous-time identification procedure introduces errors that are absent in the discrete-time counterpart. The effects of these errors on the identification results will be assessed in this section.

In order to demonstrate the PBSID$_o$ algorithm, it is applied to both uniformly and non-uniformly sampled data. This data is obtained from simulations of the 9-DoF system in Chapter 3. The system has been simulated multiple times using different sampling frequencies so that the effect of the sampling period on the perturbation of the estimated system

matrices may be observed. The identification procedure is first applied to uniformly sampled measurement data in Section 4-5-1. Next, samples are removed from the uniformly sampled datasets in Section 4-5-2, after which the identification procedure is repeated. It is then possible to compare the identification results using uniformly and non-uniformly sampled data. Furthermore, it is possible to compare the performance of the continuous-time identification algorithm with that of the discrete-time variant. Especially the performance using resampled data is of interest, since this is the alternative to continuous-time identification using non-uniformly sampled data.

4-5-1   Identification with Uniformly Sampled Data

In this section the identification results using the continuous-time PBSID_o algorithm, applied to the original simulation data, are presented. Equivalent to Chapter 3, a Monte-Carlo simulation consisting of 400 runs is performed to generate the simulation data. Next, the PBSID_o algorithm is applied to each of these data sequences. For this purpose, several new functions were included to the PBSID-toolbox [30]. The estimated poles are subsequently grouped using the clustering algorithm. In doing so, the average and standard deviation of each cluster can be computed.

The Monte-Carlo simulations were performed using $N = 5 \cdot 10^4$ samples for three different sampling frequencies, i.e. $f_s = 200$, 100 and 50 Hz. After the simulation of the system, white Gaussian noise was added to the output signals such that a signal-to-noise ratio of $\sigma_e^2/\sigma_y^2 = 0.1$ was obtained. The frequency and damping values obtained from the Monte-Carlo simulations are presented in Figure 4-7 and Tables 4-2 to 4-4.

Using a sampling frequency of $f_s = 200$ Hz results in a large variance in the estimated damping. It can be observed as well that the PBSID_o algorithm was unable to identify the third mode of the 9-DoF system. Recalling the results from Section 3-3, it was already difficult to identify this mode properly in the discrete-time domain.

By observing Figures 4-7c and 4-7e, it can be concluded that lowering the sampling frequency has a positive effect on the variance of the damping estimates. However, it can also be observed that the frequencies of the higher modes show an increased bias as the sampling frequency is lowered. This effect was explained Section 4-4-1 and is a result of discretization errors of the Laguerre filters.

Overall it can be concluded that the identification of the 9-DoF system using uniformly sampled data provides the best results when the discrete-time PBSID_{opt} algorithm is used. By comparing the results from this section with those from Section 3-3-3, it is seen that the discrete-time algorithm provides lower variance of the estimated damping and gives unbiased frequency estimates at lower sampling frequencies. In order to see if the PBSID_{opt} method also provides better results when the data is resampled, its results are compared to those obtained using the PBSID_o algorithm to non-uniformly sampled data. The identification results using non-uniformly sampled data are presented in the next section.

Figure 4-7: Identification results using the continuous-time PBSID$_o$ algorithm from 400 Monte-Carlo simulation, $\sigma_e^2/\sigma_y^2 = 0.1$, $p, f = 30$, $a = 30$ and $N = 5 \cdot 10^4$.

Table 4-2: Means and standard deviations of the identification results from 400 Monte-Carlo simulations using the continuous-time PBSID$_o$ algorithm, $f_s = 200$ Hz, $\sigma_e^2/\sigma_y^2 = 0.1$, $p, f = 30$, $a = 30$ and $N = 5 \cdot 10^4$.

Mode	$\mu_f \pm \sigma_f$ [Hz]	ϵ_f [%]	$\mu_\zeta \pm \sigma_\zeta$ [%]	ϵ_ζ [%]	poles
1	0.666 ± 0.003	0.09	0.662 ± 0.516	146.01	391
2	1.477 ± 0.004	-0.01	0.602 ± 0.284	22.64	400
3	-	-	-	-	-
4	2.601 ± 0.012	-1.02	1.194 ± 0.245	41.98	400
5	3.148 ± 0.009	0.16	1.268 ± 0.312	26.81	400
6	4.000 ± 0.014	0.03	1.662 ± 0.423	31.37	400
7	4.607 ± 0.014	0.15	1.632 ± 0.404	12.27	400
8	4.938 ± 0.020	0.07	1.878 ± 0.811	20.51	399
9	6.329 ± 0.034	0.29	2.521 ± 0.733	26.76	400

Table 4-3: Means and standard deviations of the identification results from 400 Monte-Carlo simulations using the continuous-time PBSID$_o$ algorithm, $f_s = 100$ Hz, $\sigma_e^2/\sigma_y^2 = 0.1$, $p, f = 30$, $a = 30$ and $N = 5 \cdot 10^4$.

Mode	$\mu_f \pm \sigma_f$ [Hz]	ϵ_f [%]	$\mu_\zeta \pm \sigma_\zeta$ [%]	ϵ_ζ [%]	poles
1	0.666 ± 0.001	0.03	0.601 ± 0.352	123.64	400
2	1.478 ± 0.002	0.04	0.554 ± 0.174	12.89	400
3	-	-	-	-	-
4	2.607 ± 0.008	-0.80	1.195 ± 0.176	42.18	400
5	3.157 ± 0.006	0.45	1.232 ± 0.233	23.18	400
6	4.010 ± 0.009	0.35	1.652 ± 0.288	30.59	400
7	4.631 ± 0.009	0.67	1.602 ± 0.203	10.21	400
8	4.963 ± 0.012	0.58	1.726 ± 0.358	10.77	400
9	6.392 ± 0.022	1.29	2.421 ± 0.352	21.72	399

Table 4-4: Means and standard deviations of the identification results from 400 Monte-Carlo simulations using the continuous-time PBSID$_o$ algorithm, $f_s = 50$ Hz, $\sigma_e^2/\sigma_y^2 = 0.1$, $p, f = 30$, $a = 30$ and $N = 5 \cdot 10^4$.

Mode	$\mu_f \pm \sigma_f$ [Hz]	ϵ_f [%]	$\mu_\zeta \pm \sigma_\zeta$ [%]	ϵ_ζ [%]	poles
1	0.666 ± 0.001	0.05	0.636 ± 0.266	136.66	400
2	1.482 ± 0.002	0.27	0.545 ± 0.116	11.50	400
3	-	-	-	-	-
4	2.626 ± 0.006	-0.09	1.308 ± 0.153	55.57	400
5	3.191 ± 0.004	1.51	1.256 ± 0.161	25.56	400
6	4.079 ± 0.014	2.07	1.823 ± 0.260	44.10	400
7	4.731 ± 0.006	2.85	1.711 ± 0.147	17.71	400
8	5.096 ± 0.018	3.26	2.257 ± 0.807	44.85	400
9	6.599 ± 0.053	4.57	3.234 ± 1.341	62.59	399

4-5-2 Identification with Non-Uniformly Sampled Data

In this section the performance of the continuous-time PBSID$_o$ algorithm is tested using non-uniformly sampled datasets. These datasets are obtained by randomly removing half of the samples from a uniformly sampled data sequence. The uniformly sampled data that was used for this operation is the same as in the previous section. The distribution of the non-uniformly sampled data is visualized in Figure 4-8. These datasets were created in such a way that the average sampling intervals are equal to those used in Section 4-5-1. For comparative reasons, the same parameters p, f and a were used for the PBSID$_o$ algorithm.
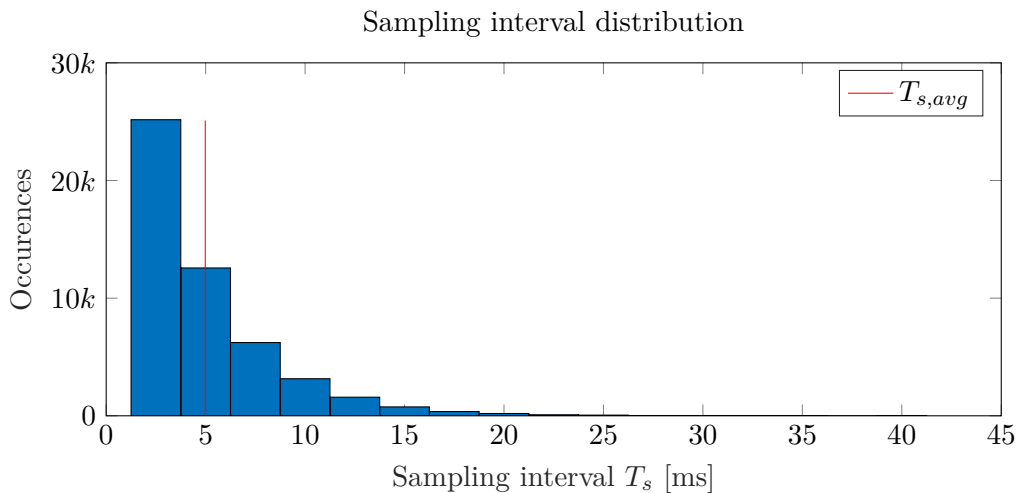
Figure 4-8: Distribution of the sampling intervals from a non-uniformly sampled dataset where half of the original samples has been removed at random.

The identification results of the Monte-Carlo simulation are presented in Figure 4-9 and Tables 4-5 to 4-7. It can be observed that using an average sampling frequency of $f_s = 200$ Hz, the PBSID$_o$ algorithm is able to accurately estimate the systems eigenfrequencies from non-uniformly sampled measurements. However, the variance of the estimated damping values is higher than in the case of uniformly sampled data.

Next, it can be seen that lowering the average sampling has a positive effect on the variance of the damping estimates. As expected though, a bias can be observed as well in the estimated eigenfrequencies of the higher modes. This phenomenon was seen in the previous section as well and is explained in Section 4-4-1. In the case of non-uniformly sampled data, the perturbation in the state-space matrices resulting from discretization errors is seen to be even larger. This can be explained by looking at the sampling interval distribution from Figure 4-8, where the biggest sampling interval is seen to be many times higher than the average sampling frequency. These higher sampling periods are causing the bias in the estimated frequencies to be even larger than before.
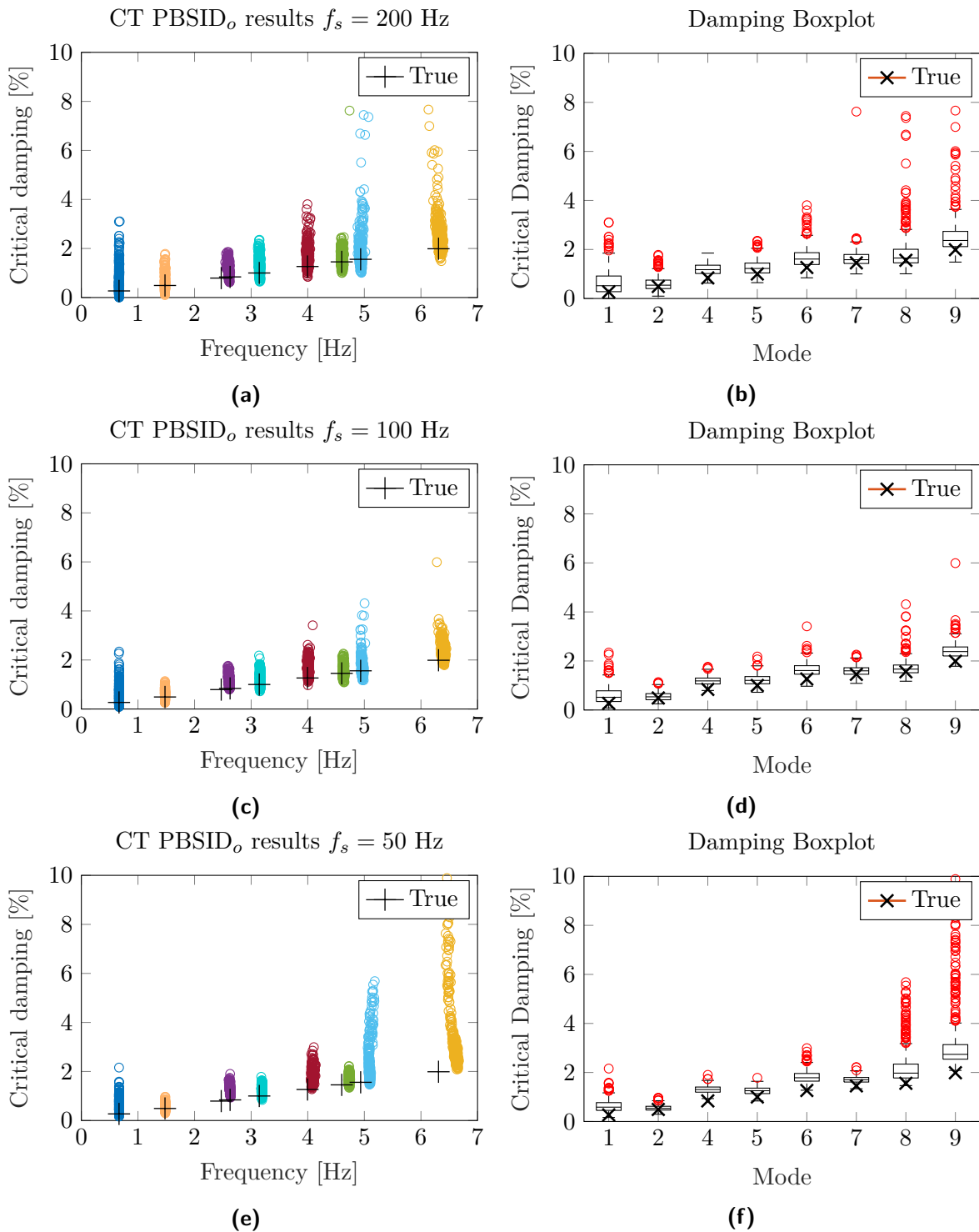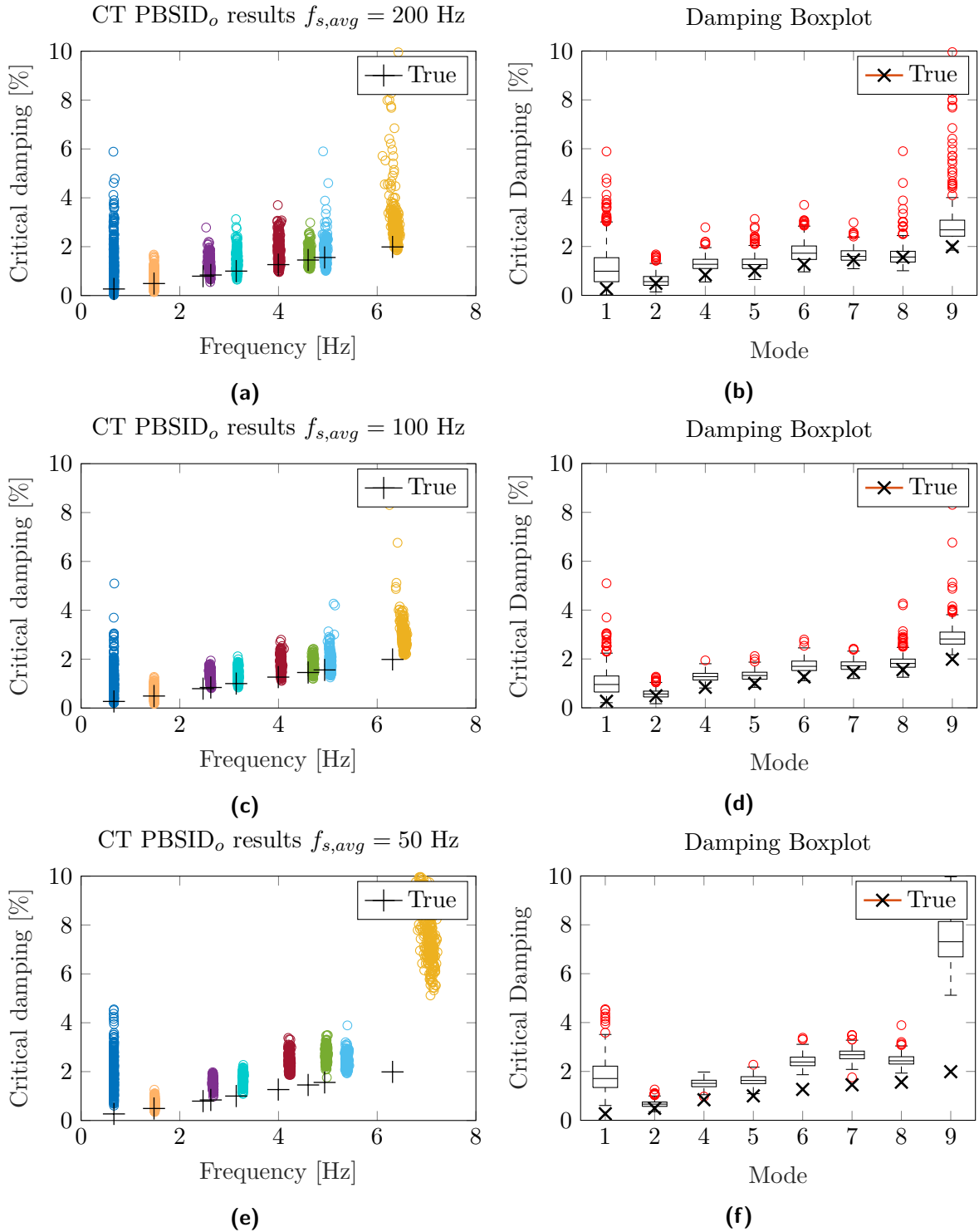
Figure 4-9: Identification results using the continuous-time PBSID$_o$ algorithm from 400 Monte-Carlo simulations, $\sigma_e^2/\sigma_y^2 = 0.1$, $p, f = 30$, $a = 30$ and $N = 5 \cdot 10^4$.

Table 4-5: Means and standard deviations of the identification results from 400 Monte-Carlo simulations using the continuous-time PBSID$_o$ algorithm, average $f_s = 200$ Hz, $\sigma_e^2/\sigma_y^2 = 0.1$, $p, f = 30$, $a = 30$, $N = 5 \cdot 10^4$.

Mode	$\mu_f \pm \sigma_f$ [Hz]	ϵ_f [%]	$\mu_\zeta \pm \sigma_\zeta$ [%]	ϵ_ζ [%]	poles
1	0.665 ± 0.003	-0.09	1.188 ± 0.863	341.92	400
2	1.478 ± 0.004	0.04	0.613 ± 0.283	24.83	400
3	-	-	-	-	-
4	2.603 ± 0.013	-0.96	1.290 ± 0.291	53.49	400
5	3.158 ± 0.009	0.46	1.320 ± 0.344	31.93	400
6	4.007 ± 0.013	0.29	1.774 ± 0.430	40.24	400
7	4.626 ± 0.012	0.57	1.636 ± 0.284	12.49	400
8	4.955 ± 0.015	0.41	1.654 ± 0.468	6.109	400
9	6.361 ± 0.051	0.80	2.926 ± 1.050	47.11	399

Table 4-6: Means and standard deviations of the identification results from 400 Monte-Carlo simulations using the continuous-time PBSID$_o$ algorithm, average $f_s = 100$ Hz, $\sigma_e^2/\sigma_y^2 = 0.1$, $p, f = 30$, $a = 30$, $N = 5 \cdot 10^4$.

Mode	$\mu_f \pm \sigma_f$ [Hz]	ϵ_f [%]	$\mu_\zeta \pm \sigma_\zeta$ [%]	ϵ_ζ [%]	poles
1	0.665 ± 0.002	-0.02	1.054 ± 0.601	292.11	400
2	1.481 ± 0.003	0.20	0.582 ± 0.190	18.50	400
3	-	-	-	-	-
4	2.619 ± 0.009	-0.33	1.283 ± 0.201	52.62	400
5	3.182 ± 0.006	1.23	1.328 ± 0.223	32.81	400
6	4.052 ± 0.009	1.41	1.731 ± 0.281	36.82	400
7	4.700 ± 0.010	2.18	1.738 ± 0.224	19.55	400
8	5.049 ± 0.014	2.32	1.868 ± 0.340	19.88	400
9	6.537 ± 0.034	3.59	2.923 ± 0.614	46.99	397

Table 4-7: Means and standard deviations of the identification results from 400 Monte-Carlo simulations using the continuous-time PBSID$_o$ algorithm, average $f_s = 50$ Hz, $\sigma_e^2/\sigma_y^2 = 0.1$, $p, f = 30$, $a = 30$, $N = 5 \cdot 10^4$.

Mode	$\mu_f \pm \sigma_f$ [Hz]	ϵ_f [%]	$\mu_\zeta \pm \sigma_\zeta$ [%]	ϵ_ζ [%]	poles
1	0.666 ± 0.002	0.03	1.838 ± 0.688	583.85	400
2	1.491 ± 0.002	0.89	0.670 ± 0.144	36.32	400
3	-	-	-	-	-
4	2.672 ± 0.006	1.67	1.510 ± 0.178	79.61	400
5	3.278 ± 0.006	4.33	1.647 ± 0.203	64.71	400
6	4.223 ± 0.012	5.68	2.418 ± 0.265	91.09	400
7	4.969 ± 0.011	8.02	2.680 ± 0.240	84.36	400
8	5.384 ± 0.016	9.10	2.460 ± 0.236	57.80	400
9	7.049 ± 0.091	11.70	7.470 ± 1.0881	275.58	271

4-6   Conclusion

In this chapter the continuous-time PBSID_o algorithm was presented. This was done by first introducing the continuous-time framework upon which the method is based. Next, it was explained how the continuous-time state-space model could be transformed to a discrete-time equivalent system using Laguerre projections. Once the discrete-time equivalent system was obtained, the PBSID method could be implemented. However, the implementation of the Laguerre projections was not straightforward. The largest issue that was encountered was the computation of the Laguerre projections for non-uniformly sampled data, which was solved by developing a varying sampling time simulation algorithm.

The PBSID_o algorithm as presented in this chapter was implemented in MATLAB as an extension of the existing PBSID-toolbox. In order to test the performance of the identification method, it was applied to the same simulation example as in Chapter 3. It was observed that the accuracy of the damping estimates was on par with the estimates obtained from the resampled data. However, the estimates of both frequency and damping will get biased when the sampling frequency is taken too low. This effect has also been described in literature and is the result of the discretization of the Laguerre filters.

Part II

Application to Offshore Wind Turbines

Identification of a Wind Turbine Simulation Model

In Chapters 3 and 4 the discrete-time and continuous-time variants of the Predictor-Based Subspace IDentification (PBSID) algorithm were presented. Furthermore, the performance of both algorithms was evaluated by applying it to a simulation example. It was observed that, depending on the conditions of the simulation data, both algorithms were able to obtain reasonable estimates of the eigenfrequencies and damping of the simulation example. In order to find out if the identification algorithms are able to accurately estimate the eigenfrequencies and damping of an Offshore Wind Turbine (OWT), both methods will be applied to wind turbine simulation data in this chapter.

In Section 5-1 the OWT simulation model is presented along with the simulation data which is used for the identification. The setup of the identification algorithm and choice of the identification parameters is subsequently highlighted in Section 5-2. Next, both PBSID algorithms are applied to different sets of simulation data in Section 5-3. In particular, the goal is to estimate the first two tower modes of the OWT, as these have the most influence on the fatigue damage. Finally, in Section 5-4 the results of the different identification methods are compared to each other.

5-1 BHawC Simulation Data

The wind turbine simulation data that will be used in this chapter is generated by the BONUS Horizontal axis wind turbine Code (BHawC). This software package consists of aeroelastic code incorporating a fully non-linear Finite Element Method (FEM) model of a wind turbine, making it possible to simulate the dynamics of an OWT subjected to specific wind, wave and soil conditions.

The turbine simulations are obtained by supplying BHawC with input data. This input data consists of the desired turbine design, the foundation, wave and wind forces acting on the

structure and a specific load case. The load case can, for instance, refer to the production state of the turbine, extreme events or yaw misalignment between the wind and turbine.

The simulations that are performed for the identification in this chapter use the model of a 6-MW wind turbine on a monopile foundation. The load case is set to an idling turbine with the blades pitched out to 88 degrees. The wind speed in the simulations ranges from $U = 1 - 32 \; m/s$, using different turbulence intensities and multiple directions.

The measurement data that will be used for identification consists of two acceleration signals taken from a bidirectional accelerometer. This accelerometer is mounted inside the nacelle of the turbine and measures the accelerations in accordance with the yaw direction of the turbine. Therefore, the x and y directions of the accelerations always refer to the Side-Side (SS) and Fore-Aft (FA) directions visualized in Figure 5-1.
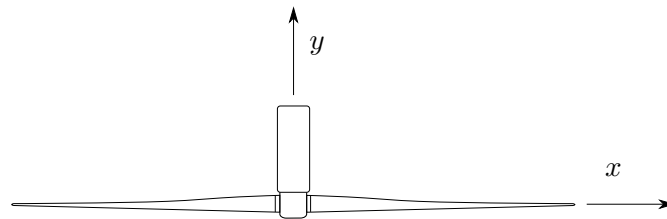
Figure 5-1: Coordinate system for Offshore Wind Turbine acceleration data (top view).

In order to examine the effects of the natural conditions on the damping of the turbine four different load cases are simulated. These load cases are visualized in Figure 5-2, where it can be seen that each load case refers to a specific wind or wave misalignment. Only the identification results of the first load case will be presented in this chapter. The results of the remaining three load cases can be found in Appendix B.
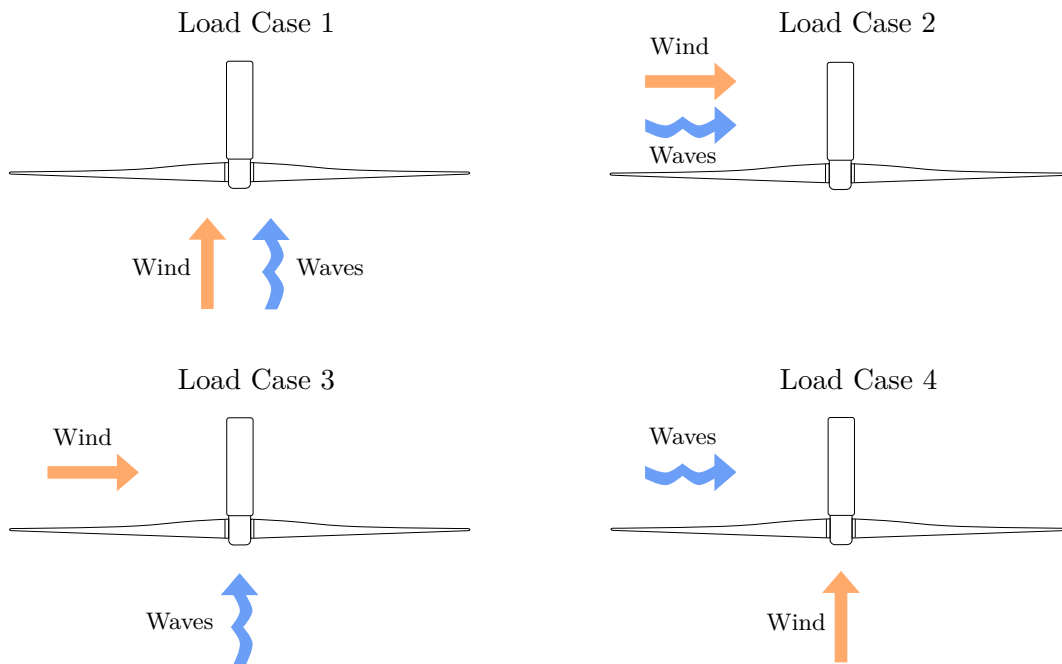
Figure 5-2: The four load cases as simulated in BHawC.

An estimate of the damping of the first FA and SS modes can also be extracted from BHawC by applying an exponential decay fit to the turbine's response resulting from a so called pull-out test. In this case, the top of the turbine receives an initial displacement. The tower top movement as a result of this displacement is subsequently damped out over time. The logarithmic decrement belonging to the first FA and SS tower modes can be estimated by curve fitting the exponential decay of the turbine's damped response. The frequencies and damping belonging to these modes are given in Table 5-1.

Table 5-1: Frequency and damping estimates of the first FA and SS modes obtained from a BHawC exponential decay simulation with wind speed $U = 4\ m/s$.

	Frequency [Hz]	Damping δ [%]
Fore-Aft	■	■
Side-Side		

Using the simulation inputs and load cases mentioned earlier, the BHawC model is simulated at a frequency of $f_s = 100$ Hz such that multiple data sets with a length of five minutes are obtained. This sampling frequency is chosen in order to emulate the non-uniformly sampled accelerations of the real OWT, which have a minimum sampling period of $T_s = 0.01s$. An example of two BHawC simulations at different wind speeds for the first load case is given in Figure 5-3, where the accelerations are plotted against time, as well as against each other. The latter figure shows the cyclic motion of the turbine over time resulting from the excitation of the first two tower modes. It can be observed that the movement of the turbine is dominant in the FA direction and that there is hardly any movement in the SS direction at low wind speeds.
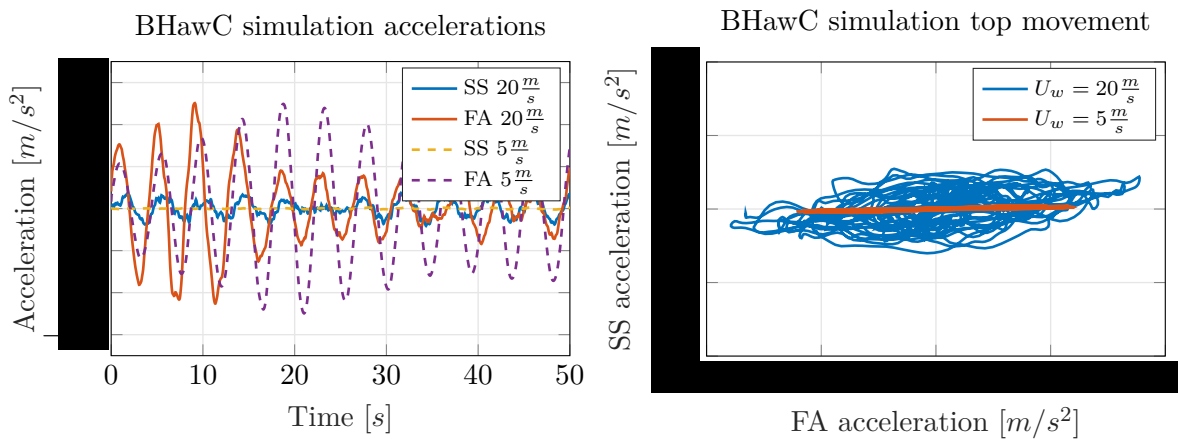
Figure 5-3: Accelerations of the wind turbine's nacelle from BHawC simulations at different wind speeds.

Now that a large amount of simulations is available for identification, the PBSID$_{opt}$ algorithm can be applied. However, some pre-processing of the data is required along with the selection of the identification parameters. This will be treated in the next section.

5-2   BHawC Identification Setup

Before the the discrete and continuous-time identification procedures visualized in Figures 3-1 and 4-1 can be applied to the simulation data, several pre-processing steps need to be applied to the raw acceleration data. Furthermore, it is necessary to select the input parameters for both algorithms. These parameters consist of the past and future window length and the system order. In the case of continuous-time PBSID, the Laguerre filter pole also has to be selected. In this section the pre-processing steps are explained and the choice of identification parameters is justified.

With the simulation examples from Chapters 3 and 4 it was possible to automatically cluster the identification results using Equation (3-25). However, first FA and SS frequencies of the OWT under consideration are in close proximity to each other. This makes it impossible to cluster these modes based on frequency data. As a result, only the Modal Assurance Criterion (MAC) is used to cluster the first two modes. It can be observed in Figure 5-3 that the accelerations in the Side-Side direction of the turbine are a lot smaller than in the Fore-Aft direction. It was found that, using the unprocessed acceleration data, the estimated mode shapes could not be discerned from each other. Therefore, it is impossible to cluster the estimated poles into two groups. This problem can be solved by rescaling the accelerations prior to application of the PBSID$_{opt}$ algorithm, such that both signals have unit variance.

In order to reproduce the conditions of the real turbine measurement data as well as possible, signal noise is added to the BHawC simulation data to mimic sensor noise. From OWT sensor specifications it was found that the amount of sensor noise results in a signal-to-noise ratio of approximately $\sigma_e^2/\sigma_y^2 = 0.1$. Following the addition of the noise, a second order low-pass Butterworth filter is applied to the simulation data in order to eliminate any noise in the higher frequency region.

Looking back at the 9-Degree of Freedom (DoF) model from Chapters 3 and 4, the selection of the model order n was trivial since the model was known. However, for the BHawC model, as well as the real turbine, the model order is unknown beforehand. As mentioned in Chapter 3, the order of a system can be estimated by examining a singular value plot. Unfortunately this does not provide a clear answer, as can be observed in Figure 5-4. Additional insight into the model order can be provided by creating a so called stability plot.
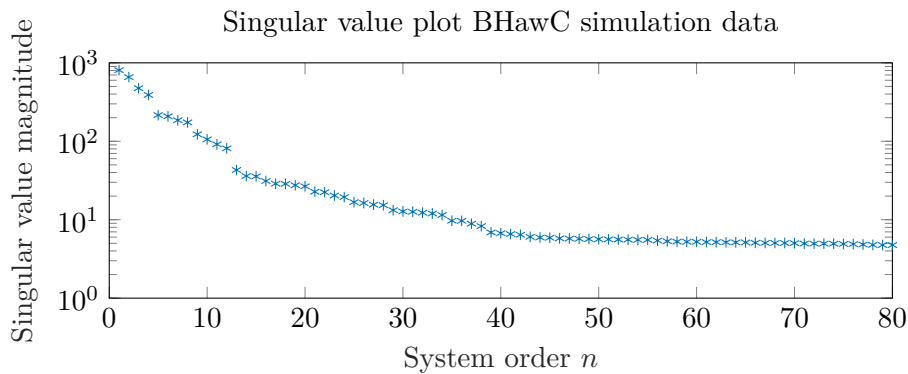

Figure 5-4: Singular value plot created from 6 combined BHawC simulation datasets, $f_s = 25$ Hz, $\sigma_e^2/\sigma_y^2 = 0.1$, $p, f = 250$.

A stability plot shows the eigenfrequencies and damping of the estimated system over a range of system orders. This is useful when identifying the physical poles of a system and casting aside the poles that are a result of noise. The idea behind this is that physical poles will remain at the same location over the different system orders and will therefore have stable frequency and damping values. Creating a stability plot makes it possible to check whether the estimated frequencies coincide with the analytical frequencies, and also gives a range of possible system orders.

A stability plot created from BHawC simulations is given in Figure 5-5, showing that several stable modes have been identified. By considering only the poles around a frequency of $f = 0.2$ Hz, two physical modes can be observed at approximately the same location as the frequencies in Table 5-1. Furthermore, it is seen that these modes are similar for n ranging between 20 and 80. Several system orders within this range were used for the identification of the damping. Selecting a model order of $n = 40$ was found to give the most stable results. This model order will therefore be used in all the following identification runs.
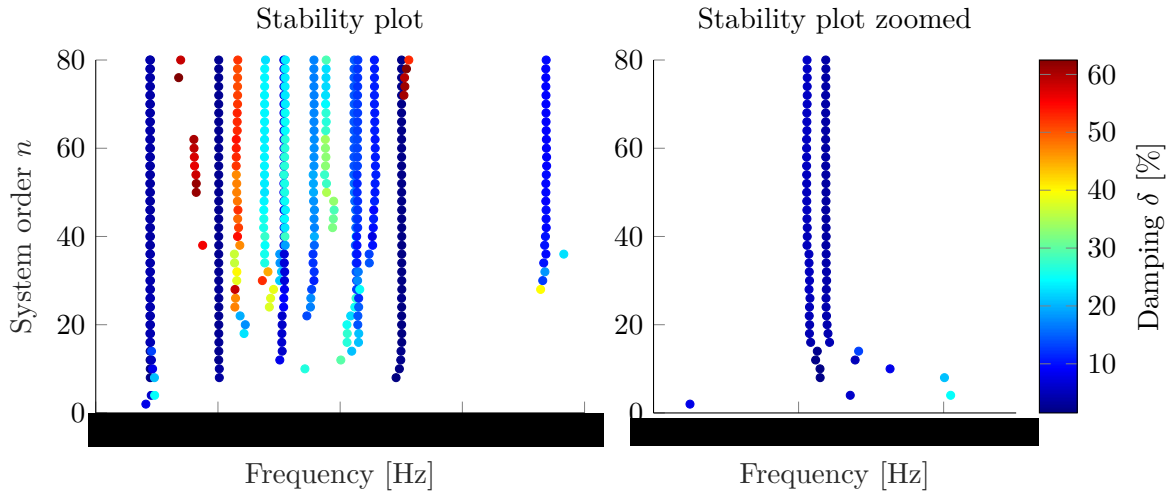
Figure 5-5: Stability plot created from 6 BHawC simulation datasets, $p, f = 250$.

For the identification of the simulation data, only the poles within the frequency band of interest are kept after each identification. Furthermore, identified poles with negative damping ratios or damping ratios greater than $\zeta = 0.1$ are discarded. Ideally, each identification of a simulation dataset will then result in the estimation of two modes, a Fore-Aft and Side-Side mode. Unfortunately, it was observed that the hierarchical clustering method introduced in Section 3-2-5 did not always have a high success rate. In order to cluster the poles with a higher success rate, the modes are separated after each identification by computing the MAC values between the estimated modes and the analytical modes. Using this approach it was found that two clusters of approximately the same size are obtained.

The next step is to select the past and future window sizes required for the PBSID algorithm. This is done by trying to fit the damping estimates from the PBSID algorithm to the damping values given in Table 5-1 that were found with the pull-out test. The results of this fit will be presented in the next section, along with the identification results for different wind speeds.

5-3   Identification Results from BHawC Simulations

In this section the results of the various identification procedures will be presented. For every wind speed there are 72 different simulations available for identification. In order to have a larger group for the identification procedure to draw from, the simulations are grouped into segments of two consecutive wind speeds, resulting in 144 simulation datasets for each identification cycle. Here it is assumed that the change in aerodynamic damping will not be significant when the wind speed increases with 1 m/s.

As mentioned in Section 2-1, there are two types of measurement which can be used for the identification of an OWT. The first type of data consists of measurements which are uniformly sampled at $f_s = 25$ Hz. With these datasets it is possible to directly apply the PBSID$_{opt}$ algorithm in order to estimate the damping. The second type of data consists of measurements that are non-uniformly sampled. For this kind of data there are two options for estimating the damping. The first option is to resample the measurements to a uniformly sampled dataset and subsequently apply the PBSID$_{opt}$ algorithm. The second option is to directly apply the continuous-time PBSID$_o$ algorithm on the non-uniformly sampled data. The goal of this section is to find out which of these three options provides the best results.

In order to find out which identification approach provides the best results, the BHawC simulations are adjusted such that they emulate the turbine measurement data as best as possible. First, the BHawC simulation data is downsampled to $f_s = 25$ Hz to obtain a uniformly sampled dataset. Second, samples are randomly removed from the BHawC simulation data sampled at $f_s = 100$ Hz, such that a non-uniformly sampled dataset is obtained which has an average sampling frequency of $f_s = 25$ Hz. With these two different types of datasets the following three identification procedures can be applied.

1. Identification of the damping by directly applying the discrete-time PBSID$_{opt}$ algorithm on the uniformly sampled datasets.

2. Resampling the non-uniformly sampled datasets to obtain datasets that are uniformly sampled at $f_s = 25$ Hz. Subsequently, the discrete-time PBSID$_{opt}$ algorithm is applied to these datasets.

3. Identification of the damping by directly applying the continuous-time PBSID$_o$ algorithm to the non-uniformly sampled datasets.

The three identification procedures mentioned above each consist of multiple estimations of the system's structural parameters. For a single identification, multiple simulations are randomly selected from the group of available simulations. This process is then repeated until 100 identifications have been performed. This allows for the gathering of statistical information on the identification results. In this case, each identification uses six different simulations, which comes down to a total data length of approximately $N = 45000$ samples. The results for each identification procedure are presented in the following sections.

5-3-1 PBSID$_{opt}$ on BHawC Simulation Data

The discrete-time PBSID$_{opt}$ algorithm is first applied to simulation data which has been uniformly sampled at $f_s = 25$ Hz. In order to find the past and future windows that provide good results, a range of values for p and f were used. The best fit for the PBSID$_{opt}$ algorithm was obtained using $p = f = 125$, of which the results are presented in Figure 5-6. The figure clearly shows that two different modes have been identified at frequencies that coincide with the pull-out test in BHawC. Furthermore, according to the box-plot on the right the damping estimate of the FA mode has been accurately estimated. In case of the SS mode it seems that damping obtained with the PBSID$_{opt}$ algorithm has been slightly underestimated compared to the pull-out test. A possible explanation for this is that the excitation of the wind turbine in the SS direction is almost nonexistent.
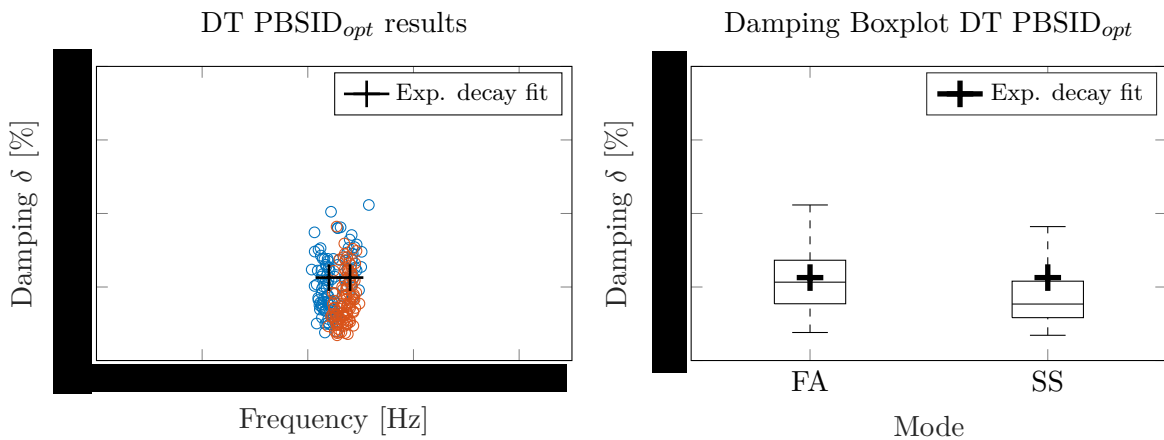
Figure 5-6: Identification results of the first FA and SS modes using the discrete-time PBSID$_{opt}$ algorithm on BHawC simulation data with $U_w = 3-4\ m/s$: 6 data batches for each identification, $f_s = 25$ Hz, $\sigma_e^2/\sigma_y^2 = 0.1$, $p, f = 125$.

The next step is to apply the identification algorithm to the remaining simulation data at different wind speeds. This is done using the same values for p and f for all wind speeds. The identification results for all the wind speed segments are presented in Table 5-2 and Figure 5-7. The table provides statistical information on the results consisting of the mean and standard deviation of the estimated frequency and damping, as well as the success rate of the identification procedure. The figure shows the box plots of the estimated frequencies and damping over all wind speeds.

It has to be noted that the tuning of the past and future windows was done based on acceleration data at wind speeds of $U_w = 3 - 4\ m/s$. However, these values for p and f do not necessarily result in accurate damping estimates using simulation data at different wind speeds. During tuning it was found that the estimated damping is very sensitive to changes in the past and future window sizes.

Looking at the results of the identification procedure, it can be observed that the estimates of the eigenfrequencies are very stable over the entire range of wind speeds and that they agree with the estimates from the pull-out test. At very high wind speeds however, a strange phenomenon is occurring where the frequencies of the FA and SS modes switch location.

Physically speaking this does not make sense, as the OWT has lower inertia in the SS direction due to the free movement of the rotor. As a result the frequency belonging to this mode should be lower than that of the FA mode. This is also thought to be the result of using past and future windows that were not tuned for high wind speeds.

The damping estimates that were obtained show an upward trend for increasing wind speeds in both principal directions. A small increase in damping could be expected beforehand, as the damping resulting from drag is a function of velocity. The largest increase in damping is seen in the SS direction. This could be explained by the pitch of the blades, which causes almost the entire area of the blades to be moving in this direction. This results in a large amount of air being displaced, which in turn leads to increased aerodynamic damping [46].

Table 5-2: Identification results of the first FA and SS modes obtained from BHawC simulation data: 6 databatches for each identification, $f_s = 25$ Hz, $\sigma_e^2/\sigma_y^2 = 0.1$ and $p, f = 125$.

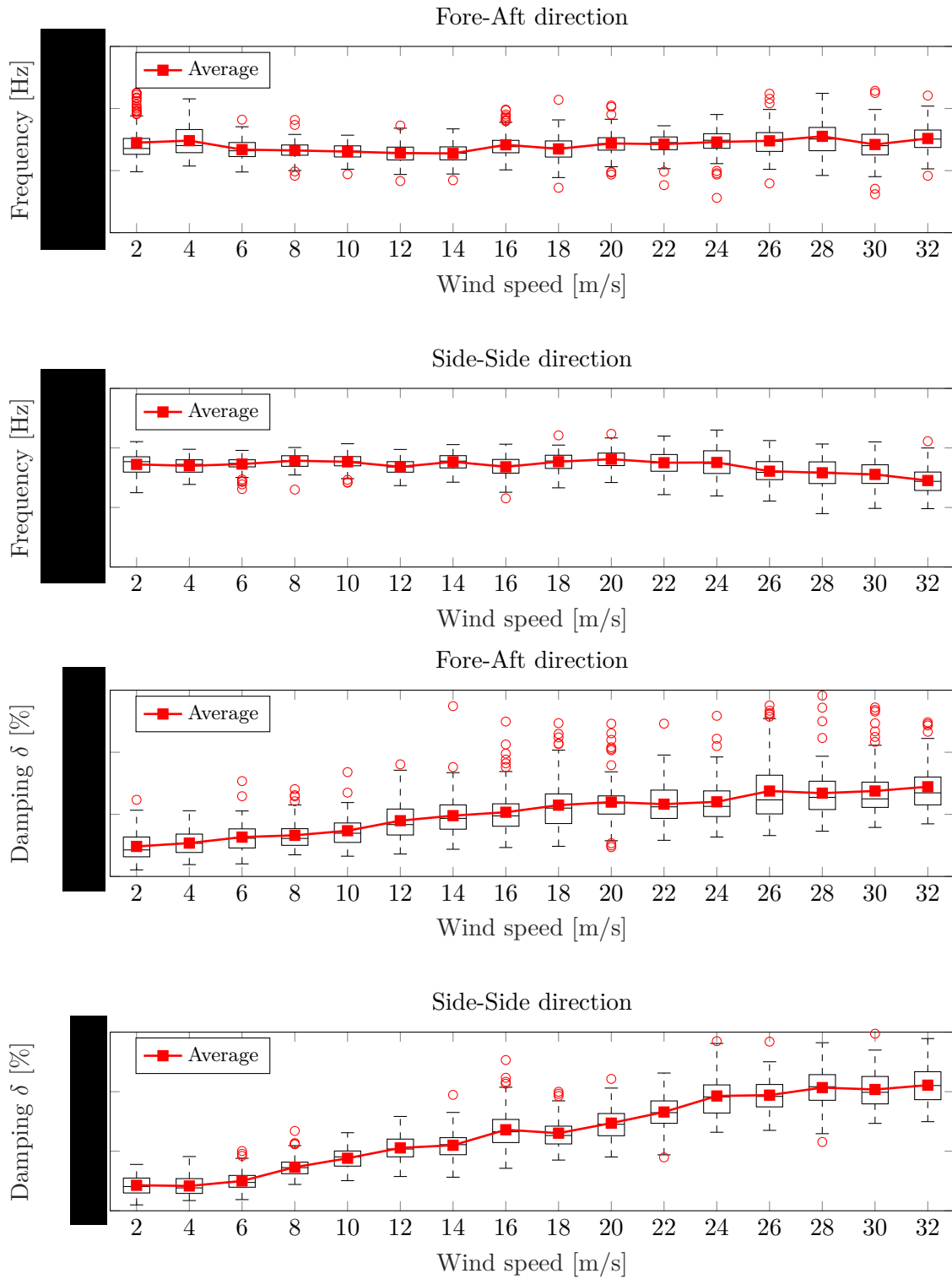| U_{wind} [m/s]	FA $\mu_f \pm \sigma_f$ [Hz]	$\mu_\delta \pm \sigma_\delta$ [%]	Success [%]	SS $\mu_f \pm \sigma_f$ [Hz]	$\mu_\delta \pm \sigma_\delta$ [%]	Success [%]
1-2			100			100
3-4			100			100
5-6			100			100
7-8			100			100
9-10			100			100
11-12			100			100
13-14			100			100
15-16			100			100
17-18			100			100
19-20			100			100
21-22			100			100
23-24			100			100
25-26			99			99
27-28			100			100
29-30			100			100
31-32			100			100

Figure 5-7: Estimated frequency and damping of the first FA and SS modes over a range of wind speeds obtained from BHawC simulation data using the discrete-time PBSID$_{opt}$ algorithm: 6 data batches for each identification, $f_s = 25$ Hz, $\sigma_e^2/\sigma_y^2 = 0.1$ and $p, f = 125$.

5-3-2   PBSID$_{opt}$ on Resampled BHawC Simulation Data

For the next identification procedure, non-uniformly sampled simulation data is resampled at a constant frequency of $f_{s,res} = 25$ Hz and subsequently supplied to the discrete-time PBSID$_{opt}$ algorithm. The non-uniformly sampled data was infected with signal noise beforehand, and should therefore be filtered after resampling. Concerning the choice of resampling method, some conclusions can be drawn by looking at Figure 5-8, which shows the performance of three different resampling methods expressed by the Variance-Accounted-For (VAF). It can be seen that both the *linear* and *pchip* methods show similar results with high VAF values. For this identification procedure the linear resampling method was selected.
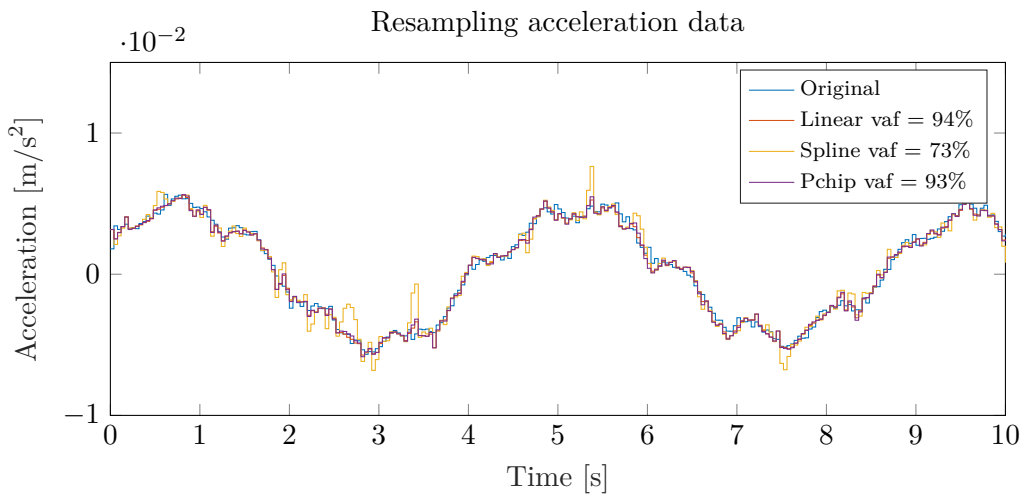
Figure 5-8: Comparing the accuracy of resampling methods in terms of Variance-Accounted-For.

The same values of p and f as in the previous identification procedure were initially used for the identification of the resampled data. However, the results that were obtained using these values were significantly worse than those obtained with the original simulation data. Therefore, the past and future windows were tuned once more for this identification procedure. The best fit in terms of damping estimates was obtained using $p = f = 200$, of which the results can be observed in Figure 5-9. However, even the best fit results in an overestimation of the damping in the FA mode and an underestimation in the SS direction. Hence, it can be concluded that using data which has been resampled from non-uniformly sampled data has a negative effect on the accuracy of the estimated damping for an OWT simulation model.

The identification procedure was subsequently repeated for simulation data over the entire range of wind speeds. The identification results are presented in Table 5-3 and Figure 5-10. From these results it can be concluded that resampling has little effect on the estimated eigenfrequencies. The frequency of the FA mode remains constant for all wind speeds and matches the estimated frequency from the exponential decay fit. The frequencies of the SS mode show a small increase for higher wind speeds and more importantly, they do not drop below the frequencies of the FA mode.
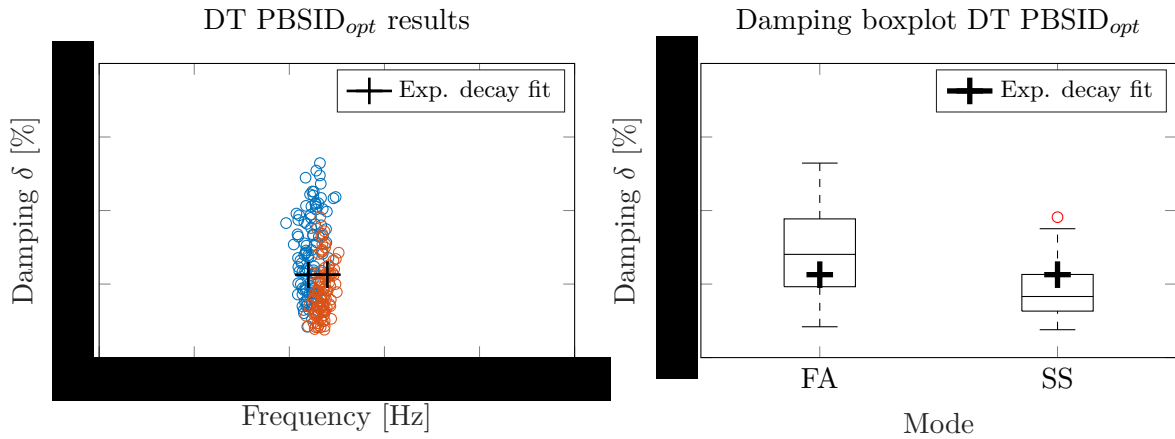
Figure 5-9: Identification results of the first FA and SS modes using the discrete-time PBSID$_{opt}$ algorithm on resampled BHawC simulation data with $U_w = 3 - 4\ m/s$: 6 data batches for each identification, $f_{s,res} = 25$ Hz, $\sigma_e^2/\sigma_y^2 = 0.1$ and $p, f = 200$.

Looking at the estimated damping in the SS direction, a similar upward trend is observed as in the case with the original simulation data. The damping estimates found with both types of simulation data are almost the same for this mode, except for the very high wind speed region, where the damping is lower for resampled simulation data. In the FA direction, a big difference is observed compared to the results of the previous section. Although the estimated damping is too high for low wind speeds, it remains relatively constant over the entire range of wind speeds. Furthermore, the variance of the damping estimates is also smaller than before.

Table 5-3: Identification results of the first FA and SS modes obtained from resampled BHawC simulation data: 6 databatches for each identification, $f_{s,res} = 25$ Hz, $\sigma_e^2/\sigma_y^2 = 0.1$ and $p, f = 200$.

U_{wind} [m/s]	FA $\mu_f \pm \sigma_f$ [Hz]	$\mu_\delta \pm \sigma_\delta$ [%]	Success [%]	SS $\mu_f \pm \sigma_f$ [Hz]	$\mu_\delta \pm \sigma_\delta$ [%]	Success [%]
1-2			100			100
3-4			100			100
5-6			100			100
7-8			100			100
9-10			100			100
11-12			100			100
13-14			100			100
15-16			100			100
17-18			100			100
19-20			100			100
21-22			100			100
23-24			100			100
25-26			100			100
27-28			100			100
29-30			100			100
31-32			100			100

Figure 5-10: Estimated frequency and damping of the first FA and SS modes over a range of wind speeds obtained from resampled BHawC simulation data using the discrete-time PBSID$_{opt}$ algorithm: 6 data batches for each identification, $f_{s,res} = 25$ Hz, $\sigma_e^2/\sigma_y^2 = 0.1$ and $p, f = 200$.

5-3-3   PBSID$_o$ on Non-Uniformly Sampled BHawC Simulation Data

The final identification procedure consists of applying the continuous-time PBSID$_o$ algorithm to non-uniformly sampled simulation data. Since the definitions of the past and future windows differ for the discrete-time and continuous-time PBSID algorithms, tuning of these parameters has to be done once more for this identification procedure. Furthermore, a suitable value for the Laguerre filter pole has to be selected.

In contrast to identification procedures using the discrete-time PBSID$_{opt}$ algorithm, the non-uniformly sampled simulation data is not pre-filtered using a separate low-pass filter. This is because the Laguerre filters used for the projections of the data have their own low-pass filtering properties. In this case the best fit for the damping was obtained using parameters $p, f = 35$ and $a = 5$. The identification results using these parameters are presented in Figure 5-11. The damping estimates obtained with the continuous-time PBSID$_o$ algorithm are seen to be accurate for the FA mode. However, the damping in the SS direction seems to be greatly underestimated.

Besides the fact that the fastlog measurement data which will be used in Chapter 6 is non-uniformly sampled, the sampling instants of the two acceleration channels differ as well. Consequently, the Laguerre projections of the measurement data cannot be directly supplied to the continuous-time PBSID$_o$ algorithm. In order to solve this problem, the updating property of the RQ-factorization presented in Chapter 3 is exploited. This is done by splitting a single acceleration dataset $y = [y_{ss} \quad y_{fa}]^T$ into two parts such that

$$y_1 = \begin{bmatrix} y_{ss}(t_1) & y_{ss}(t_2) & \cdots & y_{ss}(t_N) \\ 0 & 0 & \cdots & 0 \end{bmatrix}, \quad y_2 = \begin{bmatrix} 0 & 0 & \cdots & 0 \\ y_{fa}(t_1) & y_{fa}(t_2) & \cdots & y_{fa}(t_N) \end{bmatrix}. \quad (5\text{-}1)$$

In this way, the identification is first based on the accelerations in the SS direction, and the system estimate is subsequently updated using the accelerations in the FA direction. However, this solution does result in twice the amount of data that has to be processed by the PBSID$_o$ algorithm. For this continuous-time identification procedure, different samples of the two acceleration signals are randomly removed and the data is split into two batches in order to mimic the properties of the fastlog measurement data.
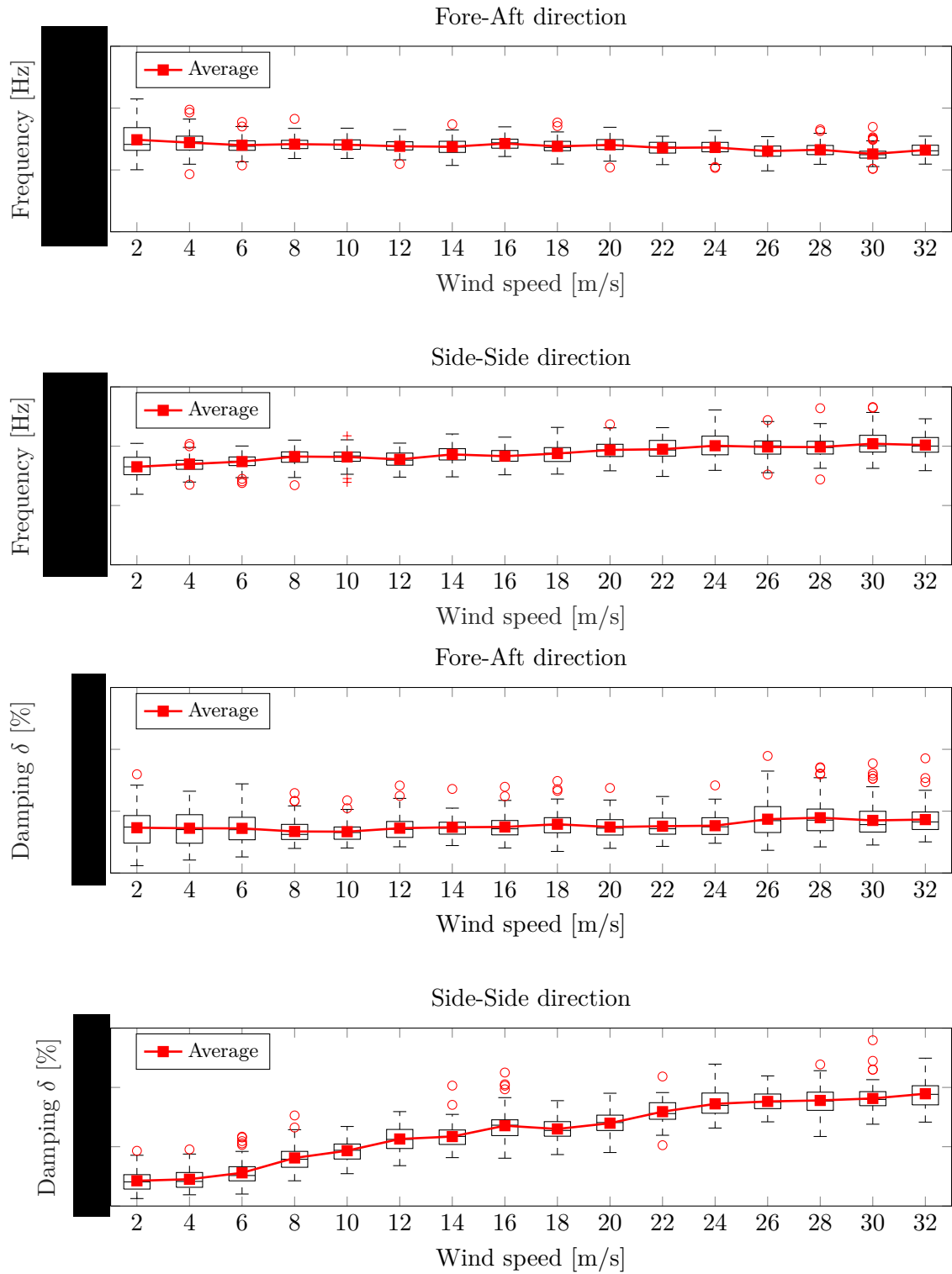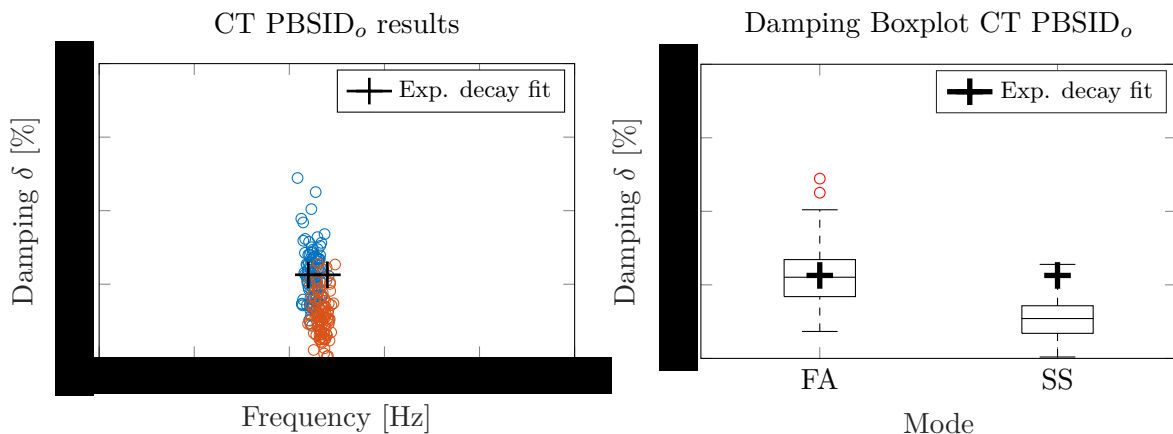

Figure 5-11: Identification results of the first FA and SS modes using the continuous-time PBSID$_o$ algorithm on non-uniformly sampled BHawC simulation data with $U_w = 3 - 4 \ m/s$: 6 data batches for each identification: $f_{s,avg} = 25$ Hz, $\sigma_e^2/\sigma_y^2 = 0.1$, $p, f = 35$ and $a = 5$.

Looking at the results presented in Table 5-4 and Figure 5-12, it can be seen that the identification results of the continuous-time PBSID$_o$ algorithm are very similar to the results obtained using the discrete-time variant. The success rate of this identification procedure is a little lower than that of the previous two. It is observed that the estimated frequencies remain relatively constant over the entire range of wind speeds. Furthermore, the frequencies are more or less the same as the frequencies obtained with the pull-out test.

The damping of the SS mode again shows the upward trend for increasing wind speeds, similar to the previous two identification procedures. Apart from the estimates at wind speeds under $U_w = 4\ m/s$, the damping values for this mode agree with the damping estimates found with the discrete-time PBSID$_{opt}$ algorithm. The damping estimates of the FA only show a small increase in damping for higher wind speeds, similar to the case of resampled simulation data.

Table 5-4: Identification results of the first FA and SS modes obtained from non-uniformly sampled BHawC simulation data: 6 databatches for each identification, $f_{s,avg} = 25$ Hz, $\sigma_e^2/\sigma_y^2 = 0.1$, $p, f = 35$ and $a = 5$.

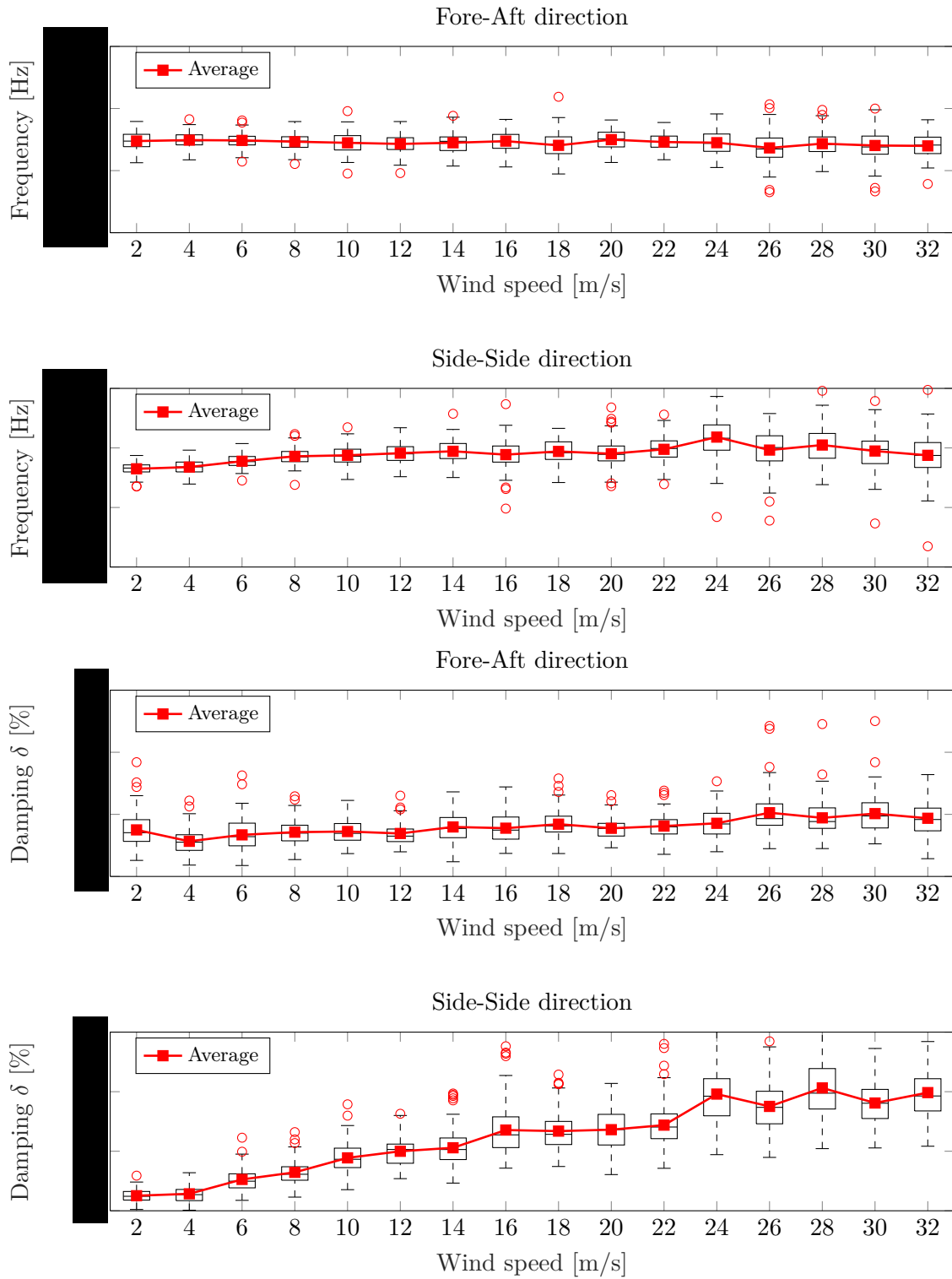|	FA			SS		
U_{wind} [m/s]	$\mu_f \pm \sigma_f$ [Hz]	$\mu_\delta \pm \sigma_\delta$ [%]	Success [%]	$\mu_f \pm \sigma_f$ [Hz]	$\mu_\delta \pm \sigma_\delta$ [%]	Success [%]
1-2			100			98
3-4			99			98
5-6			97			97
7-8			97			97
9-10			99			99
11-12			98			98
13-14			100			100
15-16			99			99
17-18			93			93
19-20			99			99
21-22			98			98
23-24			97			96
25-26			100			100
27-28			96			95
29-30			99			99
31-32			95			95

Figure 5-12: Estimated frequency and damping of the first FA and SS modes over a range of wind speeds obtained from BHawC simulation data using the continuous-time PBSID$_o$ algorithm: 6 data batches for each identification, $f_{s,avg} = 25$ Hz, $\sigma_e^2/\sigma_y^2 = 0.1$, $p, f = 35$ and $a = 5$.

Three different identification procedures have now been applied to wind turbine simulation data in this section. It was observed that each identification procedure was able to obtain accurate estimates of the wind turbine model its eigenfrequencies. The estimated damping values showed a larger variation between the three identification procedures for certain wind speeds. The average estimated damping values have been plotted against each other in Figure 5-13 to allow for better comparison.

The damping values in the FA direction provided by the second and third identification procedures are shown to be very similar and relatively stable over the entire range of wind speeds. However, the damping estimated using resampled data in the low wind speed region did not match the estimate of the exponential decay fit. This is thought to be the result of both the resampling process and the level of accelerations in the SS direction, which are almost nonexistent. Despite the low level of accelerations at low wind speeds, the first identification procedure was able to obtain a similar damping estimate as in the case of the pull-out test. However, the damping estimated with this procedure for higher wind speeds did not match the behavior of the other two identification procedures. This is likely to be the result of the tuning parameter p and f, which were selected for identification at lower wind speeds and may therefore not be optimal for higher wind speeds.

The damping estimates in the SS direction show similar behavior over the entire range of wind speeds for all three identification procedures. As mentioned before, the increased damping at higher wind speeds can be explained by the large amount of air which is being displaced in the SS direction by the pitched out blades.
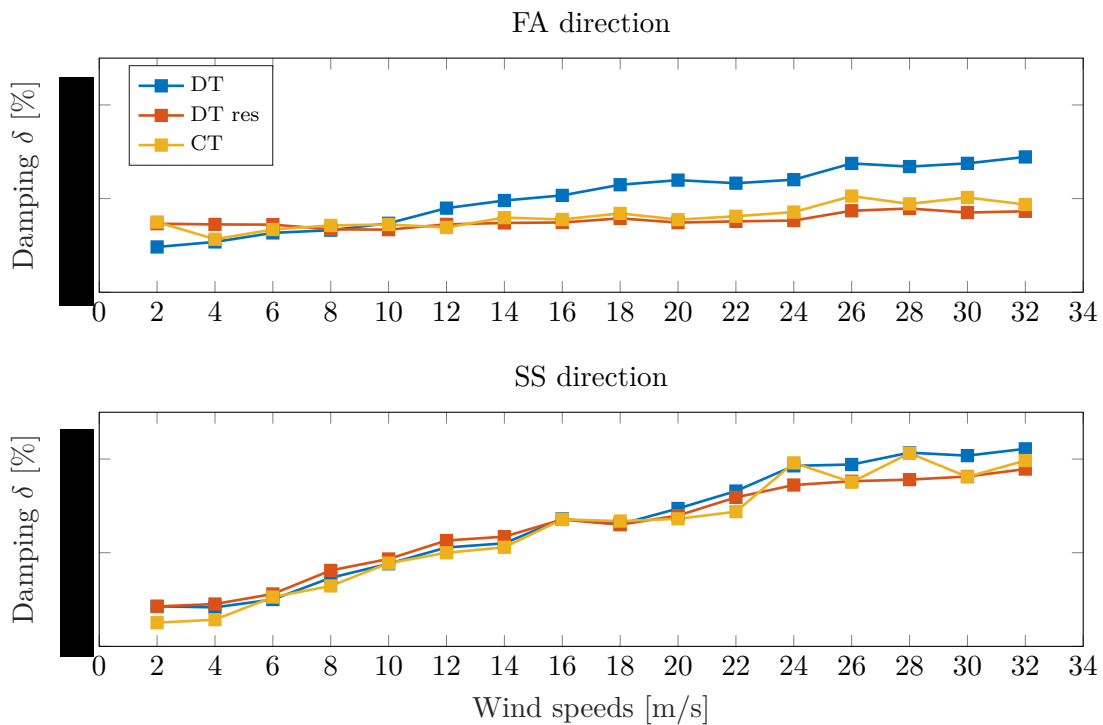
Figure 5-13: Comparison of the estimated damping using the three different identification procedures.

5-4   Conclusion

In this chapter the discrete and continuous-time PBSID algorithms were applied to simulation data generated by an OWT simulation model. The identification was performed by three different procedures. The first procedure used the original BHawC accelerations in combination with the PBSID_{opt} algorithm. The second procedure used resampled simulation data with the PBSID_{opt} algorithm. The final procedure consisted of applying the continuous-time PBSID_o algorithm to non-uniformly sampled data.

It was observed that each identification procedure was able to estimate two clusters representing the FA and SS modes. The frequencies of these clusters agreed with the values that were estimated using a exponential decay fit in BHawC. The damping estimates of the FA mode were different depending on the identification procedure. The first identification procedure showed increased damping for higher wind speeds, while the other two procedures resulted in more stable damping estimates. The different results obtained with the first procedure are thought to be the result of the past and future windows, which were selected for identification at low wind speeds.

All three identification procedures showed that the damping of an idling OWT is dominant in the SS direction. An upward trend was observed in the damping of the SS mode for increasing wind speeds. This behavior can be explained by the fact that the blades are pitched out. Large amounts of air are subsequently displaced in the SS direction, leading to increased aerodynamic damping.

<div style="text-align: right">

Chapter 6

</div>

Identification of an Offshore Wind Turbine

In this chapter the discrete-time and continuous-time PBSID algorithms will be applied to measurement data taken from an idling Offshore Wind Turbine (OWT), in order to obtain damping estimates belonging to the first Fore-Aft (FA) and Side-Side (SS) modes. The identification algorithms will be applied to two types of measurement data, namely Power Load Measurement (PLM) data and fastlog data. The PLM data consists of measurements taken at a constant sampling frequency, while the fastlog data contains non-uniformly sampled measurements.

Three identification procedures were previously applied to wind turbine simulation data that was representable for real measurement data in Chapter 5. It was observed that the two modes could be accurately identified in terms of their frequencies. Damping proved to be harder to estimate, as the different identification procedures did not alway result in the same damping values. Nevertheless, all identification procedures showed an upward trend for damping in the SS direction for increasing wind speeds, whereas the damping in the FA direction only showed a small increase. Hence, the results that were obtained using simulation data are encouraging enough to apply the identification algorithms to turbine measurement data.

The PLM data is first introduced in Section 6-1, after which the discrete-time PBSID$_{opt}$ algorithm is applied to estimate the damping. In Section 6-2, the fastlog measurement data is presented. This data is subsequently used twice to estimate the damping. First, it is resampled and supplied to the discrete-time PBSID$_{opt}$ algorithm. Second, the continuous-time PBSID$_o$ algorithms is directly applied to the *raw* acceleration data. Conclusions on the damping estimates obtained with these two types of measurement data are presented in Section 6-3.

6-1   Identification with PLM Measurement Data

In this section the discrete-time PBSID$_{opt}$ algorithm will be applied to PLM measurement data taken from an idling OWT at both low and high wind speeds. The selection methods and acquired PLM data will be discussed in Section 6-1-1. Using the PBSID$_{opt}$ algorithm on this data, an attempt is made to identify the first FA and SS modes of the turbine and quantify the amount of damping that is present at these frequencies. The results of the identification are presented in Section 6-1-2.

6-1-1   PLM Measurement Data

The properties of the PLM data were already briefly discussed in Section 5-2. The PLM turbine is equipped with a great number of sensors that measure the response of the OWT caused by wind and wave loading. Furthermore, some of the internal states of the turbine are measured as well, such as the generated power and pitch of the blades. All these measurement are taken at a constant sampling frequency of $f_s = 25$ Hz. From all these measurements, only the accelerations of the nacelle in the FA and SS direction are directly used for the identification.

In order to find measurement data that is suitable for identification purposes, it is necessary to look at the operational state of the wind turbine and the pitch position of the blades. The accelerations required for identification are only taken when the turbine is idling and the blades are pitched out. Idling means that no power is generated and the turbine is rotating at less than 0.25 revolutions per minute. This scenario can be encountered in two instances. The first scenario is when there is a long period of below cut-in wind speeds. The second scenario is only rarely encountered and occurs when the wind speeds are above cut-out level.

The PLM data unfortunately does not provide any information about the current operational state of the turbine. In order to find suitable measurements, the fastlog data is analyzed first since this data does contain information about the operational state. Using the fastlog data, multiple moments in time are identified which contain idling data. The next step is to check whether the blades are pitched out sufficiently during these time instants. The minimum pitch level that is allowed is chosen to be at $75°$. This pitch level is lower than seen in the previous chapter, but is necessary in order to obtain a sufficient amount of data. Using this selection procedure, the entire measurement database is searched for suitable acceleration data. After processing all of the available data, the suitable measurements are cut into segments of 10 minutes of idling data. This is done to increase the size of the pool containing the measurements that will be used for identification.

A segment of such a dataset is presented in Figure 6-1, where the accelerations are given over time and the movement of the nacelle is visualized. By comparing these accelerations with those of the BHawC simulation in Figure 5-3, it can be observed that the amplitudes of accelerations at low wind speeds in the SS direction are actually many times larger in reality. This is primarily due the wave misalignment of the OWT, meaning that the movement of the waves is not purely in the SS direction. Furthermore, it should be noted that as a result of idling there is yaw misalignment regarding the wind direction as well. However, it is expected that this has little effect on the damping estimates for low wind speeds, since the excitation of the OWT is wave driven.
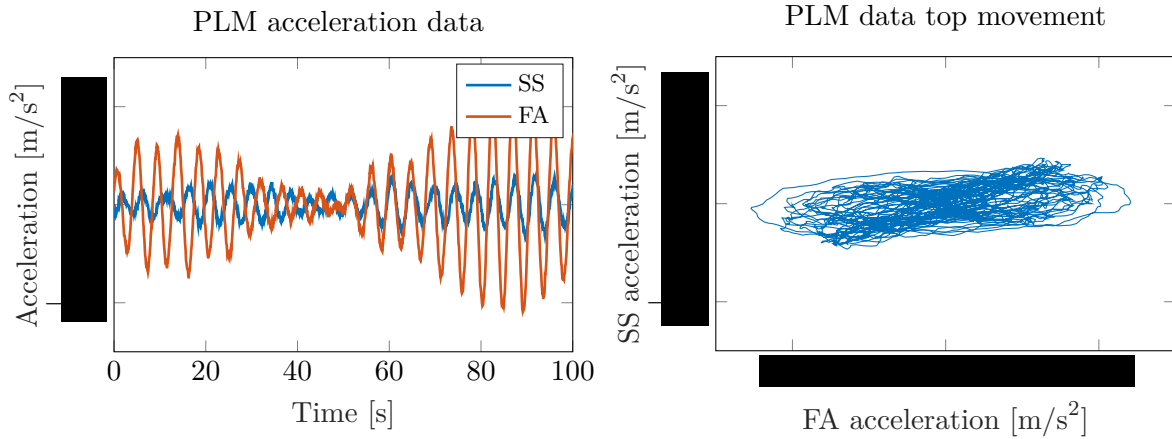
Figure 6-1: Accelerations taken from PLM data at an average wind speed of $U_w = 1.5 \ m/s$. The accelerations are plotted against time (left) and against each other (right).

6-1-2   Identification using PLM Data

The identification procedure from Figure 3-1 can be applied almost directly to the PLM data. First however, the measurement data is pre-filtered with a second order low-pass Butterworth filter, with cut-off frequency $\omega_c = 10 \ rad/s$, in order to remove the influence of noise at higher frequencies. Next, the accelerations are rescaled to obtain data with unit variance. Finally, the accelerations are downsampled to a frequency of $f_s = 15$ Hz. This is done in order to get a better comparison between the different identification procedures, as will become clear in the next section. Once the pre-processing is done, the discrete-time PBSID$_{opt}$ algorithm can be applied to the measurement data. The same identification parameters will be used as in Section 5-3.

The identification results obtained using PLM data at low wind speeds are presented in Table 6-1 and Figure 6-2. It can be observed that two clusters have been identified at nearby frequencies and that these frequencies are higher than estimated using the BHawC simulation data. The estimated damping of the FA mode seems to agree with the estimates of the BHawC data, indicating that the damping is at the structural damping level and hence aerodynamic damping effects are negligible at low wind speeds. The damping in the SS direction on the other hand, is almost twice as large as estimated using the BHawC data. This can partly be explained by the load case that was used for the BHawC simulation data, which as it turned out is not entirely representable for real idling behavior at low wind speeds. Furthermore, it might also be the case that the BHawC model itself is unable to accurately simulate an idling OWT at low wind speeds or that false assumptions were taken regarding the other sources of damping, i.e., structural, soil and hydrodynamic damping.

Table 6-1: Frequency and damping estimates of the first FA and SS modes obtained using the PBSID$_{opt}$ algorithm on PLM data for wind speeds under $U_w = 4 \ m/s$.

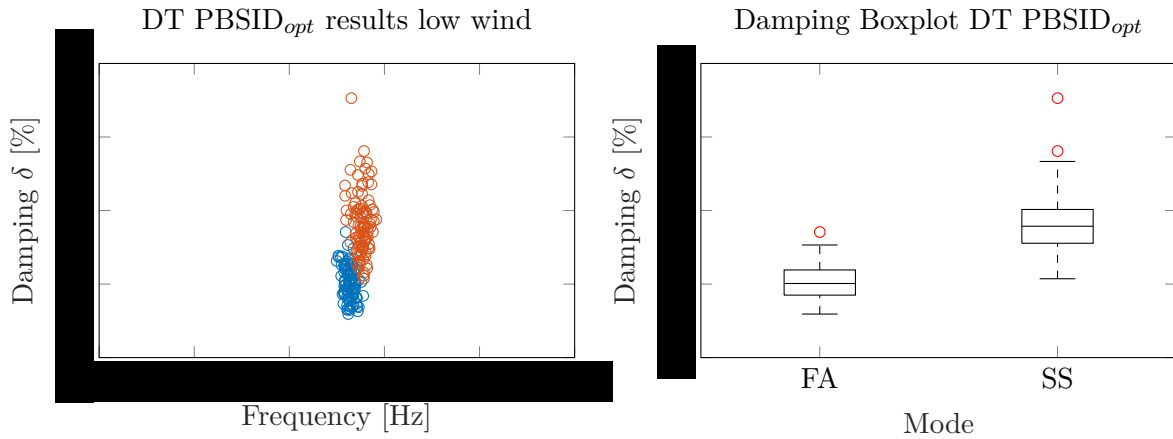|	$\mu_f \pm \sigma_f$ [Hz]	$\mu_\delta \pm \sigma_\delta$ [%]	Success [%]
Fore-Aft			100
Side-Side			100

Figure 6-2: Identification results of the first FA and SS modes using the discrete-time PBSID$_{opt}$ algorithm on PLM data for wind speeds below $U_w = 4\ m/s$; $f_s = 15$ Hz, $p, f = 125$ and $n = 40$.

The identification procedure is applied to high wind speed measurement data as well. The results obtained using this data are presented in Table 6-2 and Figure 6-3. It can be observed that a smaller amount of identification cycles is used. This is because idling due to high wind speeds does not occur often and therefore only a small amount of data is available. The identified damping using high wind speed data shows a better match with the damping estimates from Chapter 5. A small increase in damping is seen in the FA direction and large increase in the SS direction. In the next section fastlog will be used for identification.

Table 6-2: Frequency and damping estimates of the first FA and SS modes obtained using the PBSID$_{opt}$ algorithm on PLM data for average wind speeds of $U_{w,avg} = 21\ m/s$.

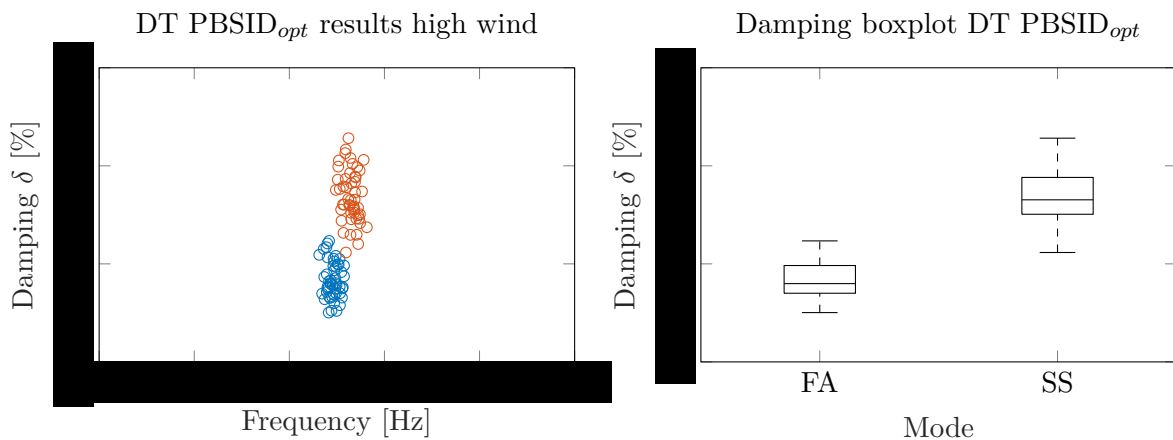|	$\mu_f \pm \sigma_f$ [Hz]	$\mu_\delta \pm \sigma_\delta$ [%]	Success [%]
Fore-Aft			100
Side-Side			100

Figure 6-3: Identification results of the first FA and SS modes using the discrete-time PBSID$_{opt}$ algorithm on PLM data for average wind speeds of $U_{w,avg} = 21$; $f_s = 15$ Hz, $p, f = 125$, $n = 40$.

of the PLM data. The results of this identification procedure are presented in Figure 6-5 and Table 6-3.

The results obtained using the resampled fastlog data are very similar to those found with the PLM data. It can be observed that the estimated frequencies are identical, while the damping values differ only slightly. This small difference in estimated damping could either be the result of the resampling process, or because the datasets used for this identification are not exactly the same as the PLM datasets. However, from these results it can be concluded that estimating the damping using resampled fastlog measurement data provides results that are of similar accuracy as when PLM data is used. A side note with this remark is that only the first FA and SS modes have been identified at this time. If higher frequency modes are to be estimated, resampling can lead to biased damping estimates as was seen in Chapter 3.
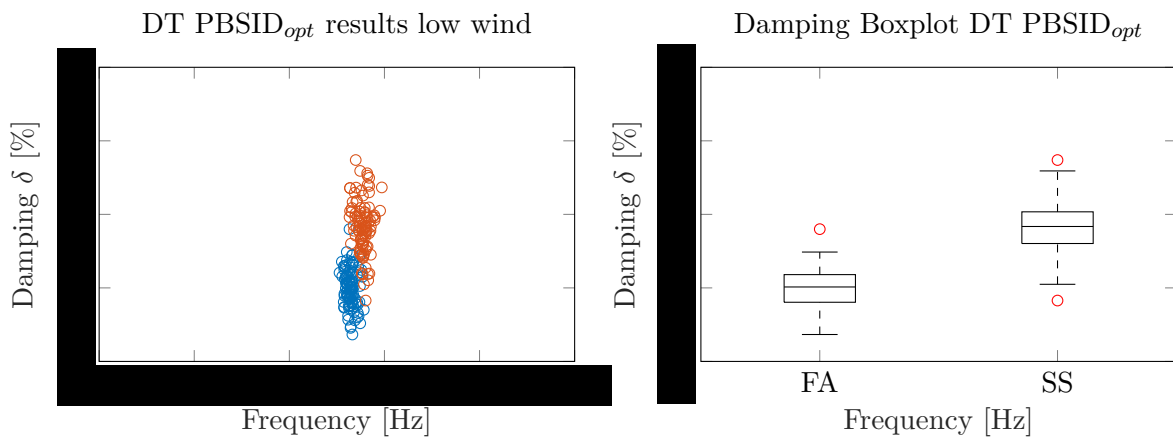

Figure 6-5: Identification results of the first FA and SS modes using the discrete-time PBSID_{opt} algorithm on resampled fastlog measurement data for wind speeds below $U_w = 4\ m/s$; resampled at $f_{s,res} = 15$ Hz, $p, f = 125$ and $n = 40$.

For the second identification procedure, the non-uniformly sampled measurement data is supplied directly to the continuous-time PBSID_o algorithm after rescaling. The same identification parameters are selected as in Section 5-2. The results of the continuous-time identification procedure are presented in Figure 6-6 and Table 6-3.

It can be observed that the continuous-time PBSID_o algorithm is able to identify the first FA and SS modes. Looking at the results it seems the estimated frequencies are slightly higher compared to the values found with discrete-time identification. It is possible that this is the result of discretization errors as was explained in Section 4-4-1. The estimated damping is also similar to the discrete-time case. It can be observed that the FA damping is slightly higher and the SS damping is slightly lower than for the other two identification procedures. Hence, it can be concluded that the damping of the first FA and SS modes can also be estimated using the continuous-time PBSID_o algorithm in combination with fastlog data. However, in this case it is also important to note that this might not be the case when higher frequency modes are to be identified. Judging from the results of the simulation example in Section 4-5, it is expected that a bias will occur in the estimated frequency and damping which will increase for higher frequencies.
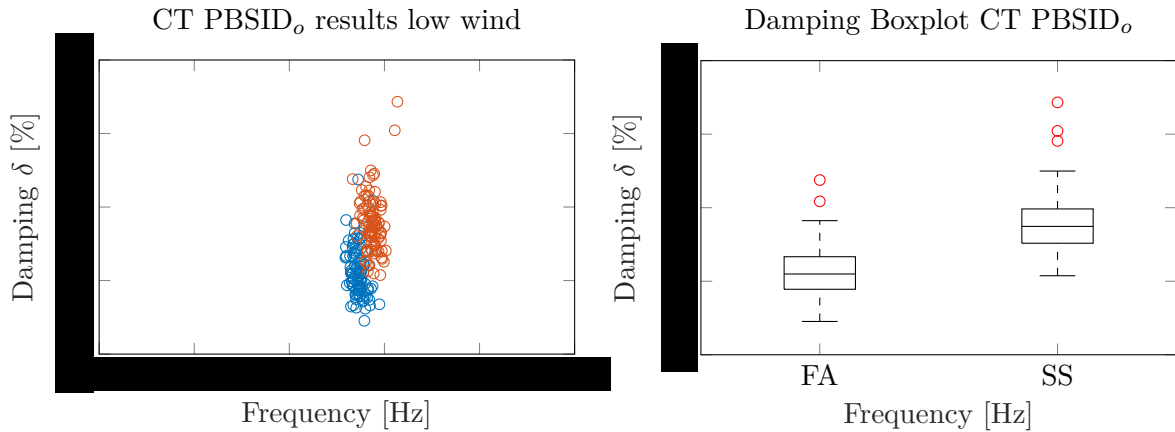
Figure 6-6: Identification results of the first FA and SS modes using the continuous-time PBSID$_o$ algorithm on non-uniformly sampled fastlog data for wind speeds below $U_w = 4\ m/s$; $p, f = 35$, $a = 5$ and $n = 40$.

Table 6-3: Frequency and damping estimates of the first FA and SS modes obtained using the discrete-time PBSID$_{opt}$ and continuous-time PBSID$_o$ algorithms on fastlog measurement data for wind speeds below $U_w = 4\ m/s$.

	DT PBSID$_{opt}$			CT PBSID$_o$		
	$\mu_f \pm \sigma_f$ [Hz]	$\mu_\delta \pm \sigma_\delta$ [%]	Success [%]	$\mu_f \pm \sigma_f$ [Hz]	$\mu_\delta \pm \sigma_\delta$ [%]	Success [%]
Fore-Aft			100			99
Side-Side			100			99

Both identification procedures were applied to fastlog acceleration data at high wind speeds as well. The results of these identifications are presented in Figures 6-7 and 6-8 and Table 6-4. The damping estimates obtained using the resampled fastlog data are similar to those obtained with the PLM and the BHawC simulation data. However, the continuous-time PBSID$_{opt}$ algorithm is not able to give a reliable estimate of the SS damping, as visualized by the large spread in the damping estimates of this mode. A possible explanation for this is that the continuous-time PBSID$_o$ algorithm was not properly tuned for high wind speed data.

Table 6-4: Frequency and damping estimates of the first FA and SS modes obtained using the discrete-time PBSID$_{opt}$ and continuous-time PBSID$_o$ algorithms on fastlog measurement data for average wind speeds of $U_{w,avg} = 21$.

	DT PBSID$_{opt}$			CT PBSID$_o$		
	$\mu_f \pm \sigma_f$ [Hz]	$\mu_\delta \pm \sigma_\delta$ [%]	Success [%]	$\mu_f \pm \sigma_f$ [Hz]	$\mu_\delta \pm \sigma_\delta$ [%]	Success [%]
Fore-Aft			100			94
Side-Side			100			94
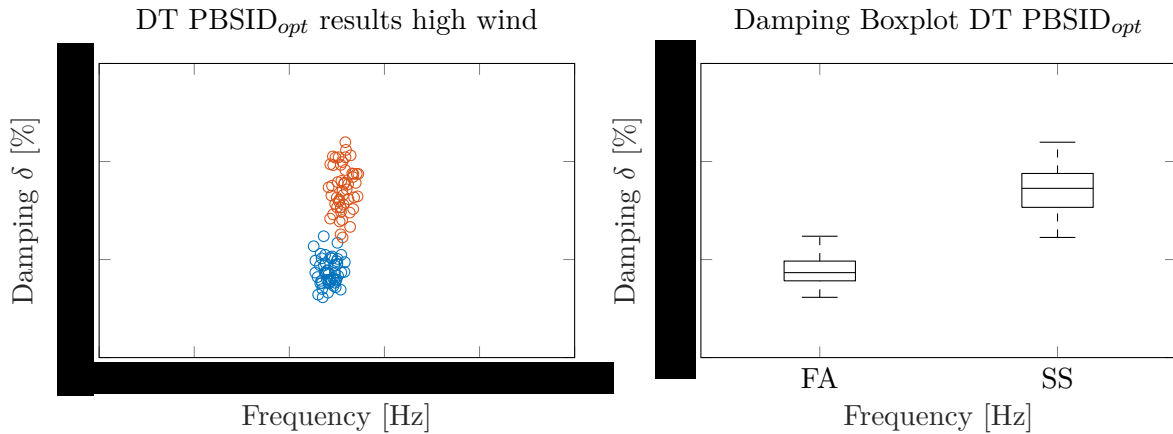
Figure 6-7: Identification results of the first FA and SS modes using the discrete-time PBSID$_{opt}$ algorithm on resampled fastlog measurement data for average wind speeds of $U_{w,avg} = 21$; resampled at $f_{s,res} = 15$ Hz, $p, f = 125$ and $n = 40$.
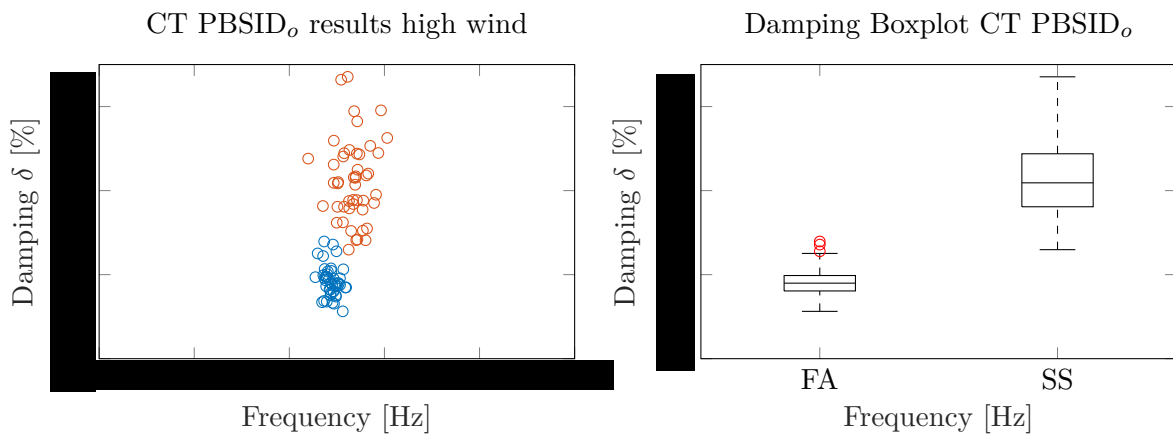
Figure 6-8: Identification results of the first FA and SS modes using the continuous-time PBSID$_o$ algorithm on non-uniformly sampled fastlog measurement data for average wind speeds of $U_{w,avg} = 21$; $p, f = 35$, $a = 5$ and $n = 40$.

6-3   Conclusion

The goal of this chapter was to identify the damping of an OWT using measurement data. The damping of the first FA and SS modes was estimated using two types of data, namely PLM and fastlog data. This measurement data was processed beforehand to only contain accelerations from idling turbines with pitched out blades.

The PBSID$_{opt}$ algorithm was first applied to the uniformly sampled PLM data at low wind speeds. The estimated damping in the FA direction agreed with the values found in Chapter 5. However, the damping in the SS direction was higher than expected. The difference in estimated damping could be explained by the fact that the BHawC load case was not entirely representable for a real idling OWT. Another possible explanation is that the BHawC model

is not entirely accurate or uses false assumptions for the turbine's other damping sources. The results obtained using PLM data for high wind speeds were in better agreement with the BHawC simulation results, showing increased damping in both FA an SS direction.

Next, the fastlog data was used to estimate the damping. The data was first resampled and supplied to the PBSID$_{opt}$ algorithm. For the final identification procedure, the non-uniformly sampled fastlog data was directly supplied to the PBSID$_o$ algorithm. The results obtained with both methods for low wind speeds are very similar to each other, and to the results of the PLM data as well. Hence, it can be concluded that the damping of the first FA and SS modes can indeed be estimated from fastlog data.

Conclusions and Recommendations

This chapter will present the conclusions on the research problems presented in Chapter 1. Furthermore, recommendations for future work or research are provided based on these conclusions.

7-1 Conclusions

In order to reduce the cost of energy for offshore wind energy, the design of an Offshore Wind Turbine (OWT) should be further optimized. An important factor in the design is represented by the damping, which is inversely proportional to the amount of fatigue damage that occurs in an OWT. The largest contribution to the fatigue damage is given when the OWT is idling, since it is assumed that the aerodynamic damping is negligible in this state. Therefore, it is vital to have accurate damping estimates of an idling OWT, especially the damping of the first Fore-Aft (FA) and Side-Side (SS) modes.

For the damping identification of an OWT, a large amount of non-uniformly sampled measurement data is available. The goal of this thesis is formulated by the following research problem:

"Identify the structural parameters of an idling Offshore Wind Turbine using non-uniformly sampled measurement data."

The non-uniformly sampled measurement data cannot be used directly for identification of the damping using conventional Operational Modal Analysis (OMA) methods. There are two possible approaches for the use of this kind of data for identification purposes. Therefore, the problem formulation given above is split into two subproblems. The first approach consists of resampling the non-uniformly sampled data with a constant sampling frequency and subsequently applying OMA techniques. Hence, the first subproblem is given by:

"Examine the effects of resampling non-uniformly sampled measurement data on the estimated structural parameters of an Offshore Wind Turbine."

For the second identification approach, literature offers a solution in the form of continuous-time identification methods. These methods can be applied directly to non-uniformly sampled data. The second subproblem is subsequently given by:

"Investigate continuous-time identification methods and subsequently evaluate the performance when applied to non-uniformly sampled turbine measurement data."

For the identification of the damping parameters, the Predictor-Based Subspace IDentification (PBSID) method was selected. The PBSID$_{opt}$ algorithm is based on a discrete-time state-space representation of a system. However, this method can also be extended to obtain a continuous-time representation of the system. In the first part of this thesis the discrete and continuous-time PBSID algorithms were presented and subsequently applied to a simulation example. The second part consisted of applying both methods to wind turbine simulation and measurement data, respectively. Furthermore, the results obtained using non-uniformly sampled measurement data were compared with the results obtained through measurement data with a constant sampling frequency.

In order to answer the research problems of this thesis, conclusions are presented on the following subjects:

1. Discrete-Time PBSID$_{opt}$ Algorithm

   - The discrete-time PBSID$_{opt}$ algorithm is able to accurately estimate the eigenfrequencies and damping ratios of a 9-Degree of Freedom (DoF) model. By increasing the amount of data, it was seen that the accuracy and precision of the damping estimates increases as well. Furthermore, the sampling frequency of the simulation data can affect the accuracy of the identification results.

   - The effects on the identification results of resampling non-uniformly sampled data were examined using the 9-DoF simulation example. It was observed that resampling of non-uniformly sampled measurement data can have a negative effect on the estimation of the damping.

   - It was observed that batch wise identification was not correctly implemented within the PBSID-toolbox developed at the Delft Center for Systems and Control (DCSC). The toolbox was subsequently extended with this functionality, using the possibility of updating the RQ-factorization in the PBSID$_{opt}$ algorithm. With these modifications the same effect as increasing the length of a measurement is achieved.

2. Continuous-Time PBSID$_o$ Algorithm

   - The continuous-time identification algorithm has been applied to the 9-DoF simulation model and the results were compared to those obtained with the discrete-time identification algorithm. It was observed that the accuracy of the damping estimates was on par with the estimates obtained from the resampled data. However, the estimates of both frequency and damping will get biased when the sampling frequency is taken too low. This effect has also been described in literature and is the result of the discretization of the Laguerre filters.

   - Compared to its discrete-time counterpart, the PBSID$_o$ algorithm requires a lot more computational power. This results in longer computation times and might prove troublesome when large past and future windows are required.

3. Identification of Turbine Simulation Data

- Using the PBSID$_{opt}$ algorithm on uniformly sampled BHawC simulation data, it was possible to estimate the frequency and damping of the first FA and SS modes. Furthermore, the damping estimates agreed with those found with help of a so called pull-out test.

- The damping estimates obtained using resampled simulation data in combination with the discrete-time PBSID$_{opt}$ algorithm were less accurate. This could either be the result of the resampling process or the fact that the wind turbine is barely excited in the SS direction at low wind speeds.

- The damping in the FA direction at low wind speeds could be accurately estimated using the continuous-time PBSID$_{o}$ algorithm applied to non-uniformly sampled simulation data. The same could not be said about the SS mode, which was underestimated at low wind speeds. This is also thought to be the effect of the low excitation of the OWT in the SS direction.

- The three different identification procedures were applied to data over a wide range of wind speeds. All of them provided similar results in terms of the estimated frequencies, which remained relatively constant at higher wind speeds. For the damping in the FA direction a small increase in damping was observed using resampled and non-uniformly sampled data. The PBSID$_{opt}$ algorithm applied to the original simulation data showed a larger increase in damping at higher wind speeds, but this is thought to be caused by the choice of past and future window size. All three identification procedures show very similar damping estimates for the SS direction, which show a large increase as function of wind speed. The increased damping can be explained by the fact that the turbine blades are pitched out. Hence, a large amount of air is displaced when the OWT moves in the SS direction, resulting in increased aerodynamic damping.

4. Identification of Turbine Measurement Data

- Using uniformly sampled measurement data at low wind speeds, the damping in the FA direction could be accurately identified. As expected the damping at low wind speeds was close to the structural damping. The estimated damping in the SS direction was higher than expected from the BHawC simulation results. The difference in estimated damping can have multiple causes. First, the load case that was used for the BHawC simulations is not representable for a real idling turbine. Second, the BHawC model might not be entirely accurate for simulation of an idling OWT at low wind speeds. Third, false assumptions regarding the structural, soil and hydrodynamic damping might have been used.

- Identification results using measurement data at high wind speeds showed a small increase in damping in the FA mode and a large increase in the SS mode. The results obtained with this data are similar to those obtained using BHawC simulation data.

- The fastlog data was used in two different ways in order to estimate the damping. Both the resampled and non-uniformly sampled measurement data provided similar results to those obtained with the PLM data.

With the help of these conclusions, it can thus be said that it is possible to use non-uniformly sampled measurement data for the identification of the structural parameters of the first FA and SS modes of an OWT. Furthermore, the accuracy of these results is similar to the accuracy obtained using uniformly sampled measurement data.

7-2   Recommendations

Based on the conclusions given in the previous section, recommendations for future work are presented in this section.

- For the current identification procedures only measurement data of pure idling wind turbines was considered. In order to increase the amount of available measurement data, other non-operational states should be considered as well. This can, for instance, refer to wind turbines under maintenance or idling when the blades are not pitched out.

- For this thesis, measurement data was taken from only one OWT. The identification can be extended to multiple turbines in the same wind farm in order to obtain site specific damping estimates.

- For the estimation of fatigue damage in an OWT, the damping of the first FA and SS modes are the most important factors. However, in order to validate the entire BHawC simulation model, higher modes need to be identified as well. Hence, it should examined if higher modes can be accurately identified and whether non-uniformly sampled measurement data is still suitable for this purpose.

- The selection of suitable measurement data is currently a time intensive process and not entirely waterproof. Further optimization and automation of the data selection process is therefore required if large amounts of measurement data are to be processed.

- The continuous-time $PBSID_o$ algorithm that was used in this thesis is very computationally intensive, resulting in longer computation times compared to the discrete-time $PBSID_{opt}$ algorithm. In order to make it competitive with its discrete-time counterpart, the implementation of the $PBSID_o$ algorithm should be further optimized.

- The non-uniformly sampled measurement data that was used in this thesis only contained two acceleration channels that were useful for identification. Increasing the amount of acceleration channels generally improves the accuracy of the identification results. Therefore, it might be worthwhile to install additional accelerometers along the tower of the OWT.

- From the results obtained with fastlog measurement data, it can be concluded that the structural parameters of the first FA and SS modes can still be estimated using resampled data. This also allows the use of other OMA methods. In order to find out if the $PBSID_{opt}$ algorithm is the optimal identification method, several of the algorithms discussed in Chapter 2 should be applied to resampled measurement data as well.

Extracting Structural Parameters from a State-Space Model

In this appendix it is shown how the structural parameters of a system can be extracted from the state-space matrices. Only the system matrix A and the output matrix C are used in determining the structural parameters of the estimated system. By performing an eigenvalue decomposition of the A matrix, the eigenvalues and eigenvectors of the system are obtained. The eigenvalues, $\lambda_i = \sigma_i \pm j\omega_i$, are composed of a real and imaginary part and can be used to determine the natural frequencies ω_{n_i} and damping ratios ζ_i in the following way:

$$\omega_{n_i} = \sqrt{\sigma_i^2 + \omega_i^2}, \tag{A-1}$$

$$\zeta_i = -\frac{\sigma_i}{\omega_{n_i}}. \tag{A-2}$$

The damping of a system can also be expressed as the logarithmic decrement δ_i, which has the following relation to the damping ratio:

$$\delta_i = \frac{2\pi\zeta_i}{\sqrt{1 - \zeta_i^2}}. \tag{A-3}$$

In order to separate natural frequencies that are located close to each other it is necessary to know their mode shapes. The mode shape of each natural frequency can be determined using an eigenvector ψ_i and the output matrix C, such that a modeshape ϕ_i is obtained by

$$\phi_i = C\psi_i. \tag{A-4}$$

Appendix B

Identification Results from BHawC Simulations

This appendix presents the identification results of the three remaining load cases illustrated in Figure 5-2. For all loadcases the frequencies could be accurately estimated and were seen to be consistent over the entire range of wind speeds. Therefore, the estimated frequencies are not visualized in this appendix.

The estimated damping for all three load cases is presented in terms of the average value in Figures B-1 to B-3. For the discrete-time PBSID_{opt} algorithm, past and future windows of $p, f = 200$ were used. For the continuous-time PBSID_o algorithm $p, f = 35$ and $a = 5$ were selected as identification parameters.

In all three load cases it is observed that the estimated damping in the SS direction shows a similar upward trend for increasing wind speeds. Furthermore, these damping estimates are similar to those from the first load case as well. For the load cases where the wind is coming in the SS direction, it can be observed that the damping in the FA direction remains constant over the range of wind speeds. In the fourth load case the wind is coming in the FA direction, resulting in an increased damping of the FA mode.

Figure B-1: Estimated damping values obtained through three different identification procedures over a range of wind speeds for load case 2.

Figure B-2: Estimated damping values obtained through three different identification procedures over a range of wind speeds for load case 3.

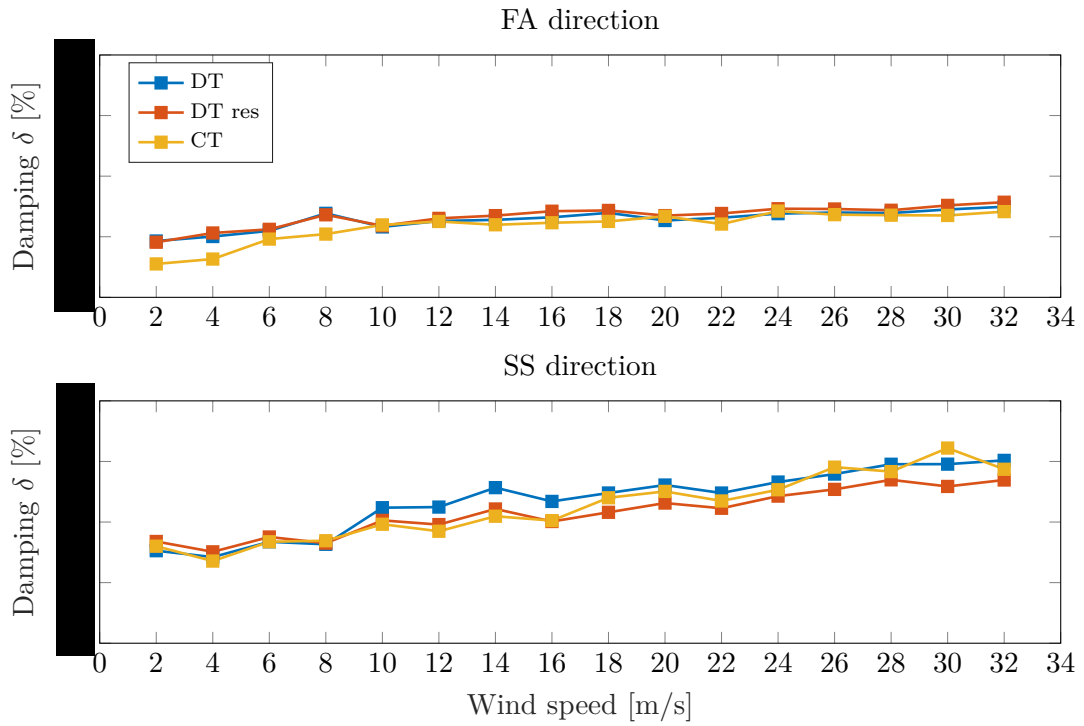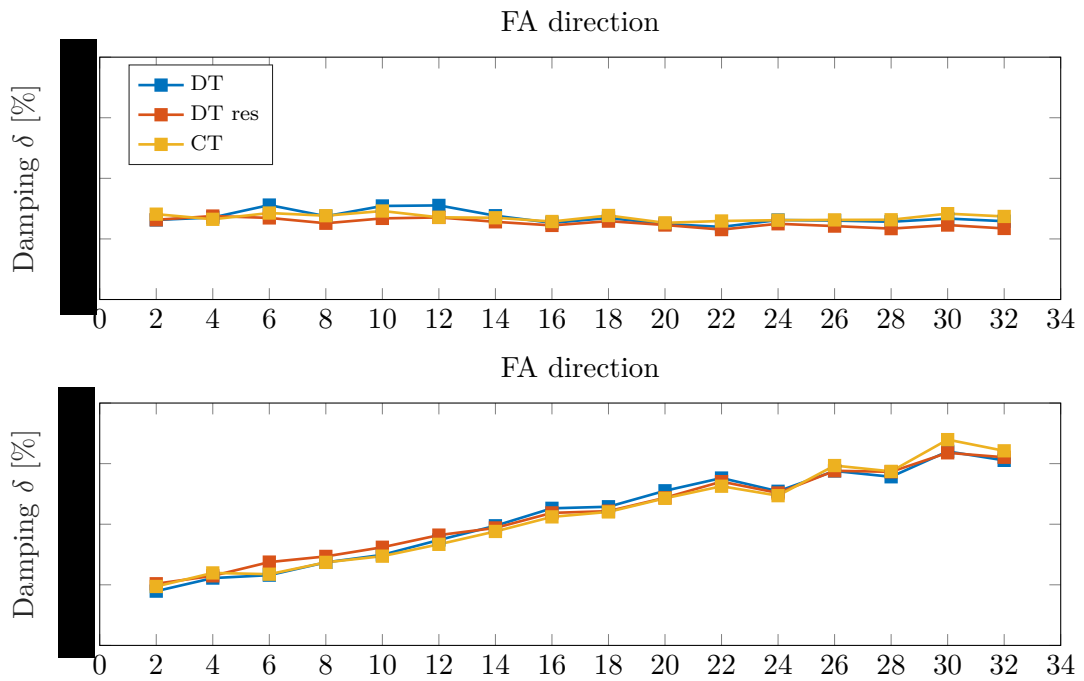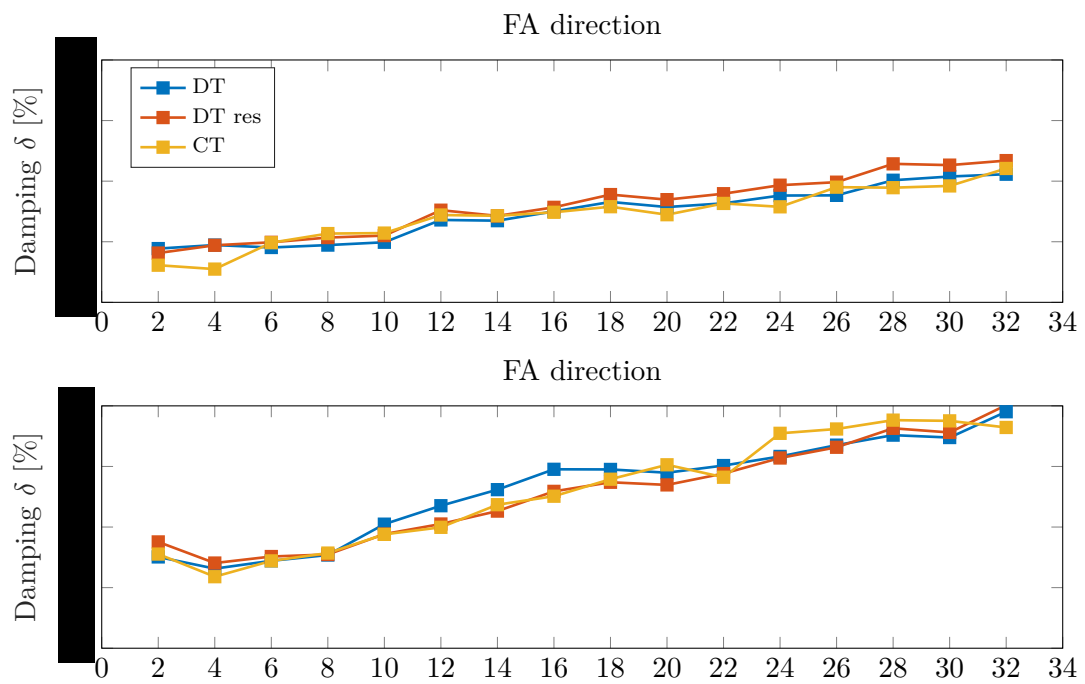**Figure B-3:** Estimated damping values obtained through three different identification procedures over a range of wind speeds for load case 4.

Bibliography

[1] CBS, "Hernieuwbare energie in nederland 2015," tech. rep., CBS, September 2016.

[2] J. van der Tempel, *Design of Support Structures for Offshore Wind Turbines*. PhD thesis, Delft University of Technology, 2006.

[3] P. L. C. van der Valk and D. J. Rixen, *An Effective Method for Assembling Impulse Response Functions to Linear and Non-linear Finite Element Models*, pp. 123–135. New York, NY: Springer New York, 2012.

[4] M. Bergamasco, *Continuous-time model identification with applications to rotorcraft dynamics*. PhD thesis, Politecno di Milano, 2012.

[5] UNFCCC, *Adoption of the Paris Agreement*, December 2015.

[6] SER, "Energieakkoord voor duurzame groei," September 2013.

[7] SIEMENS, "Transitiecoalitie." https://electricitymatters.siemens.nl/2017/02/17/transitiecoalitie-wil-tempoversnelling-bij-energietransitie/, 2016.

[8] Rijksoverheid, "Nederlands consortium bouwt tweede windpark borssele nog goedkoper." https://www.rijksoverheid.nl/actueel/nieuws/2016/12/12/nederlandse-consortium-bouwt-tweede-windpark-borssele-nog-goedkoper, 2016.

[9] M. Seidel, "Wave induced fatigue loads," *Stahlbau*, vol. 83, no. 8, pp. 535–541, 2014.

[10] C. Devriendt, P. J. Jordaens, G. D. Sitter, and P. Guillaume, "Damping estimation of an offshore wind turbine on a monopile foundation," *IET Renewable Power Generation*, vol. 7, pp. 401–412, July 2013.

[11] M. H. Hansen, K. Thomsen, P. Fuglsang, and T. Knudsen, "Two methods for estimating aeroelastic damping of operational wind turbine modes from experiments," *Wind Energy*, vol. 9, no. 1-2, pp. 179–191, 2006.

[12] R. Shirzadeh, C. Devriendt, M. A. Bidakhvidi, and P. Guillaume, "Experimental and computational damping estimation of an offshore wind turbine on a monopile foundation," *Journal of Wind Engineering and Industrial Aerodynamics*, vol. 120, pp. 96 – 106, 2013.

[13] P. L. C. van der Valk and M. G. L. Ogno, *Identifying Structural Parameters of an Idling Offshore Wind Turbine Using Operational Modal Analysis*, pp. 271–281. Springer International Publishing, 2014.

[14] H. C. Kramers, P. L. van der Valk, and J.-W. van Wingerden, "Statistical evaluation of the identified structural parameters of an idling offshore wind turbine," *Journal of Physics: Conference Series*, vol. 753, no. 5, p. 052006, 2016.

[15] W. Versteijlen, A. Metrikine, J. Hoving, E. Smid, and W. de Vries, "Estimation of the vibration decrement of an offshore wind turbine support structure caused by its interaction with soil," *Knowledge, Technology and Policy*, January 2011.

[16] D. J. Rixen, *Lecture notes: Engineering dynamics*. Delft University of Technology, Sept 2008. Chapter 4.

[17] P. Avitabile, "Experimental modal analysis," *Sound and Vibration*, Jan 2001.

[18] D. Tcherniak, S. Chauhan, and M. H. Hansen, *Applicability Limits of Operational Modal Analysis to Operational Wind Turbines*, pp. 317–327. Springer New York, 2011.

[19] G. H. James, T. G. Laufer, and J. P. Nard, "Modal testing using natural excitation," in *Proc. of the 10-th IMAC*, Feb 1992.

[20] L. Ljung, "Prediction error estimation methods," *Circuits, Systems and Signal Processing*, vol. 21, no. 1, pp. 11–21, 2002.

[21] L. Zhang, R. Brincker, and P. Andersen, "An overview of operational modal analysis: major developments and issues," *Mechanical systems and signal processing*, 2009.

[22] M. Verhaegen and V. Verdult, *Filtering and System Identification*. Cambridge University Press, 2007.

[23] A. Chiuso, "The role of vector autoregressive modeling in predictor-based subspace identification," *Automatica*, vol. 43, no. 6, pp. 1034–1048, 2007.

[24] N. J. Jacobsen, P. Andersen, and R. Brincker, "Using enhanced frequency domain decomposition as a robust technique to harmonic excitation in operational modal analysis," in *Proc. of ISMA 2006: International Conference on Noise and Vibration Engineering*, 2006.

[25] P. Verboven, *Frequency domain system identification for modal analysis*. PhD thesis, Vrije Universiteit Brussel, May 2002.

[26] M. El-Kafafy, C. Devriendt, W. Weijtjens, G. De Sitter, and P. Guillaume, *Evaluating Different Automated Operational Modal Analysis Techniques for the Continuous Monitoring of Offshore Wind Turbines*, pp. 313–329. Cham: Springer International Publishing, 2014.

[27] A. Chiuso, "On the relation between CCA and predictor-based subspace identification," *IEEE Transactions on Automatic Control*, vol. 52, pp. 1795–1812, Oct 2007.

[28] P. van Overschee and B. de Moor, *Subspace Identification for Linear Systems.* Kluwer Academic Publishers, 1996.

[29] G. van der Veen, J. van Wingerden, M. Bergamasco, M. Lovera, and M. Verhaegen, "Closed-loop subspace identification methods: an overview," *IET Control Theory Applications*, vol. 7, pp. 1339–1358, July 2013.

[30] I. Houtzager, J. van Wingerden, and M. Verhaegen, "Varmax-based closed-loop subspace model identification," in *Proceedings of The 48th IEEE Conference on Decision and Control, Shanghai, China*, 2009.

[31] H. Akaike, "A new look at the statistical model identification," *IEEE Transactions on Automatic Control*, vol. 19, pp. 716–723, Dec 1974.

[32] K. Burnham and D. Anderson, *Model Selection and Inference: A Practical Information-Theoretical Approach.* Springer-Verlag New York, 1998.

[33] A. Chiuso, "On the asymptotic properties of closed-loop cca-type subspace algorithms: Equivalence results and role of the future horizon," *IEEE Transactions on Automatic Control*, vol. 55, no. 3, pp. 634–649, 2010.

[34] F. Magalhães, Álvaro Cunha, and E. Caetano, "Online automatic identification of the modal parameters of a long span arch bridge," *Mechanical Systems and Signal Processing*, vol. 23, no. 2, pp. 316 – 329, 2009.

[35] R. J. Allemang, "The modal assurance criterion - twenty years of use and abuse," *Sound and Vibration*, 2003.

[36] B. R. J. Haverkamp, C. T. Chou, M. H. Verhaegen, and R. Johansson, "Identification of continuous-time MIMO state space models from sampled data, in the presence of process and measurement noise," in *Decision and Control, 1996., Proceedings of the 35th IEEE Conference on*, vol. 2, pp. 1539–1544 vol.2, Dec 1996.

[37] B. R. J. Haverkamp, C. T. Chou, and M. Verhaegen, "Subspace identification of continuous-time Wiener models," in *Decision and Control, 1998. Proceedings of the 37th IEEE Conference on*, vol. 2, pp. 1846–1847 vol.2, Dec 1998.

[38] R. Johansson, M. Verhaegen, and C. T. Chou, "Stochastic theory of continuous-time state-space identification," *IEEE Transactions on Signal Processing*, vol. 47, pp. 41–51, Jan 1999.

[39] B. R. J. Haverkamp, *State space identification: theory and practice.* PhD thesis, Delft University of Technology, 2001.

[40] H. Stark and J. Woods, *Probability and Random Processes with Applications to Signal Processing.* Prentice Hall, 2002.

[41] Y. Yamamoto, "A function space approach to sampled-data control systems and tracking problems," *IEEE Transactions on Automatic Control*, vol. 39, no. 4, pp. 703–712, 1994.

[42] Y. Ohta and T. Kawai, "Continuous-time subspace system identification using generalized orthonormal basis functions," in *16th Int. symp. on mathematical theory of networks and systems*, (Leuven, Belgium), 2004.

[43] Y. Ohta, "Realization of input-output maps using generalized orthonormal basis functions," *Systems & Control Letters*, vol. 54, pp. 521–528, 2005.

[44] Y. Kinoshita and Y. Ohta, "Continuous-time system identification using compactly-supported filter kernels generated from laguerre basis functions," in *49th IEEE Conference on Decision and Control (CDC)*, pp. 4461–4466, Dec 2010.

[45] M. Bergamasco and M. Lovera, "Continuous-time predictor-based subspace identification using laguerre filters," *IET Control Theory Applications*, vol. 5, pp. 856–867, May 2011.

[46] R. Shirzadeh, W. Weijtjens, P. Guillaume, and C. Devriendt, "The dynamics of an offshore wind turbine in parked conditions: a comparison between simulations and measurements," *Wind Energy*, vol. 18, no. 10, pp. 1685–1702, 2015.

Glossary

List of Acronyms

AIC   Akaike Information Criterion

ARX   Auto-Regressive with eXogenuous input

BHawC   BONUS Horizontal axis wind turbine Code

DCSC   Delft Center for Systems and Control

DoF   Degree of Freedom

EFDD   Enhanced Frequency Domain Decomposition

EMA   Experimental Modal Analysis

FEM   Finite Element Method

FFT   Fast Fourier Transform

FA   Fore-Aft

FDD   Frequency Domain Decomposition

LTI   Linear Time-Invariant

OMA   Operational Modal Analysis

OWT   Offshore Wind Turbine

MAC   Modal Assurance Criterion

MIMO   Multiple-Input Multiple-Output

MDoF   Multi-Degree-of-Freedom

MOESP   Multivariable Output-Error State-sPace

NExT   Natural Excitation Technique

PEM	Prediction Error Methods
PLM	Power Load Measurement
PSD	Power Spectral Density
PBSID	Predictor-Based Subspace IDentification
RNA	Rotor Nacelle Assembly
SS	Side-Side
SMI	Subspace Model Identification
SSI	Stochastic Subspace Identification
SVD	Singular Value Decomposition
SWP	Siemens Wind Power
VAF	Variance-Accounted-For
VARX	Vector-Auto-Regressive with eXogenuous input
ZOH	Zero-Order Hold